Thesis for the degree of doctor of philosophy

in

Thermo and Fluid Dynamics

Numerical Modelling of Diesel Spray Injection, Turbulence Interaction and Combustion

Fabian Peng Kärrholm

Department of Applied Mechanics

Chalmers University of Technology

Göteborg, Sweden, 2008

Numerical Modelling of Diesel Spray Injection, Turbulence Interaction and Combustion
Fabian Peng Kärrholm

The image on the cover of the thesis is an illustrative image of a lagrangian spray, evaporation has been turned off to improve the visual experience.

I guess this is my dissertation
Homie this ... is basic, Welcome to Graduation
Good morning,
Good morning
On this day, we become legendary
- Kanye West

Abstract

This thesis covers two main topics. The first is numerical modelling of cavitating diesel injector flows, focusing on describing such flows using a single-phase cavitation model based on a barotropic equation of state together with a homogenous equilibrium assumption. The second topic is Euler-Lagrangian simulations of diesel sprays, focusing on attempts to reduce the high grid/timestep dependencies in numerical simulations of diesel sprays. In addition, the ability of two CFD codes to predict flame lift-off length and ignition delay time, and the advection scheme's influence on fuel distributions, are considered.

A long-term goal was to develop a new atomization model based on calculated flows in injector nozzles, which did not have the drawback of requiring either non-physical parameters or information derived from specific experiments. To validate the cavitation simulations, comparisons were made with experimental data obtained at AVL. The experimental data (which are practically 2D) provide information on velocity profiles and pressure contours. These data were used to validate the code. However, since the code is not stable for diesel-type pressures, no atomization model was developed.

The main part of the thesis describes how diesel sprays were simulated using the discrete droplet model (DDM), in which the liquid is described by Lagrangian coordinates and the vapour by an Eulerian approach. The simulations have been used to investigate how the k-ε family of turbulence models influence spray behaviour, and a simple but efficient way to reduce the dependency of the mesh resolution, by limiting the turbulence length scale in the liquid core region, is proposed. This constraint is shown to have a positive effect on the spray behaviour, and to reduce both grid and timestep dependencies.

In addition, the ignition delay time and flame lift-off lengths have been investigated, since these two properties are believed to be important for emissions formation. The simulations used a complex chemical mechanism involving 83 species and 338 reactions. The effects of the numerical scheme, the turbulence model and physical parameters (like ambient temperature and oxygen content) on these variables have also been investigated.

Keywords: Spray, Computational Fluid Dynamics, Diesel, Turbulence Model, Cavitation, Atomization, Flame, Lift-off, Ignition Delay, Numerical Scheme, TVD, Combustion

iv

Acknowledgements

Nomenclature

Roman Symbols

b	Relaxation coefficient	
c	Molar Concentration	mol/m^3
c_l	Liquid specific heat at constant volume	J/kgK
$c_\mathrm{p,v}$	Fluid specific heat at constant volume	J/kgK
C_1,C_2,C_3,C_μ	Turbulence model constants	
C_D	Drag coefficient	
C_d	Discharge coefficient of nozzle	
C_e	Constant of the D^2-law	
Co	Courant number	
d	Droplet diameter	m
D	Droplet Diameter	m
$\mathcal{D}$	Mass Diffusion Coefficient	m^2/s
E_a	Arrhenius Activation Energy	J/mol
$\mathbf{F}$	Force on particle	kgm/s^2
$\mathbf{F}^s$	Spray momentum source term	kgm/s^2
f	Coefficient in RNG turbulence model	
f_heat	Correction factor for heat exchange due to mass transfer	
$\mathbf{g}$	Gravitation acceleration vector	m/s^2
h_v	Enthalpy of vapour	J/kg
k	Kinetic energy of turbulent fluctuations	m^2/s^2
k_j	Arrhenius constant of reaction j	
l_∞	Relaxation length scale	m
l_t	Length scale of turbulent fluctuations	m
L_sgs	Maximum user-set length scale	m
m	Mass	kg
n	Parameter for Rosin-Rammler distribution	
$\hat{n}$	Face Normal	
N_r	Number of reactions	
N_s	Number of species	
Nu	Nusselt number	
Oh	Ohnesorge number	
p_0	Pressure at outlet in previous time step	Pa
p_∞	Desired outlet pressure	Pa
p	Pressure	Pa

$\mathbf{p}$	Momentum	kgm/s
R_{RNG}	Coefficient in the RNG k-ε turbulence model	
R	Universal Gas Constant	J/Kmol
$\mathbf{RR}_i$	Reaction Rate of species i	
Re	Reynolds number of fluid	
S	Strain	1/s
S_{fa}	Help variable	
Sc	Schmidt number	
Sh	Sherwood number	
T	Temperature of fluid	K
t	Time	s
Ta	Taylor number	
$\mathbf{u},\mathbf{U}$	Velocity	m/s
w	Outgoing pressure wave velocity	m/s
We	Weber number	
X_i	Volume fraction of scalar i	
$X_{v,s}$	Mass fraction of fuel vapour at droplet surface	
$X_{v,\infty}$	Mass fraction of fuel vapour far away	
Y_i	Mass fraction of scalar i	

Greek Symbols

α	Volume fraction of fluid	
$\alpha_k,\alpha_\varepsilon$	Turbulence model constant	
β	Volume fraction of fluid	
β_{max}	Maximum spray cone angle	
γ	Vapour (cavitated liquid) fraction	
δ	Cell-face distance coefficient	m
Δt	Time-step	s
ε	Dissipation rate	m^2/s^3
κ_c	Thermal Conductivity	W/mK
λ	Limiter function for `interfaceCompression`-scheme	
Λ	Wavelength of fastest growing wave	m
μ	Laminar viscosity	kg/ms
μ_T	Turbulent viscosity	kg/ms
ν	Kinematic viscosity	m^2/s
ρ	Density	kg/m^3
$\dot{\rho}^s$	Spray mass source term	kg/m^{3}s
τ_e	Relaxation time of evaporation	s
τ_u	Momentum relaxation time	s
ϕ	Volume flow across cell face	m^3/s
ψ	Compressibility	s^2/m^2
Ω	Growth rate of fastest growing wave	m/s^2

Contents

Chapter 1

Introduction

1.1 Background & Motivation

Today, cars and heavy duty vehicles are considered to be major sources of environmental pollution. However, when the first automobiles appeared in the streets of New York and London they were considered to be solutions to another problem: horse manure. According to a rough estimate published in Appleton's magazine in 1908, 20 000 New Yorkers died each year from "maladies that fly in the dust, created mainly by horse manure". Details of the data used to obtain the estimate are unknown, but there is no doubt that horses, and the resulting manure, constituted a major environmental problem[1]. In the late 19th century, Nikolaus Otto in 1876, and later Rudolf Diesel in 1897 patented their prime mover inventions. Horse manure became a problem of the past. However, now, over 100 years later, we are facing a new environmental threat, and this time our former saviours have become our problem.

The Diesel engine is facing many challenges today, one of which is to reduce soot and NO_x generated in the process of burning the fuel. Both soot and NO_x are harmful to humans and animals ([2],[3]), so national governments around the world are forcing manufacturers to decrease specific emissions from the vehicles they produce, as shown in figure 1.1. According to an estimate quoted in a report on the Diesel engine by P. Kageson [3], each year roughly 21 000 people over the age of thirty in France, Switzerland and Austria died prematurely due to heart and lung-diseases caused by particulate matter from vehicle traffic. It should be noted that more people are dying from traffic pollution, than from traffic accidents in these countries.

In addition to the demands imposed by environmental legislation, manufacturers have to meet the customers' demands, who are often more concerned about cupholders, extra horsepower and larger cars, than about improving fuel eceonomy. In surveys by CNW Marketing Research [5], buyers of cars were asked which factors were important in their decisions. These
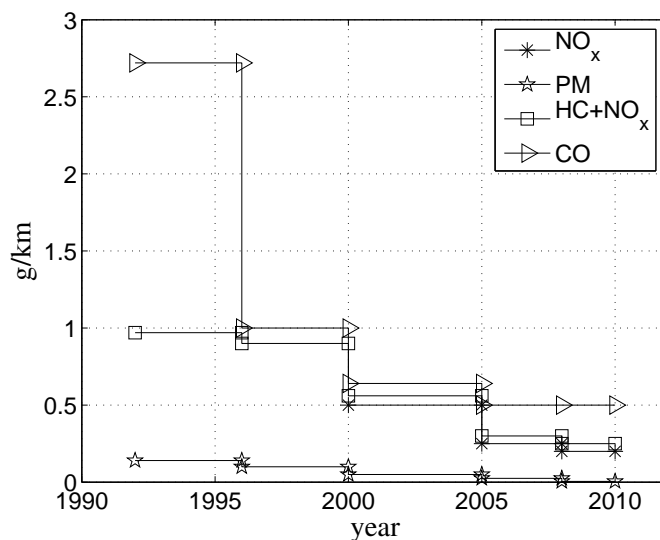
Figure 1.1: Changes in legal limits for emissions from automobiles within the EU, 1992-2008 [4].

surveys showed that although fuel economy increased from being important to just 27.2% of the buyers in 1995, to 61.3% in 2005, it was important to fewer customers than factors like interior comforts, manufacturer's reputation, sound system, and overall exterior styling (the reason most buyers found important). It should be noted that the survey does not take into account how important the factors were to the buyers, only the numbers who thought they were important reasons for their choices. There also seems to be a discrepancy between what consumers claim to do, and what they actually do. The same report provides data on the average weights of US light vehicles and average fuel consumption dating back to 1975. If most consumers really considered fuel economy to be an important factor when choosing a car, a decline or at least reductions in the rate of increase in vehicle size would be expected. However, as can be seen from figure 1.2, the power of the engine per unit vehicle weight has increased over the past 30 years, and increased even more since 2005. The figure also shows that fuel consumption per unit distance travelled declined sharply between 1975 and 1985, but due to the increases in power & weight, the decrease has flattened out since then. If customer awareness is increased, or the oil price is drastically increased, perhaps the demand for large cars with powerful engines will decline. Downsizing of the engine could then become a viable option to meet legislative demands as well as customer needs. It should also be mentioned that increases in safety features of modern cars have also increased their weight.

In figure 1.3, the amounts of NO_x and CO_2 emitted into the atmosphere between 1990-2005 from vehicles in Sweden are shown. The amounts of harmful NO_x gases are decreasing, while those of the greenhouse gas CO_2 are slowly increasing. CO_2 is an inevitable product of combustion when
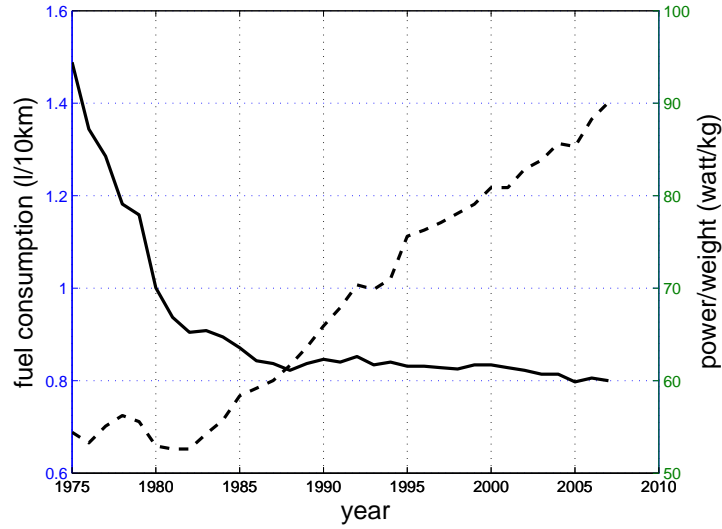
Figure 1.2: Fuel consumption per unit distance travelled (solid line), and power per unit weight of cars (dashed line), 1975-2007
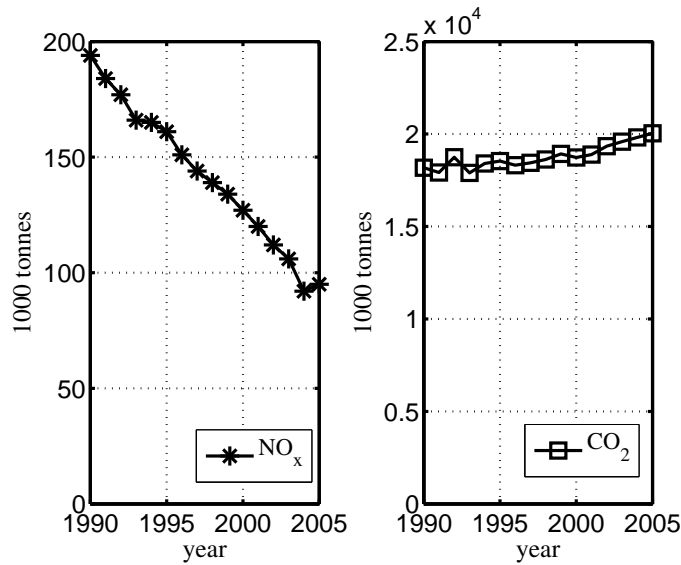
Figure 1.3: Emissions from vehicles in Sweden, in 1000 tonnes, 1990-2005 [6]

carbon-based fuels are burnt, and the only way to reduce emissions of it is to burn less. This can be done either by increasing the efficiency of the engine, or using the engine less. The second option becomes more interesting as battery power is increased. However, batteries that can power a vehicle for long-haul highway operations are still far in the future. For the nearer future, increasing fuel efficiency and engine downsizing are more likely to be viable strategies.

There are two branches of research concerning the optimization of engine design and operators: one involving experiments with physical engines, and the other involving attempts to model engines numerically. A symbolic relationship between the two approaches is usually employed, since neither of them can capture all the relevant details. The experimenter does not know exactly what happens inside the engine, and the modeller cannot be certain the events predicted by the model are correct without experimental verification. However, with a verified model, a reasonable description of the processes taking place can be obtained. In addition, the modeller has all the data available from them. Another advantage of modelling is that it allows conceptual engines and combustion modes to be explored long before prototypes are made. Simulations can also be useful for parameter studies, where they provide a cheaper alternative than large-scale engine studies.

1.2 Simple Description of the Computational Approach

CFD is an abbreviation of Computational Fluid Dynamics, and refers to solving a finite approximation of the Navier-Stokes equations numerically. The spatial domain of interest, for example the cylinder of an engine, the shape of a car, or the inside of a diesel injector, is divided into several small cells or control volumes. The sum of the control volumes, called a mesh, provides a finite approximation of the spatial domain. Solving conservation equations using such a mesh is called an Eulerian approach, meaning that each position in space has a numerical representation. For instance, a thermometer that measures the outdoor temperature at the same spot every day provides an example of an Eulerian description of temperature. Another way to describe reality is to follow a particle, and compute its state vector, including variables such as its position over time, conserving momentum and energy. This approach, known as Lagrangian, is particularly appropriate when all forces acting on an object are known. For example, the path of a rocket can be conveniently described in Lagrangian coordinates, as all forces acting on the rocket moves with it.

A combination of these two representations is often used in Diesel spray simulations. The air in the combustion chamber is described using an Eulerian framework, and the liquid spray is discretised into computational 'parcels', each of which is described by Lagrangian coordinates. That is, we inject part of the spray, and track its position in time. The parcels may consist of any number of droplets, each of which is considered identical, depending on values set by the user. Each of these parcels is subject to the same processes as a real diesel spray, including (*inter alia*): atomization, break-up, collision, evaporation, heat transfer and turbulence. The processes mentioned, such as heat transfer, occur as integral operations over the particle's entire surface, but resolution of particle surfaces is computationally prohibitive. Therefore, a 'point particle' approximation is typically made, which requires a large number of sub-models to empirically account for integral fluxes over the

particle surfaces. Further sub-models, requiring still more empiricism, are needed to model physical processes such as atomization. Unfortunately, most of the sub-models available today are quite unreliable, and depend on the user to supply constants that have limited physical interpretability. These constants can often differ widely between authors, and publications, depending on the type of spray behaviour being considered. A typical example is the breakup constant in the KelvinHelmholz-RayleighTaylor model ([7],[8],[9]), which can vary over an order of magnitude.

1.3 Implementation and Code

The code used in the work this thesis is based upon was OpenFOAM ([10] &[11]); an open-source code available at `www.openfoam.com`. It is an object-oriented code written in C++, which makes it reasonably straightforward to implement new models and fit them into the whole code structure. OpenFOAM is being continously developed; when I started my doctoral studies I used Nabla FOAM 1.2, followed by OpenFOAM 1.0 up until the recent 1.4.1 (the latest, 1.5, release has not been used). The code now includes polyhedral mesh support, making it possible to create meshes using any form of cells, as long as the quality of the resulting mesh is high. Lagrangian parcels are tracked by face-to-face tracking, thus no parcels are lost when moving between cells as in Kiva-3V. Further, models are implemented to be run-time-selectable, which makes it very easy for the user to switch between turbulence models, spray sub-models, numerical schemes etc. OpenFOAM has many other advantages[1], but one of the most important is the complete parallelization of the code. All solvers written in OpenFOAM can easily be run in parallel, since the code is parallelized at such a fundamental level, removing the need (in most cases) for the user to consider multiple processor simulations.

OpenFOAM code was chosen both because of the high scope it offers for developing new models, and the demands it places on the user. It is more difficult to not know what you are doing in OpenFOAM, than in other codes. One could argue that access to source code, and knowledge of what one is doing, can easily be achieved by using an in-house code. While this is true, I believe that research should generally be done in a community in which exchange of information is the norm, and an important contributor to progress. The ability to share codes and ideas developed in the same framework is one of OpenFOAM's most important strengths.

---

[1]One of the most recent additions is an automatic mesh generator.

1.4   Outline of the Thesis

The Introduction chapter presents basic information about sprays, and motivation for the work. The idea is that this chapter should be understandable to people without a degree in engineering. Subsequent chapters assume a knowledge of basic university level math and physics. In the following chapters, the project is described in the same order that the fuel travels, starting with the nozzle flow, and then on to the spray calculations, turbulence interactions and combustion. Some parts of the modelling have been described twice (in both papers and the thesis), but such repetition has been kept to a minimum. Where it is included, it is included for continuity, or because the description in the article was too concise due to size limitations.

The goals of the work have been to improve existing models for diesel spray simulations, and to develop better models. Spray modelling today is at a stage where there is a heavy reliance on experimental data for validation. One example is the dependency on the computation grid. The errors in spray simulations do not follow the common CFD rule of decreasing as the number of cells is increased[12]. Instead, the discretization error has a minimum for a specific grid size, due to the relationship between the liquid (Lagrangian parcels) and the gas (Eulerian cells). The minimum has to be found on a case-to-case basis, and the results compared to experimental data to determine which grid is most suitable. Therefore, spray simulations are more sensitive to the grid than other CFD simulations, since an increase in the number of cells can either increase or decrease the quality of the simulation. If some of this grid dependency could be reduced, it would be of great value to the numerical community.

Euler-Lagrangian spray simulations uses sub-models to describe the processes that affect the injected liquid. One of the models that has been focused on in this work is the injection and atomization model. The model is used to obtain initial droplet size and velocity parameters, thus it has a major influence on the initial breakup of the spray. Atomization refers to the primary breakup of the liquid core of the spray, and it is separated from secondary breakup, which describes how liquid droplets are split into smaller droplets. An atomization model can be used to describe how the droplets break up initially, or simply switch off breakup within a certain distance from the injector. The most common way to inject droplets in Euler-Lagrangian sprays is to use a size distribution and randomly inject droplets from the injector in directions within the prescribed cone angle. A better injection model taking cavitation, turbulence and the flow in the nozzle into account that is only dependent on physical parameters could increase the quality of the simulations. Therefore, a goal of this project was to develop such a model, which does not prescribe an injection angle and droplet distribution, but calculates it from set variables such as the injection pressure, fuel density, length and width of the nozzle etc.

A very important parameter for diesel simulations is the flame lift-off length, which is believed to have a strong effects on the emissions generated during combustion, since increasing it will cause the flame to have a more premixed character and consequently yield lower emissions of NO_x and particulate

matter. The lift-off length phenomenon is quite complex, and requires a well-developed spray model to even appear. If inappropriate schemes, sub-models and combustion models are employed the flame will spread all the way to the nozzle and no lift-off length will be observed. It is also closely linked to the ignition delay time, which is very important for engine simulations since full control over the ignition is highly desirable. Attempts were also made to bench-mark OpenFOAM's performance in terms of simulating these phenomena, and compare it to that of the commonly used KIVA-3V code.

The last issue addressed during the work underlying this thesis were the effects of numerical schemes and initial turbulent viscosity on the solution. It was discovered quite early on (during the studies described in Paper 1) that the chosen scheme and initial parameters have a large influence over the resulting spray. Part of the reason why this was studied is the wide variety of schemes available in OpenFOAM, in which it is very easy to switch between different types.

Chapter 2

Nozzle Flow

In both Diesel engines and direct injection spark ignition engines fuel is injected into the combustion chamber by high pressure. Ideally, it should then atomize, form small droplets, and eventually completely evaporate, yielding a mixture that is easily combustible without forming either soot or NO_x. In a spark ignition engines it is also important to position the fuel cloud close to the spark plug to promote good combustion. The atomization, i.e. the formation of the initial droplets and their breakup, is mainly governed by the flow in the nozzle which ejects the spray ([13]). It is therefore important to study the flow inside the nozzle, to find out how it is linked to the spray in the cylinder. Furthermore, cavitation is believed to have a strong influence on the flow inside the nozzle, so it is also important to consider these effects.

Cavitation can occur when fluid of high velocity passes through a contraction like a nozzle. A pocket of low pressure is formed in the wake of the contraction's edge, and if the pressure in this wake is sufficiently low, i.e. below the saturation pressure, the liquid will cavitate. The size of the cavitation bubbles will depend on several factors, including injection pressure, geometry, smoothness of the interior of the nozzle, and the properties of the fluid. For example, if the fluid is pushed through the nozzle sufficiently slow, no cavitation will occur and ordinary pipe flow will be observed.

Cavitation introduces vapour bubbles into the flow and increases the maximum velocity in the centre. The velocity is increased for two reasons when the fluid is cavitating. Firstly, if there is vapour along the walls the liquid will not have a no-slip condition boundary since the vapour will not be stationary, thus allowing the velocity of the liquid to increase (which is essential when there is a high pressure drop over the nozzle). Secondly, when the fluid is cavitating the liquid can not fill the entire channel. Furthermore, since the vapor bubbles formed in the nozzle are mixed with the liquid, when they reach the combustion chamber the ligaments and droplets formed are already partly evaporated through cavitation. The remaining liquid will evaporate faster, and the entire atomization process will be accelerated.

2.1   Previous Works in the Field

The flow inside a diesel nozzle has been studied by many researchers, both experimentally ([14],[15],[16],[17]), and numerically ([17],[18],[19],[20]). The results from [15] by Winklhofer *et al* have been used in this work to validate the single-phase cavitation model. They have been used previously in [21] using a Rayleigh Bubble Growth model [22]. In some studies nozzle flow calculations have been coupled to Lagrangian spray simulations ([23]) on a case-to-case basis, but few authors have performed nozzle simulations with intention to create a new atomization model for Euler-Lagrangian diesel spray simulations covering a comprehensive range of initial conditions. An exception is Ning [24], who developed a new atomization model for the Euler-Lagrangian Spray and Atomization (ELSA) approach. ELSA is a mixture of modelling approaches in which a full Eulerian description is used for the near-nozzle flow where the spray is dense, but if the liquid volume fraction falls below a user-set value, it is transformed into a Lagrangian parcel.

An additional complication when modelling cavitation that most studies have neglected (one exception is [25]) is the effect of cavitation in multi-hole injectors. As reported by Nouri *et al* in [26], strings of cavitation can occur between different nozzle holes in multi-hole injectors and the strings reduce the effective hole flow area, which in turn increases the flow velocity.

Cavitation is usually modelled using either Rayleigh bubble growth dynamics theory in conjunction with a volume of fluid method ([17],[22],[27]) or, the Homogenous Equilibrium Model (HEM,[20],[28]), which assumes that the cavitated mixture is perfectly mixed and the amount of cavitation can be described by a vapour mass fraction between 0 and 1. In both approaches an assumption about isentropic nozzle flow is usually included, and the HEM approach needs an equation of state relating pressure and density to calculate the growth of cavitation. The Rayleigh bubble growth approach solves a transport equation for the liquid-gas interface, with a source term to model cavitation, calculated from a simplified Rayleigh equation. There is also a third approach, based on Gibbs free energy [29], which is very rarely used.

Previous works in the field have modelled cavitating liquid, but not the ambient air in the combustion chamber. This is often an essential simplification due to the difficulty of resolving three phases while maintaining reasonable computational times. As part of this project, OpenCFD Ltd. was contracted to develop a code handling liquid, cavitating liquid and ambient air. The resulting code has not been validated within this project, due to problems in its handling of diesel fuel flows. However, it is possible to use it to simulate water injections, although the simulation time extends over several weeks. This code was originally described in [30], but since the cited publication has limited availability it will also be described here. A simpler code (presented in the following section) for a cavitating fluid was also developed as part of the project.

2.2 A Code for Cavitating Diesel Injector Flow into Air

The purpose of this code is to simulate cavitating diesel fuel injected into a chamber filled with air. Even though the code can have other uses, simulating diesel injections was its original purpose. In this text, gas refers to the ambient gas which the liquid is injected into, and vapour to liquid that undergoes cavitation. To simulate the liquid-gas interface, the Volume of Fluid (VOF) method is used, in which the liquid phase is allowed to cavitate and the gas phase can be compressed due to pressure shocks. The equations that need to be solved are, as usual, the momentum equation and the continuity equation, presented below:

$$\frac{\partial \rho \mathbf{U}}{\partial t} + ((\mathbf{U} \cdot \nabla)\rho \mathbf{U}) - \nabla \cdot (\mu \nabla \mathbf{U}) = -\nabla p \tag{2.1}$$

with

$$\mu = \alpha(\gamma \mu_{\alpha,\mathrm{v}} + (1 - \gamma)\mu_{\alpha,\mathrm{l}}) + \beta \mu_\beta + \mu_{\mathrm{sgs}} \tag{2.2}$$

where α and β are the fuel and air volume fractions, respectively. The relationship between these two is:

$$\alpha + \beta = 1 \tag{2.3}$$

In equation 2.2, the vapour fraction is described by γ, indicating the proportion of the cells that are cavitated.

$$\gamma = \frac{\rho_{\alpha,\mathrm{lv}} - \rho_{\alpha,\mathrm{lSat}}}{\rho_{\alpha,\mathrm{vSat}} - \rho_{\alpha,\mathrm{lSat}}} \tag{2.4}$$

The code uses a Large Eddy Simulation (LES) model, which is apparent in equation 2.2 in the μ_{sgs}-term. LES is believed to be necessary in order to resolve the liquid turbulence interaction with the low turbulence in the gas phase.

In addition to the momentum equation there is the continuity equation for each phase:

$$\frac{\partial \alpha \rho_\alpha}{\partial t} + \nabla \cdot (\rho_\alpha \alpha \mathbf{U}) = 0 \tag{2.5}$$

$$\frac{\partial \beta \rho_\beta}{\partial t} + \nabla \cdot (\rho_\beta \beta \mathbf{U}) = 0 \tag{2.6}$$

where

$$\rho = \alpha\rho_\alpha + \beta\rho_\beta \tag{2.7}$$

and thus equations 2.5 & 2.6 can be combined to form

$$\frac{\partial \rho}{\partial t} + \nabla \cdot (\rho \mathbf{U}) = 0 \tag{2.8}$$

Since the code is intended to account for compressibility an equation of state (EOS) relating pressure and density is needed. There was a more detailed rationale for the EOS used in the studies presented in Paper 2, but that code does not use VOF and thus only one EOS is needed. For modelling diesel injection into air two equations of state are needed, one for liquid and one for the gas. The main reason for selecting the chosen EOS (for the liquid) is that it obeys the liquid and vapour EOS in the limit cases of pure liquid and pure vapour, and some form of mixture for the intermediate states. The gas EOS is simpler, since it is assumed to not undergo any phase-changes:

$$\rho_{\text{liq,vap}} = (1 - \gamma)\,\rho_l^0 + (\gamma\psi_\text{v} + (1 - \gamma)\,\psi_\text{l})\,p^{\text{sat}} + \psi(\gamma)\left(p - p^{\text{sat}}\right) \tag{2.9}$$

$$\rho_{\text{air}} = \psi_\text{g} p \tag{2.10}$$

Where ψ_v and ψ_l refers to the vapour and liquid compressibility, respectively. For reference, it is related to the speed of sound by:

$$a = \frac{1}{\sqrt{\psi}} \tag{2.11}$$

The constant ρ_l^0 is defined as

$$\rho_l^0 = \rho_{\text{l,sat}} - p_{\text{sat}}\psi_\text{l} \tag{2.12}$$

When the code is executed the model for ψ is chosen at runtime. Three models have been implemented: the Wallis equation [31]:

$$\psi_{\text{Wallis}} = (\gamma\rho_{\text{v,Sat}} + (1 - \gamma)\rho_{\text{l,Sat}}) \left(\gamma\frac{\psi_\text{v}}{\rho_{\text{v,Sat}}} + (1 - \gamma)\frac{\psi_\text{l}}{\rho_{\text{l,Sat}}} \right) \tag{2.13}$$

the Chung equation [32]:

$$s_{\text{fa}} = \frac{\frac{\rho_{\text{v,Sat}}}{\psi_\text{v}}}{(1 - \gamma)\frac{\rho_{\text{v,Sat}}}{\psi_\text{v}} + \gamma\frac{\rho_{\text{l,Sat}}}{\psi_\text{l}}} \tag{2.14}$$

$$\psi_{\text{Chung}} = \left(\left(\frac{1 - \gamma}{\sqrt{\psi_\text{v}}} + \frac{\gamma s_{\text{fa}}}{\sqrt{\psi_\text{l}}} \right) \frac{\sqrt{\psi_\text{v}\psi_\text{l}}}{s_{\text{fa}}} \right)^2 \tag{2.15}$$

and a linear model:

$$\psi_{\text{linear}} = \gamma\psi_{\text{v}} + (1 - \gamma)\,\psi_{\text{l}} \tag{2.16}$$

The linear model was the one chosen for this work, since it is then consistent with the VOF-method, where viscosity and mass fraction are also described by linear equations. The Wallis model represents the lower speed of sound (compressibility) in a bubbly mixture in a more physical way, but it was found to be quite unstable when used for high speed flows. When a linear compressibility model is used, the EOS for the liquid can be reduced to:

$$\rho_{\text{liq,vap}} = \rho_{\text{l,sat}} + \psi p \tag{2.17}$$

We can now return to equations 2.5 and 2.6, and form equations that are more suitable for solving for the phase fraction and densities. We can begin by separating the two equations into two components: one representing incompressible flow, and the other the compressibility effects.

$$\frac{\partial\alpha}{\partial t} + \nabla\cdot(\alpha\mathbf{U}) = -\frac{\alpha}{\rho_\alpha}\frac{D\rho_\alpha}{Dt} \tag{2.18}$$

$$\frac{\partial\beta}{\partial t} + \nabla\cdot(\beta\mathbf{U}) = -\frac{\beta}{\rho_\beta}\frac{D\rho_\beta}{Dt} \tag{2.19}$$

These two equations could be solved for α and β respectively with the right hand side as the compressible "source". However, when these equations are discretized, they will not be mass-conservative, since there is no coupling between α and β when they are solved. The way the phase fraction variables are calculated will be described later. If the two equations above are combined with 2.3 an equation for the divergence of $\mathbf{U}$ is formed:

$$\nabla\cdot\mathbf{U} = -\frac{\alpha}{\rho_\alpha}\frac{D\rho_\alpha}{Dt} - \frac{\beta}{\rho_\beta}\frac{D\rho_\beta}{Dt} \tag{2.20}$$

This equation is used with the discretized momentum equation and the equation of state (equations 2.9 & 2.10, respectively) to form the equation for pressure. An example of how this is done for a simpler code (`icoFoam`) can be found in Appendix A.1.

Equations for U and p have now been derived, and by using the equation of state, the density can be found. However, we also need an equation to convect the density for the momentum equation, which has already been defined in 2.5 & 2.6. They can be re-arranged into:

$$\frac{\partial \rho_\alpha}{\partial t} + \nabla \cdot (\rho_\alpha \mathbf{U}) = \rho_\alpha \beta \left(\frac{1}{\rho_\alpha} \frac{D\rho_\alpha}{Dt} - \frac{1}{\rho_\beta} \frac{D\rho_\beta}{Dt} \right) \tag{2.21}$$

$$\frac{\partial \rho_\beta}{\partial t} + \nabla \cdot (\rho_\beta \mathbf{U}) = \rho_\beta \alpha \left(\frac{1}{\rho_\beta} \frac{D\rho_\beta}{Dt} - \frac{1}{\rho_\alpha} \frac{D\rho_\alpha}{Dt} \right) \tag{2.22}$$

These equations are used to convect ρ and illustrate that if the material derivatives of either density is larger than the other, it will result in a negative/positive right hand side. Further, the phase densities will remain single-phase if either α or β is zero. The terms within the parenthesis on the right hand side are treated explicitly, when the equations are solved for ρ_α and ρ_β.

The last two variables that need to be solved for are the phase-fractions. The equation to be solved can be derived from 2.18 & 2.19, where the convection term is evaluated and 2.20 is used to eliminate the divergence term. This results in:

$$\frac{\partial \alpha}{\partial t} + \mathbf{U} \cdot \nabla \alpha = -\alpha\beta \left(\frac{1}{\rho_\alpha} \frac{D\rho_\alpha}{Dt} - \frac{1}{\rho_\beta} \frac{D\rho_\beta}{Dt} \right) \tag{2.23}$$

$$\frac{\partial \beta}{\partial t} + \mathbf{U} \cdot \nabla \beta = -\alpha\beta \left(\frac{1}{\rho_\beta} \frac{D\rho_\beta}{Dt} - \frac{1}{\rho_\alpha} \frac{D\rho_\alpha}{Dt} \right) \tag{2.24}$$

Unlike 2.18 and 2.19, these equations are bounded by $\alpha\beta$, and if care is taken with regard to sign of the right hand side, the boundedness can be maintained by choosing the solver to be implicit with respect to α or β, depending on the sign of the term within the parenthesis. The code only solves equation 2.23, and then calculates β through equation 2.3.

The last requirement is to find a way to maintain sharp interfaces, since when using the VOF method it is essential to ensure that the interface is not dispersed, causing cubes to lose their shape and balls to become "wiggly". This is usually done by using a compressive differencing scheme such as CICSAM [33], which unfortunately has problems to fulfil its nondisperse property when both liquid and air are flowing away from the interface (divergent flow) [33]. For this code a "counter-gradient" method was chosen. This involves not only use of a specific scheme, but also the introduction of a new term, which compresses the interface. The new term cannot be allowed to affect the solution in any other way than by compressing interfaces. It is also essential for this term to reduce to zero as the grid is refined, since the distortion of interfaces and associated problems are larger for coarse grids. By adding the term as a divergence term, the equation will still be conservative, and the term introduced will have an $\alpha\beta$ term, meaning that it will only be non-zero around interfaces. Equation 2.21 is then modified by adding the third term on the left hand side in the equation below:

$$\frac{\partial \alpha}{\partial t} + \mathbf{U} \cdot \nabla \alpha + \nabla \cdot (\mathbf{U}_c \alpha\beta) = -\alpha\beta \left(\frac{1}{\rho_\alpha} \frac{D\rho_\alpha}{Dt} - \frac{1}{\rho_\beta} \frac{D\rho_\beta}{Dt} \right) \tag{2.25}$$

The success of the model now depends on the choice of $\mathbf{U}_c$, which should only compress interfaces, and thus be directed in $\frac{\nabla\alpha}{|\nabla\alpha|}$. The method must compress interfaces even when no flow is present, i.e. when $|\mathbf{U}|$ is low. There are many options for ensuring this, but the one chosen for this code is:

$$\mathbf{U}_c = \min(c_\alpha|\mathbf{U}|, \max(|\mathbf{U}|))\frac{\nabla\alpha}{|\nabla\alpha|} \tag{2.26}$$

As mentioned above, the liquid/gas interface is maintained not only by use of a specific compressible numerical scheme but also by introducing the mentioned term. The scheme used is implemented in OpenFOAM under `interfaceCompression`, which switches between upwind and central differencing depending on the limiter function λ.

$$\lambda = \min(\max[1 - \max\{(1 - 4\alpha_\mathrm{P}(1 - \alpha_\mathrm{P}))^2, (1 - 4\alpha_\mathrm{N}(1 - \alpha_\mathrm{N}))^2\}, 0], 1) \tag{2.27}$$

where subscript P refers to the current cell value and N the neighbour cell value.

2.3 Boundary Conditions for Pressure

When modelling a high Mach-number flow, the boundary conditions become very important. If a non-reflective outlet condition is not used, pressure waves from the nozzle will bounce off the outlet boundary and destroy the physical realism of the simulation. The same is true for the inlet; using a simple fixed value for the pressure at the inlet is insufficient. Therefore special care has been applied to the boundaries.

2.3.1 Inlet

The total inlet pressure takes into account the compressibility of the mixture, as well as the calculated local velocity, as follows

$$p_\mathrm{inlet} = \frac{p_0}{(1 + \frac{1}{2}\psi(1 - \mathrm{pos}(\phi))|\mathbf{U}|^2)} \tag{2.28}$$

where: p_0 is the pressure set by the user; ϕ is a scalar volume flux on the face (for more information on what ϕ really means, see Appendix A.1); pos is a function returning the positive part of this velocity (which is a scalar); while ψ and $\mathbf{U}$ are read from the field.

2.3.2 Outlet

The non-reflective pressure boundary condition implemented in OpenFOAM is a simplification of that proposed in [34]. Input for the model is p_∞ and l_∞,

which represent the outlet pressure and relaxation length scale, respectively. The relaxation length scale is the parameter that governs how reflective the outlet will be; a low value will give a more reflective outlet than a high value. The model begins by calculating the velocity of the outgoing pressure wave:

$$w = \mathbf{U} \cdot \hat{n} + \sqrt{\frac{1}{\psi}} \tag{2.29}$$

where $\hat{n}$ is the outlet normal. The pressure wave velocity is used to calculate the pressure wave coefficient α and the relaxation coefficient b:

$$\alpha = w\frac{\Delta t}{\delta} \tag{2.30}$$

$$b = \frac{w\Delta t}{l_\infty} \tag{2.31}$$

where δ is the cell-face distance coefficient. The value of the pressure can now be calculated using these properties:

$$p_{trans} = \frac{p_0 + bp_\infty}{1 + b} \tag{2.32}$$

$$\xi = \frac{1 + b}{1 + \alpha + b} \tag{2.33}$$

where p_0 refers to the pressure at the outlet in the previous time-step. The pressure at the outlet is not set to p_{trans}, instead a mixture of p_{trans} and the pressure in the cell (p_{cell}) closest to the outlet is used.

$$p_{\text{outlet}} = \xi p_{\text{trans}} + (1 - \xi)\, p_{\text{cell}} \tag{2.34}$$

This ends the description of the multi-phase code for cavitating flow. In the results section some results obtained by applying it to water injection into a chamber are presented.

2.4   A Code for Cavitating Single-Phase Flow

A simpler, more robust code was also developed as part of the previously mentioned three-phase code for cavitating nozzles. This code simulates only cavitating liquid, and is the one used in the studies presented in Paper 2. The implementation is publicly available under the name `cavitatingFoam` in OpenFOAM 1.4.1.

A single-phase code for a cavitating fluid, is usually constructed by introducing variable density, which can be dependent on pressure and/or

temperature. If it is only dependent on pressure, the equation of state is said to be barotropic. Since it is implemented in a finite volume code, it is also convenient to assume homogenous equilibrium, which means the liquid and vapour are assumed to be always perfectly mixed in each cell. A property, γ, is introduced to describe the amount of cavitated vapour in each cell.

As mentioned above, an equation of state is required to model cavitation. In this case we have assumed the temperature is constant (in accordance with reference experiments [15]). A common barotropic equation of state is then the non-equilibrium differential equation:

$$\frac{D\rho}{Dt} = \psi \frac{Dp}{Dt} \tag{2.35}$$

This equation 2.35 can either be used directly in the continuity equation to formulate a pressure equation, or integrated to obtain the pressure as a function of the density. The latter approach has been applied by Schmidt *et al* [28]. The former approach is problematic when it comes to consistency. The former approach is complicated by the lack of consistency (since equation 2.35 is not an equilibrium equation of state) between the pressure and density obtained from it with the liquid and vapour equations of state before equilibrium is reached. Thus, until equilibrium is reached, errors from the inconsistency accumulate, and the code will not produce accurate results when it has reached equilibrium.

Like the equivalent three-phase EOS, the equation of state for the single-phase cavitation code should therefore obey the liquid and vapour equations of state both in the limit cases when there is pure liquid or pure vapour, while in intermediate cases between these states it must have some form of mixture. The two states have the following linear equations of state:

$$\rho_{\mathrm{v}} \quad = \quad \psi_{\mathrm{v}} p \tag{2.36}$$
$$\rho_{\mathrm{l}} \quad = \quad \rho_{\mathrm{l}}^{0} + \psi_{\mathrm{l}} p \tag{2.37}$$

The property that describes the proportion of liquid in each phase is γ:

$$\gamma = \frac{\rho - \rho_{\mathrm{l,sat}}}{\rho_{\mathrm{v,sat}} - \rho_{\mathrm{l,sat}}} \tag{2.38}$$

$\gamma = 1$ corresponds to a fully cavitated flow, and $\gamma = 0$ a flow without cavitation. $\rho_{v,sat}$ is calculated from

$$\rho_{\mathrm{v,sat}} = \psi_{\mathrm{v}} p_{\mathrm{sat}} \tag{2.39}$$

where ψ_v is the compressibility of the vapour. These properties together form the mixture's equalibrium equation of state:

$$\rho = (1 - \gamma)\, \rho_{\mathrm{l}}^0 + (\gamma \psi_{\mathrm{v}} + (1 - \gamma)\, \psi_{\mathrm{l}})\, p^{\mathrm{sat}}$$
$$+ \psi(\gamma)\left(p - p^{\mathrm{sat}}\right) \tag{2.40}$$

The compressibility, ψ, and choice of how it is modelled. were mentioned in section 2.2. For the single-phase code, the considerations when choosing a model are the same, and for the simulations in Paper 2 the linear model in equation 2.16 was chosen. For the mixture's viscosity, a simpler version of equation 2.2 can be used, since only one compressible phase is then present:

$$\mu_{\mathrm{f}} = \gamma \mu_{\mathrm{v}} + (1 - \gamma)\, \mu_{\mathrm{l}} \tag{2.41}$$

When a linear model is used for the compressibility, the equation of state (2.40) can be simplified to:

$$\rho = (1 - \gamma)\, \rho_{\mathrm{l}}^0 + \psi p \tag{2.42}$$

The first term governs the liquid density when γ is low. If the fluid is cavitating, the second term becomes more dominant. The first term contains the property ρ_l^0 which is:

$$\rho_{\mathrm{l}}^0 = \rho_{\mathrm{l,sat}} - p_{\mathrm{sat}} \psi_{\mathrm{l}} \tag{2.43}$$

where $\rho_{\mathrm{l,sat}}$ is the liquid density at standard conditions. The saturation density of the vapour, used earlier to calculate γ, is important for the liquid's tendency to cavitate. If $\rho_{\mathrm{v,sat}}$ is increased, ρ will not need to be so low in order to obtain a higher γ.

The relationship between density and pressure are used in the continuity equation to transform it from a density equation to a pressure equation. For reference, we have the compressible continuity equation:

$$\frac{\partial \rho U}{\partial t} + \nabla \cdot (\rho U U) = -\nabla p + (\mu_{\mathrm{f}} \nabla U) \tag{2.44}$$

$$\frac{\partial \rho}{\partial t} + \nabla \cdot (\rho U) = 0 \tag{2.45}$$

Since this is compressible flow, it is more straightforward than incompressible flow. Now, with equation 2.40 we get:

$$\frac{\partial \psi p}{\partial t} - \left(\rho_{\mathrm{l}}^0 \frac{\partial \gamma}{\partial t} + (\psi_{\mathrm{l}} - \psi_{\mathrm{v}})\, p_{\mathrm{sat}}\right) \frac{\partial \gamma}{\partial t}$$
$$- p_{\mathrm{sat}} \frac{\partial \psi}{\partial t} + \nabla \cdot (\rho U) = 0 \tag{2.46}$$

This equation can be combined with the numerical discretization of the momentum equation to obtain the continuity equation for pressure. This equation is solved in conjunction with the momentum equation in a PISO loop, as normal. This code does not use any turbulence model, instead it relies on stabilizing numerical schemes. This can be regarded as implicit LES if small cells are used.

2.4.1 Development of Injection Model

These simulations were originally intended to provide input for the development of a new injection model for Euler-Lagrangian diesel spray simulations. The features of interest were the ways in which cavitation layer thickness, velocity profile, velocity fluctuations and the discharge coefficient vary with changes in injection pressure, curvature of the inlet, $\frac{L}{D}$, etc.

A schematic diagram of the development of a cavitation layer in a nozzle can be seen in figure 2.1. The size of the cavitation layer is the size of the vapour layer close to the wall, and it ends where the liquid core begins. This distinguishes it from the boundary layer, which is located where the freestream velocity is reached.
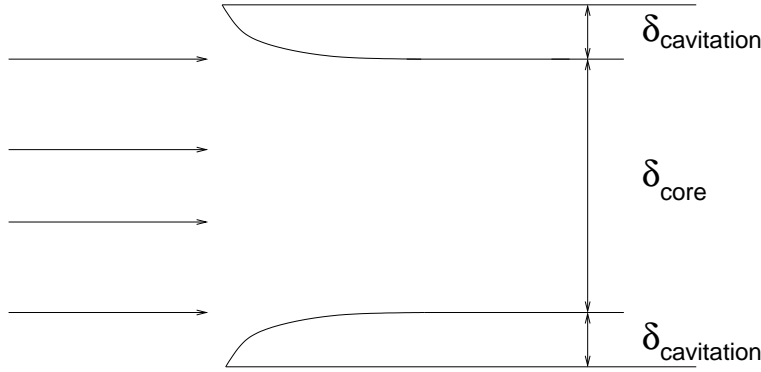

Figure 2.1: Schematic diagram of a cavitation profile, and cavitation layer classification

The theory behind the model is that if the cavitation layer ($\delta_{cavitation}$) is thin, there will be more mass in the centre of the injector, and the model will return large initial droplets. Since large droplets are assumed to originate from the centre of the spray, this could also result in a smaller spray angle. Smaller droplets are then formed from the cavitation layer itself, and the distance they move from the spray axis is governed by the turbulence in the nozzle. Thus, a thin cavitation layer can still result in a large spray angle, if the turbulence is sufficiently high.

This assumption and the points raised in the brief discussion on the cavitation layer have all been mentioned before in the literature ([35],[36]). However, Huh [35] only considers the results of turbulence, and the Max Planck Institute (MPI) model, described in [36], only considers the effect of cavitation in the

nozzle. The aim of the new model was to account for both cavitation and turbulence, and to estimate their magnitude using CFD.

During the course of the project, several attempts were made to simulate cavitating diesel nozzle flow. Initially, the equation of state in the code assumed that the vapour density was proportional to the pressure. The code worked well for water injections into gas at atmospheric air pressures, but for diesel pressures it caused the vapour density to rise above the liquid density. This forced the use of a unphysically high saturation pressure to avoid negative pressures in the solution and allow the vapour density to remain below the liquid density. Attempts were made to extend this code to use Peng-Robinson equation of state (EOS) [37], but the EOS was not sufficiently smooth to handle the large pressure gradients in the flow. The compressibility model was also changed, from the Wallis [31] model to a linear compressibility model. The change was necessary partly to enhance stability and partly because the same cavitation model was to be used for the multi-phase code handling diesel vapour, liquid and air, as mentioned earlier. Since a linear combination of the vapour fraction (γ) and liquid/gas fraction (α and β) is highly suitable for describing the mixture's properties in such cases, the same model was used for the single-phase code. A similar story of cavitation code development is reported in [38]. It starts off by using what the papers refers to as the Schmidt model [28], and ends in a modification of that model with a cut-off for negative pressures.

The combined effects of these factors caused long delays in the simulations, and forced the author to limit the work to validating a model for cavitating single-phase flow, without being able to develop a model for Lagrangian diesel spray simulations.[1]

---

[1]It should also be noted that it is only in special cases (mainly sprays with low evaporation, e.g. in cold starts) that the size of the initial droplets and their maximum spreading angle really affect the combustion. This issue will be addressed in section 4.2.1

Chapter 3

Spray Modelling

In section 1.2, Lagrangian spray simulations were briefly described. The
method used to introduce Lagrangian particles into an Eulerian grid is
sometimes called the discrete droplet model (DDM). This is based on the fact
that we cannot resolve the full details of the near-nozzle flow using only
Eulerian cells (as yet at least). A typical nozzle has a diameter of around
200 μm, so if it is to be resolved properly a cell size of about 20 μm is needed,
but even if such small cells are only used around the injector the number of
cells required grows enormously if the calculations are run in 3D. Thus, the
spray is usually modelled in some other way. There has been a growing
number of attempts to simulate sprays using a full Eulerian approach, or by
using LES instead of the classical DDM with a k-ε turbulence model. These
attempts are often associated with some limitations. For instance, de Villiers
et al [39] considers primary breakup close to a non-cavitating nozzle, Befrui *et
al* [40] uses an updated version of the same code to study primary breakup in
non-cavitating gasoline direct injection, and Ménard *et al* [41] considers liquid
injection into incompressible air with a velocity of around 100 m/s. A spray
study using LES and an Euler-Lagrangian description of the gas and liquid
has also been published, by Vuorinen *et al* [42]. They also used lower velocities
than those of diesel sprays and assumed the surrounding air to be
incompressible, but the Reynolds number was comparable to those of diesel
sprays. However, they did not simulate the near-nozzle behaviour, and mainly
focused on studying the spray behaviour. All the papers mentioned above,
ignore cavitation, and the simulations cover only part of the relevant physical
domain.

One of the biggest problems associated with the DDM is modelling the
near-nozzle flow, more specifically the conditions close to the injector. In this
region a liquid core forms from the liquid fuel being injected through the
injector. Ligaments are separated from this liquid core and form droplets that
evaporate and mix with the ambient gas. Hence, since the DDM assumes
disperse flow with spherical droplets of liquid, it is not an accurate
representation of the spray in this region. An option to improve near-injector
flow is to use the previously mentioned (in section 2.1) ELSA model. Aside

from the work by [24] (mentioned in 2.1), Blokkeel *et al* [43] and Lebas *et al* [44] have also used it to improve the primary breakup of the spray. Since the DDM model is only used when the liquid fraction is low, representing a state in which droplets (not ligaments) have been formed from the liquid core, the model gives a better representation of the near-nozzle flow. Another benefit is that such a modelling concept does not require a primary atomization model, and thus there are fewer model constants to tune. However, this raises some of the problems associated with high grid resolution to resolve the nozzle mentioned earlier. There have also been other attempts to simulate sprays using only Eulerian cells, in 2D ([45]). However, the Eulerian-Lagrangian description of the diesel spray has been the most widely used.

The large number of sub-models used to simulate the various physical processes that the parcels are subjected to before they become part of the gas can pose further problems when using the DDM model. Each of these models will be thoroughly described later in this chapter, but here my intention is to mention the interactive problems they raise as a group. For instance, even if the breakup model is fully correct, the parcels can become too small due to the evaporation model simulating evaporation too quickly, thus nullifying the excellence of the breakup model. Similarly, a perfect turbulence interaction can be ruined by a dissipative numerical scheme, or an overpredicting drag model that slows all the parcels down too much. Therefore, tuning the spray model in a non-combusting environment to constant volume experimental data, and then applying the results of the tuning to real engine calculations often yields poor results. The complex interactions amongst all of the sub-models make spray simulation somewhat more of an art than a science.

3.1   The Gas Phase

3.1.1   Basic Equations

The Eulerian grid is used to discretise the conservation equations of the fluid phase. When chemical reactions and interactions between the Lagrangian and Eulerian phases are also involved, Eq. 2.8 needs to be extended to include liquid spray evaporation. Furthermore, the density ρ becomes more complex since diesel combustion involves multiple species, all of which affect the density. In addition, since chemical reactions are occuring various compounds will be formed and participate in further reactions, so the mass fraction of each species is not conserved. However, if we consider the total density, the only source term ($\dot{\rho}^s$) is from spray evaporation.

$$\frac{\partial \rho}{\partial t} + \nabla \cdot (\rho \mathbf{U}) = \dot{\rho}^{\text{s}} \tag{3.1}$$

The evaporation source term is calculated from the evaporation sub-model, which will be described later. As already mentioned, each species will be transported, by both diffusion and convection, and may also be formed or

consumed by the reactions. The mass fraction for species i is denoted by Y_i, and its transport equation is:

$$\frac{\partial \rho Y_i}{\partial t} + \nabla \cdot (\rho U Y_i) - \nabla \left((\mu + \mu_{\mathrm{T}})\nabla Y_i\right) = \dot{\rho}^{\mathrm{s}_i} + \kappa \mathbf{R}\mathbf{R}_i \tag{3.2}$$

$$\dot{\rho}^{\mathrm{s}} = \sum_i \dot{\rho}^{\mathrm{s}_i} \tag{3.3}$$

since most fuels consist of multiple species, and when combustion occurs their number increases dramatically. For instance, when the mechanism including 83 species was used for the calculations shown in Paper 3, the transport equation had to be solved 83 times in each time iteration. The momentum equation also needs to be modified due to the presence of a Lagrangian spray. Presented here is the equation for the mean velocities using a Reynolds Average Navier Stokes assumption:

$$\frac{\partial \rho \mathbf{U}}{\partial t} + \nabla \cdot \left(\rho \mathbf{U}^{\mathrm{T}}\mathbf{U}\right) = -\nabla p + \nabla \cdot \left((\mu + \mu_{\mathrm{T}})\frac{1}{2}(\nabla \mathbf{U} + (\nabla \mathbf{U})^{\mathrm{T}})\right) + \rho \mathbf{g} + \mathbf{F}^{\mathrm{s}} \tag{3.4}$$

$\mathbf{F}^s$ is the spray momentum source term.

3.1.2 Turbulence Modelling

Since the goal of this project was to develop new models for industrial applications, the turbulence was modelled using k-ε models. Paper 1 presents constant volume vessel simulations of diesel sprays conducted using three different turbulence models, which yielded results that substantially differed in terms of spray shape and penetration of liquid and vapour. For later simulations different turbulence models were also tested, bearing in mind the intial results. The discrepancies between the models indicate the importance of modelling the turbulence correctly.

The three (compressible) models used in Paper 1 were: standard k-ε [46], Renormalized Group k-ε [47] (RNG) and Launder-Sharma's k-ε (LS) [48] models. Each of the three turbulence models was developed with a different rationale. The RNG model and the standard k-ε model used for these cases are both high Reynolds number models, meaning that they apply wall functions for the near wall cell. The Launder-Sharma turbulence model differs in this respect, since it is a low Reynolds number model, and has no wall functions. This places higher demands on the near-wall cell size, but since all computations in this work simulated events in a bomb, the near-wall behaviour was not as important as the spray interactions by any of the walls except the injector-wall.

The first turbulence model based on k and ε was originally presented in [46]. It is shown in equations 3.5 and 3.6 in a general form to accommodate the three turbulence models.

$$\frac{\partial}{\partial t}(\rho k) + \nabla \cdot (\rho k \mathbf{U}) - \nabla \cdot [(\alpha_k \mu_\mathrm{T} + \mu)\nabla k] =$$

$$= 2\mu_\mathrm{T}\mathrm{S} - \frac{2}{3}\rho k \nabla \cdot \mathbf{U} - \rho\varepsilon - D_i \qquad (3.5)$$

$$\frac{\partial}{\partial t}(\rho\varepsilon) + \nabla \cdot (\rho\varepsilon\mathbf{U}) - \nabla \cdot [(\alpha_\varepsilon \mu_\mathrm{T} + \mu)\nabla\varepsilon] =$$

$$C_1 2\mu_\mathrm{T}\mathrm{S}\frac{\varepsilon}{k} - \frac{2}{3}C_1\rho\varepsilon\nabla \cdot \mathbf{U} - C_2\rho\frac{\varepsilon^2}{k} + B_i \qquad (3.6)$$

where B_i and D_i are listed below. Numerical constants and other variables are listed in Paper 1.

i	B_i	D_i
k-ε	$-C_3\rho\varepsilon\nabla \cdot \mathbf{U}$	0
RNG	$-2\mu_\mathrm{T}\mathrm{R}_\mathrm{RNG}\mathrm{S}\varepsilon/k$	0
LS	$-C_2 f \rho\frac{\varepsilon^2}{k} + 2\mu\mu_\mathrm{T}\frac{|\Delta\mathbf{U}|^2}{\rho}$	$2\mu|\nabla\sqrt{k}|^2$

Table 3.1: Specific terms of each turbulence model

3.1.3   Turbulence/Spray Interaction

There is no liquid spray source term in equations 3.5 & 3.6, so the turbulence is not directly affected by the presence of particles. Different researchers have adjusted their models in different ways to incorporate the effects of particles on turbulence. Including a source term in the equations is the most common way to achieve this, but not the only one. An example of a model that uses a source term in the equations for the turbulent quantities is KIVA ([49]). However, that term can only reduce the kinetic energy of the turbulence, which is not consistent with the conclusions drawn from experiments by Crowe *et al* [50, 51], see figure 3.1.

According to experimental investigations of gas-solid and gas-liquid flows summarized in 3.1, the property $\frac{d}{l_t}$ affects whether particles will increase or decrease the intensity of the turbulence. A value above 0.1 indicates that the intensity of the turbulence will increase, and a value below the opposite. For most diesel spray simulations, the length scale[1] l_t is of the order of 100 μm in cells where there are parcels, and the droplet diameter ranges from 100 μm (depending on the size of the injector) down to about 1 μm (there may of course be smaller droplets than this, but they will quickly evaporate). Figure 3.2 shows the distribution of the quantity $\frac{d}{l_t}$, centered around 0.1, indicating that some parcels will increase, and others reduce, the turbulence.

---

[1]According to the k-ε turbulence model, which might not predict the turbulence entirely correctly.
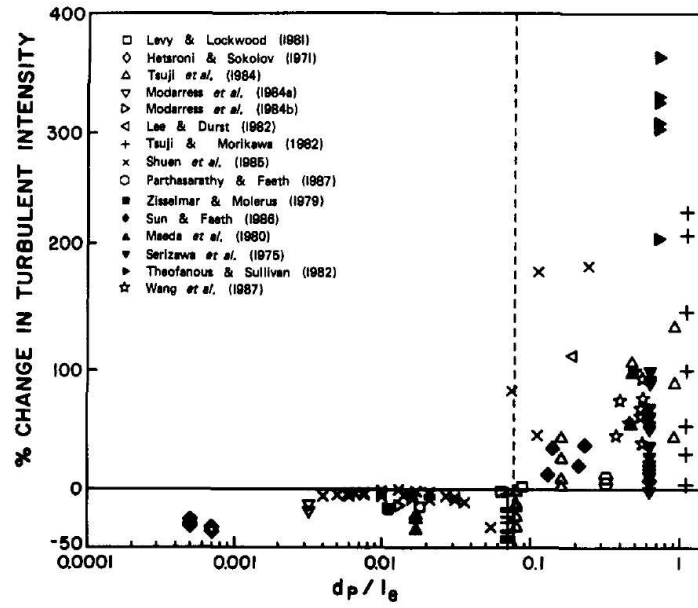
Figure 3.1: Changes in turbulent intensity as a function of length scale ratio. Reprinted from [50] with permission from Elsevier Ltd.
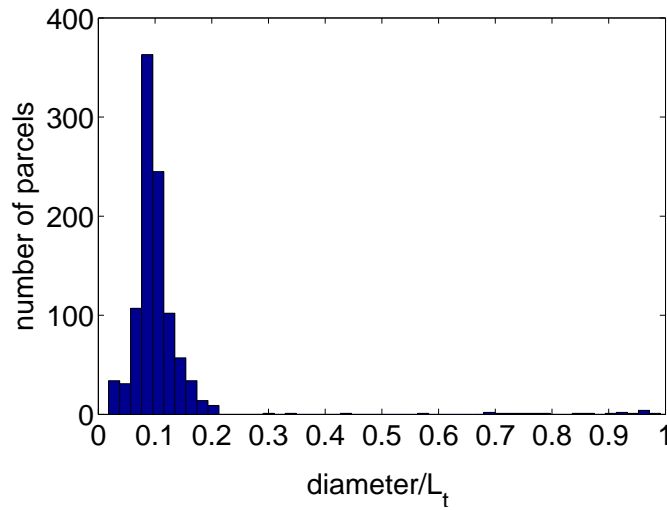

Figure 3.2: Distribution of parcels from five spray simulations obtained using different turbulence models, both combusting and non-combusting. The total number of parcels was 1018, and L_t was approximated to 100 μm

Aside from using new terms in the turbulence model, there are other ways to account for the presence of droplets in a simulation. For instance, one of a list of suggestions for improving the performance of spray simulations in a book by Stiesch [12] is to limit the length scale of the gas phase turbulence inside the

spray to the jet diameter in order to reduce the grid dependency of the calculations. Such a modification would also cause the turbulence model to be affected by the particles. However, the suggestion raises several problems. Notably, the jet diameter is not well defined, it could refer solely to the liquid part of the spray, or the vapour part could also be included. Similarly, the term "inside the spray", could refer to just the liquid core, or include the vapour cloud.

The author chose to limit the turbulent length scale to the nozzle diameter in cells with parcels. The spray is a cloud of parcels, and all cells that have parcels in them must be inside this cloud. There can be cells that do not have a parcel in them, but if we choose a high number of injected parcels there will be few such cells. The nozzle diameter is selected rather than the jet diameter because the nozzle diameter is the parameter that initially sets the length scale of the turbulence. Fixing the limit prevents the turbulence length scale from growing, but it also simplifies the calculations, since calculating the jet diameter in every timestep would be costly. Thus, the nozzle diameter is a good first approximation.

k governs the scale of the fluctuating turbulent velocity, and ε the size of the turbulent eddies. The limit was thus imposed on ε. The length scale of the turbulence is defined as:

$$l_{\mathrm{t}} = C_{\mu}\frac{k^{3/2}}{\varepsilon} \tag{3.7}$$

Thus, since the limit was imposed on ε, it was limited by:

$$C_{\mu}\frac{k^{3/2}}{L_{\mathrm{sgs}}} < \varepsilon \tag{3.8}$$

Where L_{sgs} is set to the nozzle diameter. The constraint is imposed after the equations for k and ε are solved. If the constraint is applied before any of the equations are solved, the constraint in equation 3.8 cannot be guaranteed.

The modification of the turbulence model implies an assumption regarding ε; that the equation for ε underestimates the dissipation when liquid parcels are present. One could also think of this as over-prediction of the length scale of the spray, which is perhaps easier to imagine, and this explanation will be used in the rationale below.

The parcels in a diesel spray problem have fairly high velocities, and the increased momentum of the gas comes from the spray. Thus, the resulting length scale of the turbulence should also be governed by the spray and nozzle size, which is what this modification does. One could argue that this only shifts the dependency from the grid to the magnitude of the turbulence length scale limit. While this is true, it is a much cheaper dependency computationally.

3.1.4 Chemistry

After the fuel liquid droplets have undergone breakup and evaporation, the fuel mixes with the surrounding air and forms a combustible mixture. A real diesel fuel consists of about 1000 different species, reacting with the air in over 10 000 reactions. Thus, when studying combustion, either experimentally or numerically, the complexities are generally reduced by considering the combustion of a simpler model fuel. One such model fuel is n-heptane, another is the IDEA model fuel consisting of n-decane and α-methyl-naphthalene. Both have been used in this work: IDEA for the spray studies described in Paper 1, and n-heptane for the studies described in Papers 3 and 4.

Solving the chemistry numerically means solving a large system of reaction equations. For each reaction

$$S_{11}^f[X_1] + S_{21}^f[X_2] + ... \rightarrow S_{11}^r[X_1] + S_{21}^r[X_2] + ... \tag{Re. 1}$$
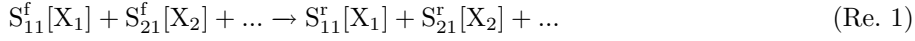
there is a corresponding reaction rate equation which determines how rapidly the reaction is proceeding and in which direction. To formulate the reaction in a more general manner, reaction j is written as:

$$\sum_{i=1}^{N_s} S_{ij}^f[X_i] \overset{k_j^f}{\underset{k_j^r}{\rightleftharpoons}} \sum_{i=1}^{N_s} S_{ij}^r[X_i] \tag{Re. 2}$$

where S^f and S^r are the matrices of forward and reverse stoichiometric coefficients, respectively, k_j^f and k_j^r are the corresponding reaction rate constants of reaction j, and $[X_i]$ is the molar concentration of species i in the cell. The matrix of stoichiometric coefficients consists of N_s rows, with the rows corresponding to species. The columns represent reactions, making the matrix $N_s \times N_r$. The reaction rate constant k is itself a function of the Arrhenius constants:

$$k_j = A_j T^{\beta_j} e^{-\frac{E_{a,j}}{RT}} \tag{3.9}$$

which need to be specified as part of the mechanism. It is now possible to write the equation for the reaction rate of the basic reaction, Re. 1. The rate of formation of species $[X_1]$ from reaction j is written as:

$$\left(\frac{d[X_1]}{dt}\right)_j = S_{1j}^r \left(k_j^f \prod_{i=1}^{N_s} [X_i]^{S_{1j}^f} - k_j^r \prod_{i=1}^{N_s} [X_i]^{S_{1j}^r}\right) \tag{3.10}$$

This equation is formulated for every species included in the chemical mechanism, as well as for every reaction, resulting inn an equation system

consisting of $N_s \times N_r$ equations. As can be seen from the above equation, it is a system of Ordinary Differential Equations (ODEs), which can be solved coupled using an ODE solver, sequentially using a *reference species technique* [52], or by an Euler-Implicit method. OpenFOAM has the ability to solve the equations using an ODE solver (an approach used in Paper 3). Some versions of KIVA-3V also offer the option of solving the chemical rate reactions coupled, one of them being the KIVA-3V version also used in Paper 3. Aside from the concentrations, it is also important to find the right hand side of equation 3.10, since it is used in the source term in the transport equation (equation 3.2). The source term for species i is:

$$\mathbf{RR}_i = \frac{W_i}{\rho} \sum_{j=1}^{N_r} (S_{ij}^r - S_{ij}^f)\dot{\omega}_j \tag{3.11}$$

$$\dot{\omega}_j = k_j^f \prod_{i=1}^{N_s} [X_i]^{S_{ij}^f} - k_j^r \prod_{i=1}^{N_s} [X_i]^{S_{ij}^r} \tag{3.12}$$

As mentioned, a real mechanism for hydrocarbon fuels (including model fuels) would be very large. While it is possible to use such mechanisms in shock tube simulations, they are too large to use in a CFD simulation. As mentioned in the above section, each reaction requires a term describing the amounts of each species it forms, and each species requires a transport equation to be solved. One example of a sufficiently small mechanism is the reduced one used in Paper 3, consisting of 338 reactions and 83 species. This mechanism has to solve 83 systems of ODEs in every cell, in every timestep. Some of the equations in the system will not be applicable, since no reaction includes all species, but in theory the system could comprise 28054 ODEs in total.

To solve the chemical reaction equations, a stiff ODE solver is needed. The one used in the studies presented in Paper 3 is the SIBS method (Semi-Implicit Bulirsch Stoer [53]) in OpenFOAM, which is based on Richardson extrapolation of the approximated solution. As mentioned earlier the solver needs to solve ODEs in every timestep to determine the chemical species' concentrations at the end of the timestep. The Richardson extrapolation of the function y assumes that as the interval (in our case the computational timestep Δt) is split up into increasing number of sub-steps, the solution will converge to some value y_∞. However, the solver will never apply enough sub-steps to find it. Instead, it will approximate it, depending on the solution using large sub-steps. The analytical function used to approximate y_∞ is a polynom, and the error function of the method contains only even terms of the step size.

Chalmers PaSR Model

It is necessary to use some form of treatment for the chemistry and turbulent mixing, in the literature there are many suggestions for doing this, including: PaSR ([54]), diffusion flamelets [55], detailed chemical kinetics with a perfectly-stirred reactor [56], and the general flame surface density model [57].

However, the Chalmers PaSR model was used to model the turbulence - chemistry interaction in Paper 3.

The PaSR model is based on the theory that real flames are much thinner than any computational cell, so assuming that an entire cell is a perfect reactor is a severe overestimation. Thus, the cells are divided into a reacting part, and a non-reacting part. The reacting part is treated like a perfectly stirred reactor, in which all present species are homogeneously mixed and reacted. After reactions have taken place, the species are assumed to be mixed due to turbulence for the mixing time τ_{mix}, and the resulting concentration gives the final concentration in the entire, partially stirred, cell. The relative sizes of the parts of the computational cell constituting the reactor and the rest of the cell, are governed by the turbulent mixing time and the residence time (the numerical time step, τ, in our case). The reaction rate term for species i is then approximated as:

$$\frac{\partial c^i}{\partial t} = \frac{c_1^i - c_0^i}{\tau} = \kappa \mathbf{RR}_i(c_1^i) \tag{3.13}$$

Where $\mathbf{RR_i}(c_1^i)$ is the laminar chemical source term, and κ the reaction rate multiplier, defined as:

$$\kappa = \frac{\tau_{\mathrm{c}}}{\tau_{\mathrm{c}} + \tau_{\mathrm{mix}}} \tag{3.14}$$

where τ_{mix} is the turbulence timescale mentioned above, and τ_{c} the corresponding chemical timescale. This factor appears in the species transport equation with the chemical source term (as in equation 3.2):

$$\frac{\partial \rho Y_i}{\partial t} + \nabla \left(\rho Y_i \mathbf{U} \right) - \nabla \left(\mu_{\mathrm{Eff}} \nabla \left(Y_i \right) \right) =$$
$$= \mathbf{S}_i + \kappa \mathbf{RR_i}(c_i) \tag{3.15}$$

where τ_{mix} is the turbulence timescale mentioned above, it is assumed to be determined by k and ε:

$$\tau_{\mathrm{mix}} = C_{\mathrm{mix}} \frac{k}{\varepsilon} \tag{3.16}$$

with $C_{\mathrm{mix}} = 0.03$. The chemical timescale is determined by solving the reaction system's ODEs fully coupled, and finding the characteristic time for that system. Other variations and detailed derivations of the PaSR model can be found in [52, 54, 58, 59].

3.2 Spray Sub-Models

3.2.1 Spray Motion Equation

The motion of a Lagrangian particle, moving in an Eulerian framework, is governed by one of the most fundamental laws of physics; Newton's second law:

$$\frac{\partial \mathbf{p}_{\mathrm{d}}}{\partial t} = \sum_i \mathbf{F}_i \tag{3.17}$$

Unfortunately, this equation cannot be solved immediately, simply because the force acting on the parcel is unknown. The full spray equation, often referred to as the BBO equation - from Basset (1888), Boussinesq (1903) and Oseen(1927) - includes effects of added mass, pressure, Basset force[2], Magnus effect[3], Saffman force[4], and Faxén[5] force. They are all neglected. Most of the terms can be neglected due to the high density ratio between the two phases, while others like the Magnus effect are neglected since rotation of the droplets will not be very important. What remains are the forces due to drag and gravity acting on the droplets. The latter is included for simplicity and the former due to its physical importance. These simplifications allow us to write the right hand side of equation 3.17 as:

$$\frac{\partial \mathbf{p}_{\mathrm{d}}}{\partial t} = -\rho_{\mathrm{g}} \frac{\pi D^2}{8} C_{\mathrm{D}} \left(\mathbf{u}_{\mathrm{d}} - \mathbf{U}\right) |\mathbf{u}_d - \mathbf{U}| + \rho_{\mathrm{d}} \frac{\pi D^3}{6} \mathbf{g} \tag{3.18}$$

This equation can be simplified further, if we assume the droplets are spherical, and that the drag will not be affected by changes in mass, then:

$$\frac{\partial \mathbf{p}_{\mathrm{d}}}{\partial t} = m_{\mathrm{d}} \frac{\partial \mathbf{u}_{\mathrm{d}}}{\partial t} = \rho_{\mathrm{d}} \frac{\pi D^3}{6} \frac{\partial \mathbf{u}_{\mathrm{d}}}{\partial t} \tag{3.19}$$

A droplet's mass will of course change with time (due to breakup & evaporation), but we assume that the changes will not affect the drag. This means we can neglect the effect that causes rockets to liftoff and airplanes to fly, an effect that is not believed to be pronounced in diesel droplets from which some mass is evaporating. If we combine equations 3.18 and 3.19, the result is:

$$\frac{\partial \mathbf{u}_{\mathrm{d}}}{\partial t} = -\frac{3}{4} \frac{\rho_{\mathrm{g}}}{\rho_{\mathrm{d}}} \frac{1}{D} C_{\mathrm{D}} \left(\mathbf{u}_{\mathrm{d}} - \mathbf{U}\right) |\mathbf{u}_{\mathrm{d}} - \mathbf{U}| + \mathbf{g} \tag{3.20}$$

To simplify this equation further, a momentum relaxation time is introduced:

---

[2]This is the force that causes a motorboat to continue in its path even when the motor has been switched off recently.

[3]The force that causes a soccer ball to rotate perfectly past defenders and into the net

[4]Lift force due to shear

[5]force due to curvature of the flow

$$\tau_{\mathbf{u}} = \frac{8m_{\mathrm{d}}}{\pi \rho_{\mathrm{g}} C_{\mathrm{D}} D^2 |\mathbf{u}_{\mathrm{d}} - \mathbf{u}|} = \frac{4}{3} \frac{\rho_{\mathrm{d}} D}{\rho_{\mathrm{g}} C_{\mathrm{D}} |\mathbf{u}_{\mathrm{d}} - \mathbf{u}|} \tag{3.21}$$

Equation 3.20 can now be written as:

$$\frac{\partial \mathbf{u}_{\mathrm{d}}}{\partial t} = -\frac{\mathbf{u}_{\mathrm{d}} - \mathbf{U}}{\tau_{\mathbf{u}}} + \mathbf{g} \tag{3.22}$$

Even with the introduction of $\tau_{\mathbf{u}}$, the drag cannot be approximated without a drag coefficient, which will be introduced in a later section in this chapter.

3.2.2 Parcel Tracking

In Lagrangian spray simulations, the particles representing liquid are moving in a fixed Eulerian framework as described above. Tracking them and defining the cells they are in are clearly important issues. There are two main ways of doing this, one called the *Lose-Find* algorithm, and one called the *Face-To-Face* algorithm.

The *Lose-find* algorithm is fairly simple and can be described in four steps.

1. Update the properties of the parcel
2. Move the parcel with velocity $\mathbf{u_d}$ for time Δt
3. Find out which cell the parcel is in
4. Add momentum to the cell to which the parcel has moved

Assuming that the time step is sufficiently small to ensure that every parcel traverses more than one cell, this approach is acceptable. However, even for a small time step, a parcel can still be moved across a cell without having any momentum exchange with it. The model is used in KIVA-3V, as well as some commercial CFD codes. Due to the problems mentioned above, however, another model is used in OpenFOAM; *Face-To-Face* tracking. It too can be described in four steps:

1. Move the parcel until it reaches a cell boundary or for the entire time step Δt if it remains in the same cell
2. If the parcel changes cell, calculate the time it took to move out of the first cell, and update the parcel properties
3. Add the momentum-change to the cell that the parcel has been in
4. If the parcel still has time left to move, go back to 1.

The *Face-To-Face* tracking in OpenFOAM includes a stability check that begins by tracking the parcel from the centre of the cell it belongs to, rather than from the particle's position. This is done to ensure that particles that might be close to the edge of the cell (or even slightly outside) are properly tracked.

Parcels tracked by *Face-To-Face* tracking cannot 'skip' cells, which improves the predictions of transfer of mass, momentum and energy. For a more detailed description, see [60].

3.2.3   Injection Model

The injection model used in the Lagrangian spray simulations is a solid-cone injection model. The user supplies a drop diameter probability density function (PDF) with parameters, in this case a Rosin-Rammler form was chosen. The model also requires minimum and maximum values for the droplet size, as well as the maximum spray cone angle. The parameters for the model can be found in table 3.2

Model parameter	Numerical Value
d_{min}	10^{-6} m
d_{max}	d_{nozzle}
d_{mean}	d_{nozzle}
n	3
β_{max}	20

Table 3.2: Solid cone injection model constants

The direction of a droplet to be injected into the domain is calculated by multiplying β_{max} and a random number between 0 and 1. This angle is the angle between the set spray direction and the direction of the injected droplet. Note that β_{max} is not the half-angle of the spray, but the full spray angle. The velocity of the injected parcel is based on the injection pressure, and the pressure in the domain:

$$\mathbf{u}_{\mathrm{d}} = C_{\mathrm{d}}\sqrt{\frac{2\Delta p}{\rho_{\mathrm{i}}}} \tag{3.23}$$

where ρ_i is the density of the injected parcel, taking the type of fuel, injection pressure, and composition of fuel (for multi-component fuels) into account. C_d is the discharge coefficient, a parameter that varies from nozzle to nozzle, and is to a certain degree pressure-dependent [15].

3.2.4   Drag Model

Several options for the drag coefficient have been suggested in the literature ([36],[61],[62]), but the one chosen here was:

$$C_{\mathrm{D}} = \begin{cases} \frac{24}{\mathrm{Re_d}}\left(1 + \frac{\mathrm{Re_d}^{\frac{2}{3}}}{6}\right) & \mathrm{Re_d} < 1000 \\ 0.44 & \mathrm{Re_d} > 1000 \end{cases} \tag{3.24}$$

OpenFOAM also offers the possibility to account for changes in drag due to oscillations of the droplet surface, i.e. the instability waves eventually resulting in droplet breakup. If this model is used, the TAB model [9] will be used to calculate the oscillations and the resulting drag will be added to the drag described above. The modification is

$$C_{\mathrm{D}} = C_{\mathrm{D,model}}(1 + C_{\mathrm{D,distort}}\min(y_{\mathrm{lim}}, y)) \tag{3.25}$$

where $C_{\mathrm{D,distort}}$ and y_{lim} are user-set constants, and y is the relative deviation from the equator of the parcel if it were spherical. y_{lim} is usually set to 1.0. The minimum function is not necessary when the TAB breakup model is used, since a y-value of 1.0 will result in the parcel breaking up.

3.2.5 Breakup Model

The breakup model used is the Kelvin-Helmholtz-Rayleigh-Taylor (KHRT) model ([8] & [63]). This model, along with the TAB model, is one of the most widely used models in Lagrangian spray simulations today ([64],[65],[66]). The KHRT model was chosen for its superior performance under diesel conditions ([67]). It is also possible to use the TAB model, but often in conjunction with some form of atomization model since the TAB model tends to break up the droplets very rapidly. The KHRT model includes two modes of breakup: KH breakup, accounting for unstable waves growing on the liquid jet due to the differences in velocity between the gas and liquid; and RT breakup, accounting for waves growing on the droplets' surface due to acceleration normal to the droplet-gas interface. Analysis of a round liquid jet yields a fastest growing wave with a wavelength (Λ_{KH}) and a growth rate (Ω_{KH}):

$$\Lambda_{\mathrm{KH}} = 9.02 \frac{r(1 + 0.45\mathrm{Oh}^{\frac{1}{2}})(1 + 0.4\mathrm{Ta}^{0.7})}{(1 + 0.865\mathrm{We}^{1.67})^{0.6}} \tag{3.26}$$

$$\Omega_{\mathrm{KH}} = \frac{(0.34 + 0.38\mathrm{We}^{\frac{3}{2}})}{(1 + \mathrm{Oh})(1 + 1.4\mathrm{Ta}^{0.6})} \sqrt{\frac{\sigma}{\rho_{\mathrm{d}}r^3}} \tag{3.27}$$

The critical droplet radius r_{c}, which is the radius a parcel will have after it has been stripped off the liquid jet, is assumed to depend linearly on the wavelength Λ_{KH} and the stripping rate, or characteristic breakup time τ_{KH} (which controls the breakup rate) is assumed to be a simple function of the growth rate Ω_{KH}, wave-length Λ_{KH} and droplet radius, r:

$$r_{\mathrm{c}} = B_0\Lambda_{KH} \tag{3.28}$$

$$\tau_{\mathrm{KH}} = \frac{3.726B_1 r}{\Omega_{\mathrm{KH}}\Lambda_{\mathrm{KH}}} \tag{3.29}$$

The continuous reduction of droplet size due to breakup can then be defined by the rate equation:

$$\frac{dr}{dt} = -\frac{r - r_{\mathrm{c}}}{\tau_{\mathrm{KH}}} \tag{3.30}$$

which essentially describes how rapidly the drops will reach the stable state. The breakup parameters B_0 and B_1 can be found in Table B.1. In addition to these two constants, there are two more parameters to control the KH breakup. The first determines whether breakup will occur at all. If $We < We_{\mathrm{limit}}$, the drop has reached a stable state and no breakup due to Kelvin Helmholtz instabilities will occur. The second parameter controls the rate of introduction of new child-parcels. As the jet breaks up the parcel will accumulate a *stripped mass*, m_{s}, and when m_{s} exceeds a certain percentage of the average parcel mass, which is the total injected liquid mass divided by the total number of injected parcels, a new parcel will be introduced with size r_{c}, containing the accumulated mass m_{s}.

Rayleigh-Taylor breakup, on the other hand, is governed by how rapidly disturbances grow on the surface of the droplet. For real droplets these disturbances originate from the droplets' trailing edges [12]. If these disturbances are assumed to be linear, the frequency of the fastest growing wave, and the corresponding wavelength, is given by:

$$\Omega_{\mathrm{RT}} = \sqrt{\frac{2|g_{\mathrm{t}}(\rho_{\mathrm{l}} - \rho_{\mathrm{g}})|^{1.5}}{3\sqrt{3}\sigma(\rho_{\mathrm{g}} + \rho_{\mathrm{l}})}} \tag{3.31}$$

$$g_{\mathrm{t}} = (\mathbf{g} + \frac{d\mathbf{u}_{\mathrm{d}}}{dt}) \cdot \frac{\mathbf{u}_{\mathrm{d}}}{|\mathbf{u}_{\mathrm{d}}|} \tag{3.32}$$

$$\Lambda_{\mathrm{RT}} = 2\pi C_{\mathrm{RT}} \sqrt{\frac{3\sigma}{|g_{\mathrm{t}}(\rho_{\mathrm{l}} - \rho_{\mathrm{g}})|}} \tag{3.33}$$

Where C_{RT} is a modelling parameter. If this wavelength of the fastest growing wave is smaller than the diameter of the droplet diameter and the perturbations are allowed to grow for a period of time, the droplet will be immediately converted into a parcel with smaller droplets when the growth time exceeds the characteristic RT time. The new size is proportional to the wavelength Λ_{RT} of the disturbances. Thus, C_{RT} determines both whether or not the droplets are going to be converted into smaller drops and how large the new droplets are going to be. The RT mode does not add any new parcels to the system, it only increases the statistical number of droplets in the parcel and changes the radii of the droplets.

3.2.6   Evaporation Model

When modelling the evaporation of a droplet, the key parameter is the lifetime, or evaporation relaxation time of the droplet. The derivation of this time starts by evaluating the time-derivate of the mass of the droplet.

$$\frac{dm_{\mathrm{d}}}{dt} = \rho_{\mathrm{d}}\frac{d}{dt}\left(\frac{4}{3}\pi\left(\frac{D}{2}\right)^3\right) = \frac{\rho_{\mathrm{d}}\pi}{2}D^2\frac{dD}{dt} \tag{3.34}$$

Further, the evaporation is assumed to follow the empirical D^2-law:

$$\frac{dD^2}{dt} = C_{\mathrm{e}} \Rightarrow \frac{dD}{dt} = \frac{C_{\mathrm{e}}}{2D} \tag{3.35}$$

where C_{e} is a constant. From this equation we can determine the relaxation time by integration (since C_{e} is a constant).

$$D^2 = C_{\mathrm{e}}t + D_{\mathrm{o}}^2 \tag{3.36}$$

If we want to determine the time (τ_{e}) when a droplet of size D_0 has completely evaporated, we can put $D = 0$ into the above equation, resulting in:

$$\tau_{\mathrm{e}} = -\frac{D_0^2}{C_{\mathrm{e}}} \tag{3.37}$$

The only unknown in this equation is the constant C_{e}, which will be determined by inserting equation 3.35 into equation 3.34, the result is:

$$\frac{dm_{\mathrm{d}}}{dt} = \frac{\rho_{\mathrm{d}}\pi}{4}DC_{\mathrm{e}} \tag{3.38}$$

However, the time derivative of the mass of the droplet can also be expressed as ([52]):

$$\frac{dm_{\mathrm{d}}}{dt} = -\pi D\mathrm{Sh}\mathcal{D}\rho_{\mathrm{v}}\ln\left(\frac{p - p_{\mathrm{v},\infty}}{p - p_{\mathrm{v,s}}}\right) =$$
$$= -\pi D\mathrm{Sh}\mathcal{D}\rho_{\mathrm{v}}\ln\left(1 + \frac{X_{\mathrm{v,s}} - X_{\mathrm{v},\infty}}{1 - X_{\mathrm{v,s}}}\right) \tag{3.39}$$

Using these two equations for $\frac{dm_{\mathrm{d}}}{dt}$, the value of the constant C_{e} can be expressed as:

$$C_{\mathrm{e}} = -4\mathrm{Sh}\frac{\rho_{\mathrm{v}}}{\rho_{\mathrm{d}}}\mathcal{D}\ln\left(1 + \frac{X_{\mathrm{v,s}} - X_{\mathrm{v},\infty}}{1 - X_{\mathrm{v,s}}}\right) \tag{3.40}$$

The Sherwood number Sh is calculated using the Ranz-Marshall (or Frössling) correlation (from [51]):

$$\mathrm{Sh} = 2 + 0.6\mathrm{Re}^{1/2}\mathrm{Sc}^{1/3} \tag{3.41}$$

Equation 3.37 can now be used with known C_e to solve equation 3.39:

$$\frac{dm_d}{dt} = -\frac{m_d}{\tau_e} \tag{3.42}$$

where the relaxation time is

$$\tau_e = \frac{\rho_d D^2}{6\mathcal{D}\mathrm{Sh}\rho_v \ln\left(1 + \frac{X_{v,s} - X_{v,\infty}}{1 - X_{v,s}}\right)} \tag{3.43}$$

and a similar equation for the diameter (from 3.35):

$$\frac{dD}{dt} = -\frac{D}{3\tau_e} \tag{3.44}$$

A relaxation time is introduced to characterise the evolution of the particle size. If an explicit method is used, the time step (a function of the relaxation timescale) must not be larger than the relaxation time, or the mass will become negative. If an implicit method is used, the method is unconditionally stable. It is also consistent with the way the momentum and heat transfer equations for each parcel are solved. The difference in timescales of these processes is useful for determining the rate at which each process is proceeding.

3.2.7   Heat Transfer

The heat transfer model comes in part from [51], and is based on the convective heat transfer of a particle with a uniform temperature. A modification was made to account for the latent heat phase transfer during evaporation. The heat transfer model also uses the evaporation relaxation time, since the evaporation of a droplet also transfers heat to the surrounding gas.

$$\frac{dT_d}{dt} = \frac{\pi D \kappa_c \mathrm{Nu}}{m_d c_l}(T_g - T_d)f_{\mathrm{heat}} - \frac{1}{c_l}\frac{h_v(T_d)}{\tau_e} \tag{3.45}$$

The modification is in the factor f_{heat} which is:

$$f_{\mathrm{heat}} = \frac{-\frac{c_{p,v}\dot{m}_d}{\pi D \kappa_c \mathrm{Nu}}}{\left(e^{-\frac{c_{p,v}\dot{m}}{\pi D \kappa_c \mathrm{Nu}}} - 1\right)} \tag{3.46}$$

The first part of equation 3.45 accounts for the heat transfer to the liquid, and the second part for latent heat arising from mass transfer. Since the mass transfer is related to the evaporation of the droplet, the relaxation time introduced in 3.2.6 is used. The heat transfer can also be expressed with a relaxation time:

$$\tau_{\mathrm{h}} = \frac{m_{\mathrm{d}}c_{\mathrm{l}}}{\pi D \kappa_{\mathrm{c}} \mathrm{Nu}} \tag{3.47}$$

resulting in:

$$\frac{dT_{\mathrm{d}}}{dt} = \frac{(T_{\mathrm{g}} - T_{\mathrm{d}})}{\tau_{\mathrm{h}}}f - \frac{1}{c_{\mathrm{l}}}\frac{h_{\mathrm{v}}(T_{\mathrm{d}})}{\tau_{\mathrm{e}}} \tag{3.48}$$

where one term describes heat transfer due to temperature difference, and the other heat transfer due to mass of the droplet lost through evaporation.

3.2.8 Particle Collisions

OpenFOAM offers two collision models: the O'Rourke model [68], and the modification by Nordin [52]. Other models have also been published, for instance the collision model by Schmidt *et al* [69], using adaptive collision meshing, which involves generating a separate orthogonal collision mesh with random orientation in every time step. The mesh is refined until the number of parcels in each cell is below a set threshold.

In the simulations presented in the included papers and the results chapter the trajectory collision model by Nordin [52] was used (unless otherwise stated). This is based on the O'Rourke collision model, which will be briefly described. Other modifications have also been made to the O'Rourke model [70]. In the original version, parcels collide if they are in the same cell with a probability given by:

$$e^{-\min(N_1,N_2)\frac{1}{4V_{\mathrm{cell}}}\pi(d_1+d_2)^2|U_1-U_2|\Delta t} \tag{3.49}$$

In practice, a random number between 0 and 1 is generated for each parcel. If the number is lower than the probability, the parcels are set to collide. The outcome of the collision depends on the Weber number, resulting in either coalescence or grazing. Thus, the direction of the parcels has no influence on whether they collide or not, nor does their position within the cell. If the cells are large, parcels several droplet radii away will be able to collide, although the probability of this will be lower, according to equation 3.49 (due to the large cell size). At the other extreme, there will be few collisions in very small cells, since parcels will not often occupy the same cell. In all, the O'Rourke model has very strong grid dependency, as shown in [52, 69].

As mentioned previously, the model implemented into OpenFOAM used for the work presented in the appended papers is a modified form of the O'Rourke model. Instead of only colliding parcels that are in the same cell, the algorithm calculates the paths of all parcels and collides those that will intersect within the same timestep. Thus the parcels need to be in the same position, regardless of the mesh. Since a simulated spray may contain several thousand parcels, the algorithm first calculates whether a pair of parcels is heading

towards each other. If they are not, they are regarded as not colliding. This
reduces the computational load of the algorithm, and is done by computing:

$$v_{\text{Align}} = \frac{(\mathbf{U}_1 - \mathbf{U}_2) \cdot (\mathbf{x}_2 - \mathbf{x}_1)}{|\mathbf{x}_2 - \mathbf{x}_1|} \tag{3.50}$$

This property will give how much of the vector $\mathbf{x}_2 - \mathbf{x}_1$ can be projected onto
the vector $\mathbf{U}_1 - \mathbf{U}_2$, if it is positive it indicates that the parcels are heading
towards one another, if it is negative they are travelling away from each other,
and if it is zero, they are on a perpendicular course. The parcels also need to
be close enough to collide since, as mentioned before, they need to reach each
other within the current timestep, this gives the next criterion:

$$|\mathbf{x}_2 - \mathbf{x}_1| - \frac{d_1 + d_2}{2} < v_{\text{Align}}\Delta t \tag{3.51}$$

On the left hand side of this equation is the distance between the droplet
surfaces, and on the right hand side the parcels' relative displacement during
the current timestep, which must be larger. This ensures that the parcels can
reach each other within the given time (the numerical timestep). The question
that remains to resolve is whether or not the parcels reach the intersection at
the same time. If, for instance, one parcel has a high velocity and the other a
low velocity, they may miss each other. So the algorithm needs to determine
the times (designated t_α and t_β) at which the parcels reach the intersection,
this is done by solving:

$$\mathbf{x}_{1,\text{new}} = \mathbf{x}_1 + t\mathbf{U}_1 \qquad \mathbf{x}_{2,\text{new}} = \mathbf{x}_2 + t\mathbf{U}_2 \tag{3.52}$$

$$\frac{\partial |\mathbf{x}_{2,\text{new}} - \mathbf{x}_{1,\text{new}}|}{\partial t_1}(t = t_\alpha) = 0 \quad \frac{\partial |\mathbf{x}_{2,\text{new}} - \mathbf{x}_{1,\text{new}}|}{\partial t_2}(t = t_\beta) = 0 \tag{3.53}$$

Whether the parcels actually collide or not is governed by chance, the
probability for a collision is now given by:

$$\mathcal{P}_{\text{coll}} = \left(\frac{\frac{1}{2}(d_1 + d_2)}{\max(\frac{1}{2}(d_1 + d_2), |\mathbf{x}_{1,\text{new}}(t_\alpha) - \mathbf{x}_{2,\text{new}}(t_\beta)|)} \right)^{C_{\text{space}}} e^{-\frac{c_{\text{time}}|t_\alpha - t_\beta|}{\Delta t}} \tag{3.54}$$

where $|\mathbf{x}_{1,\text{new}} - \mathbf{x}_{2,\text{new}}|$ is the smallest distance between the two parcels during
the timestep. As this value declines, the probability of collision increases. The
two model constants C_{time} and C_{space} control the collision rate in time and
space, respectively.

Chapter 4

Results & Discussion

4.1 Simulations of a Diesel Flow in a Cavitating Model Nozzle

Paper 2 describes simulations of the flow inside a model nozzle using a new code for cavitation implemented in OpenFOAM. The code, which was described in section 2.4, was unstable and obtaining the results in this section required extensive work. The simulations were run on a grid representing the experimental nozzle shown in figure 4.1. The inlet pressure was set to 10 MPa, and the outlet pressure was varied between 1.5 MPa and 5.1 MPa.
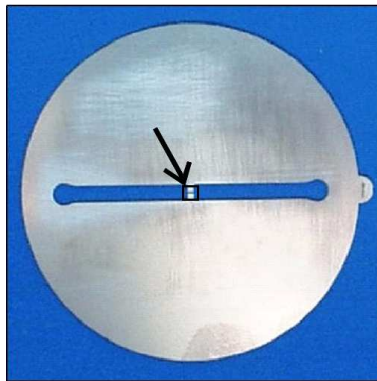
Figure 4.1: View of the experimental setup, the centre of the image contains the 1 mm model injector. Before and after the nozzle, there is a 1 cm wide channel.

The first converged results displayed a shock-wave zig-zag pattern developing through the channel. As the boundary conditions were set in a more appropriate way, and the geometry was improved by adding more cells before and after the channel, the following cavitation pattern was obtained:
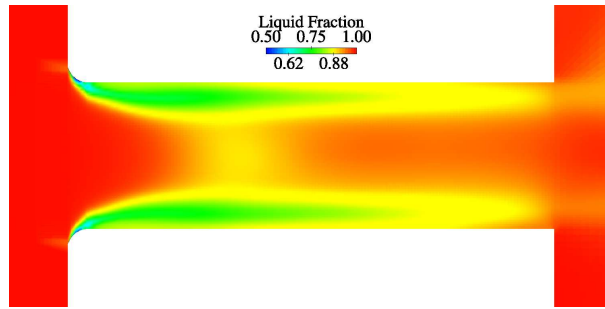
Figure 4.2: Image of the computed average vapour fraction, injection pressure 7 MPa

The pattern obtained, shown here for an injection pressure of 7 MPa, was very smooth. It should also be noted that this pattern has a scale ranging between 0.5 and 1 to allow the reader to distinguish between the two phases, as the case is barely cavitating. The cavitation bubble in this case was so stable, that calculating an average made hardly any difference. However, it did match pressure curves acquired experimentally [71]. After considering this image, a change of convection scheme was introduced. Instead of using the limited linear scheme, as done previously, the monotonized central scheme [72] was used. A routine was also implemented for calculating the cavitation probability, which the experimental data showed, instead of the mean vapour fraction as displayed in figure 4.2. Unfortunately, the change of scheme not only introduced instabilities in the wall cavitation bubble, it also produced four oblong cavitation bubbles in the centre of the domain (see figure 4.3) due to strong vortices.

These vortices could be removed by introducing a slip condition on the upper and lower walls. The physical rationale for the slip condition was that the boundary layer along the two walls is extremely thin, and a no-slip condition would cause the size of the layer to be overestimated, and thus produce sufficiently strong vortices to cavitate the fluid. After the slip condition was introduced, the results illustrated in figure 4.4 were obtained, which compare well to experimental results (figure 4.5). A comparison of the experimental mass flow rate and the calculated mass flow rate is also shown, in figure 4.6. It is very important for the code to be able to capture the maximum mass flow as the flow cavitates, since this is a fundamental property of nozzle flow.
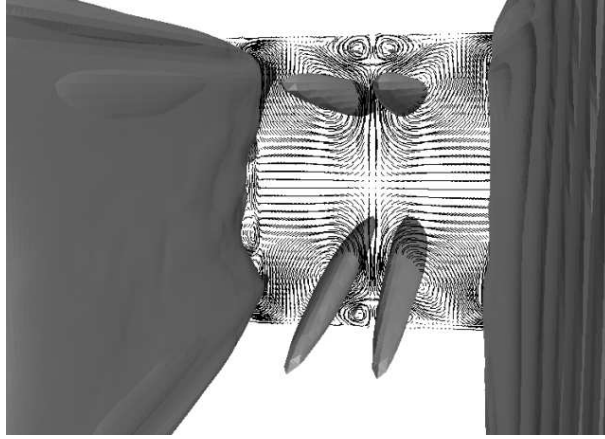
Figure 4.3: Mean isosurface for a vapour fraction of 0.1, velocity field in a plane perpendicular to the flow direction shown to visualize the vortices, with no-slip condition applied to both upper and lower walls. The image shown is taken as if the viewer is situated in the nozzle looking at the flow going downstream with the cavitation bubbles on the left and right sides.
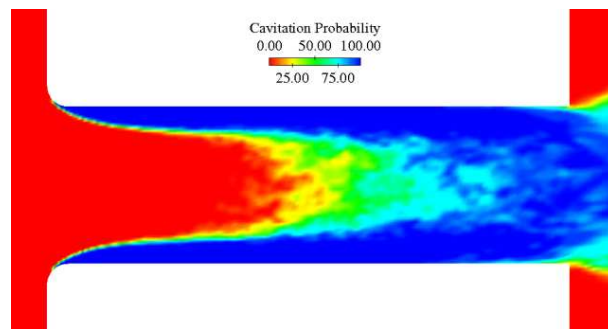

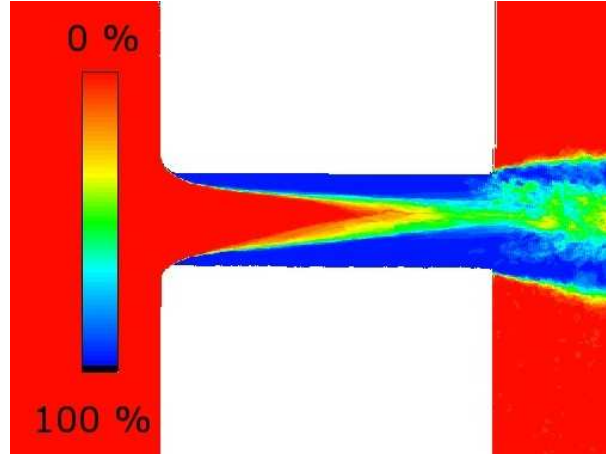Figure 4.4: Image of computed cavitation probabilities in the channel section of the model injector, injection pressure 8.5 MPa

Figure 4.5: Image of experimental determined cavitation probabilities, injection pressure 8.5 MPa
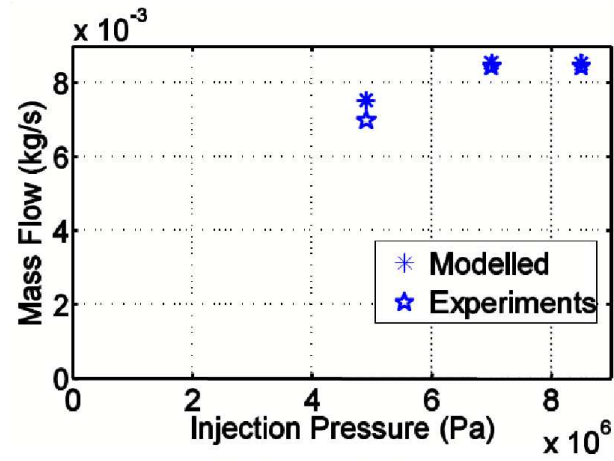
Figure 4.6: Modelled and experimentally determined mass flows with injection pressure of 4.9, 7 and 8.5 MPa

4.2 Injector Simulation Results

Results obtained using the cavitation single-phase code are presented in Paper 2. Since the liquid-vapour-gas code described in section 2.2 is not sufficiently stable to run for diesel conditions, it was not used in any of the published studies. However, an example of the kind of results generated using the code is shown in figure 4.7.
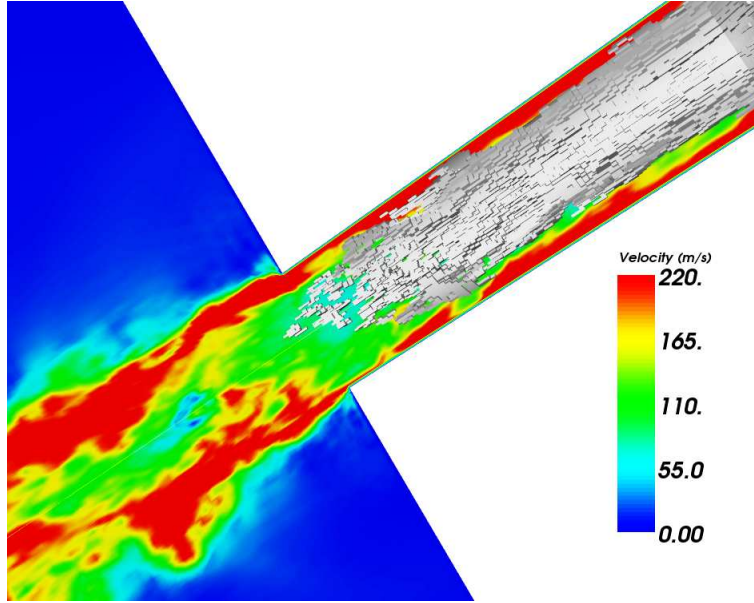
Figure 4.7: Cutplane of injector geometry, coloured according to velocity magnitude. Isosurface of $\rho = 500\text{kg/m}^3$

While the above simulation looks pretty, it requires a simulation time of over 200 days if run on a single processor (assuming perfect parallelization). The simulation was run on 12 processors, thus reducing the time to 17 days. It should also be noted that the mesh at 1.7 million cells is not sufficiently fine to resolve the in-cylinder spray structures, but may be adequate for modelling turbulence and cavitation inside the injector.

4.2.1 Impact of Injection Model

As stated in the model description section, one objective for this project was to develop a new injection model for Euler-Lagrangian diesel sprays. However, since the available code for simulating a cavitating fluid was not capable of handling high pressures, no such model could be developed. Remaining of the efforts to develop an injection model is the presented code for cavitation and a preliminary study which was made to answer questions like: How much influence does the injector model have? Will the fuel-distribution/flame be influenced by variations in the spray angle or droplet distribution and, if so, how much? These questions were briefly addressed using simulations with several different spray angles and droplet distributions. This was by no means a full study, and the conclusions are tentative at best.

The numerical grid and physical data were the same as those used in Paper 3, except that combustion was switched off for these simulations. Results of varying the injection spray angle are shown in figure 4.8. There is a slight change for the liquid phase, but the gas phase remains almost unchanged for a doubled injection cone angle.

(a) 9 degrees injection cone angle (b) 20 degrees injection cone angle
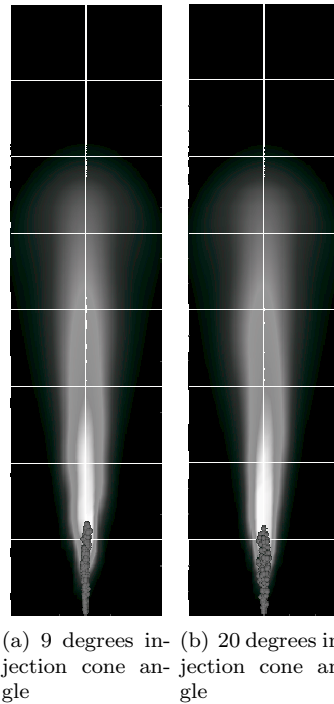
Figure 4.8: Comparison of fuel vapour distribution in a centre cutplane for a low injection angle (9 degrees) and a large angle (20 degrees)

Another initial parameter for the spray is the initial droplet size. This parameter was also varied, by varying the Rosin-Rammler distribution (as described in section 3.2.3) used. As shown by the images in figure 4.9, initial parameters of the droplets also have quite a minor influence on the vapour distribution. They seem to affect the penetration of the fuel vapour core, but not the overall vapour penetration. However, they strongly influence the liquid penetration, which will have substantial effects on combustion.

(a) $d_{\text{av.}} = 50$ μm (b) $d_{\text{av.}} = 100$ μm (c) $d_{\text{av.}} = 200$ μm
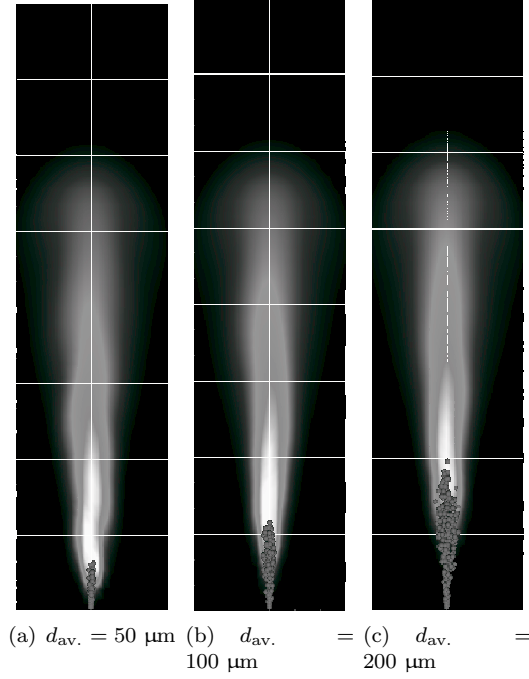
Figure 4.9: Comparison of fuel vapour distributions in a centre cutplane obtained with three average initial diameter values

4.3   Spray Results without Chemistry

In Paper 1, results of applying the turbulence length-scale limiter (described in section 3.1.3) are presented. Due to the constraints on the length of the article, the effects of the modification on vapour penetrations on 2 and 3 dimensional grids were mainly used to demonstrate the improvements it provided. However, the effect of the length scale limiter on liquid penetrations is also beneficial in terms of promoting grid independence, as will be shown in this section. For details on grids, physical conditions etc., see Paper 1.

4.3.1   Grid Dependency

This section deals solely with the grid dependency of the simulations conducted in 2D to show how the limiter decreases the dependency. The liquid penetration obtained using the standard k-ε model is shown in figure 4.10
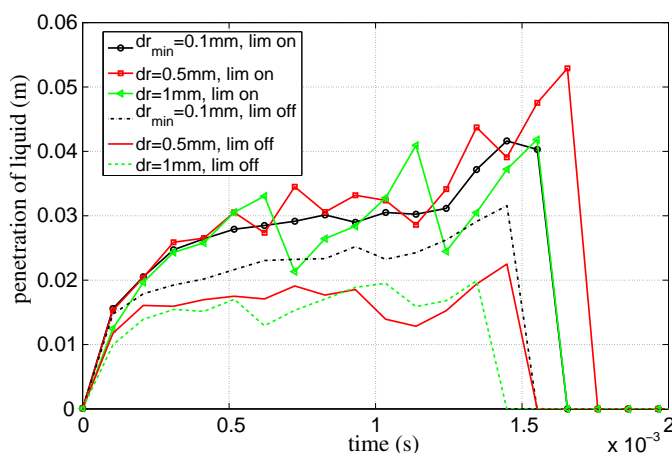
Figure 4.10: Liquid penetration vs. time, obtained using three different grids, standard k-ε

When using the length-scale limiter the calculations seem to exhibit grid independency, while the calculations without the length-scale limiter produce different shapes on the three grids. It can also be seen that increasing the cell size results in more significant deviations from the average. If we filter out the oscillations, using a simple local filter, we can see the local average at each point. This gives an idea of the average penetration for every timestep sampled. The results can be seen in figure 4.11.

The large oscillations observed in the liquid penetration rate are due to the liquid penetration being set to the furthest point reached by 95% of the liquid mass in the system. If this was set to a lower value, for example 90%, the results would be less oscillatory and possibly no filtering would be needed.
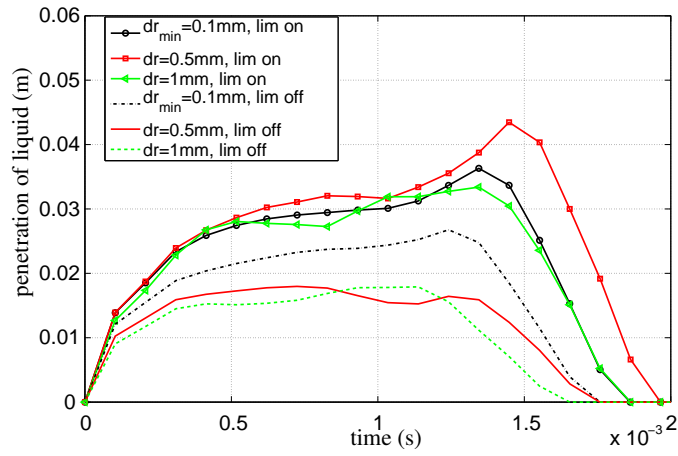
Figure 4.11: Liquid penetration vs. time, obtained using three different grids, the standard k-ε model and filtered penetrations

When the Launder-Sharma k-ε model is used, the behaviour is slightly different, see figure 4.12. The penetration obtained with the coarsest grid differs considerably from those obtained with the two finer ones, indicating that 3000 cells with a cell size of 1 mm may be too coarse. In Paper 1 similar indications were shown for the vapour penetration. However, the penetration across the three different grids is more uniform with the limiter then without it.
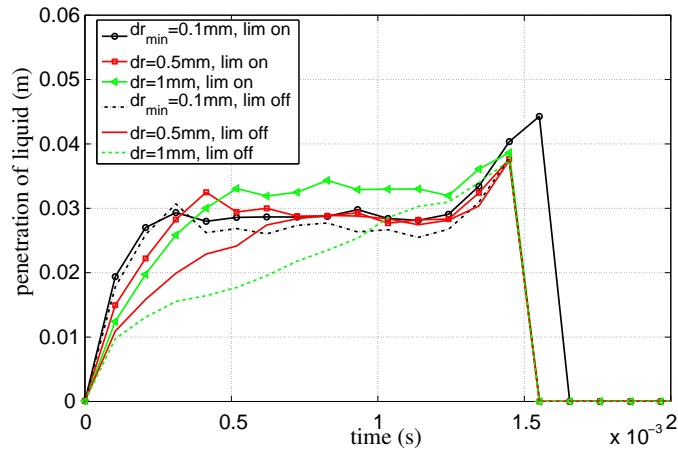
Figure 4.12: Liquid penetration vs. time, obtained using three different grids and the Launder Sharma k-ε with no filter

4.3.2   Time Step Dependency

The code uses a Courant-based timestep, which means the timestep changes
with the grid size and local velocity. This implies that one cannot draw
conclusions about grid independency, without also investigating the effects of
different Courant numbers. The results of a Courant number investigation are
shown in Figures 4.13 & 4.14. The limiter has a positive effect on the liquid
penetration, but not as strong as its effects on the vapour penetration, for
which it removed the dependency completely (Figures 4.15 & 4.16, taken from
Paper 1).
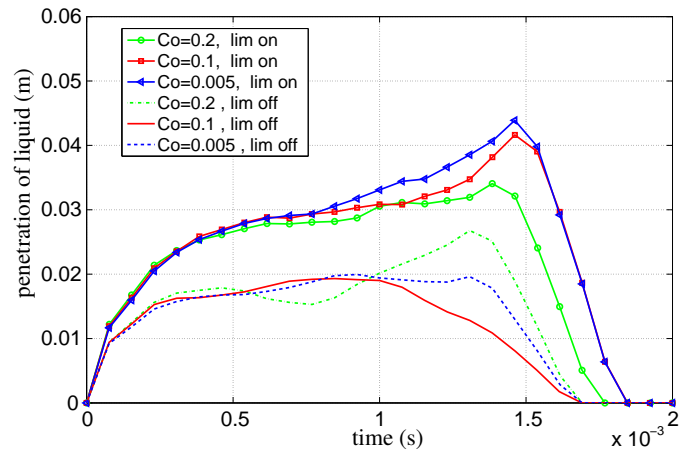
Figure 4.13: Liquid penetration vs. time, obtained using three different Courant
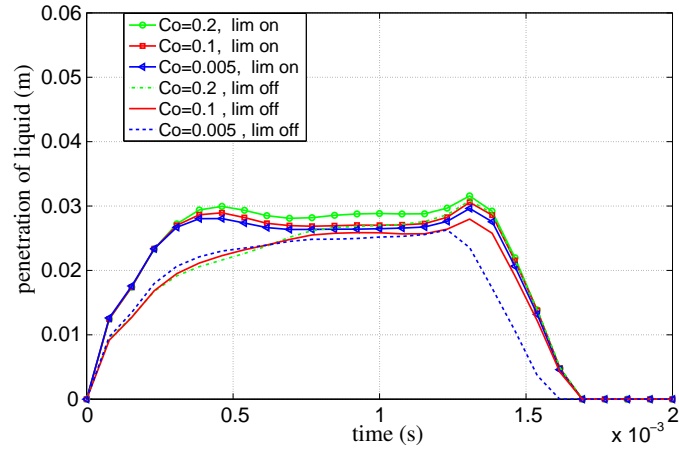numbers and the k-ε model with filtering used

Figure 4.14: Liquid penetration vs. time, obtained using three different Courant
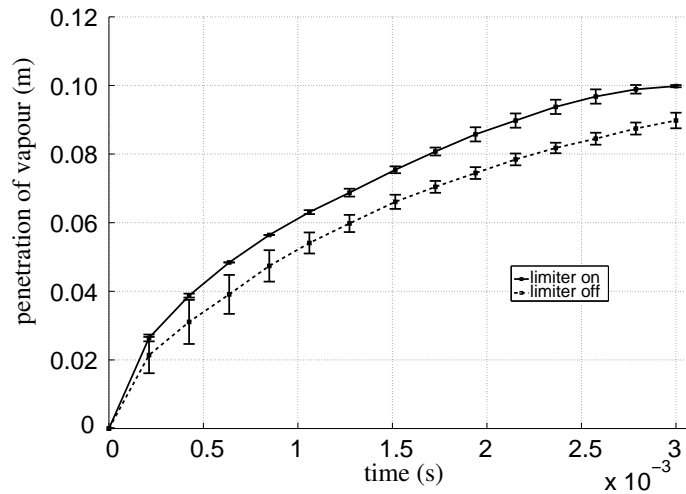numbers, the Launder Sharma k-ε model and filtering used

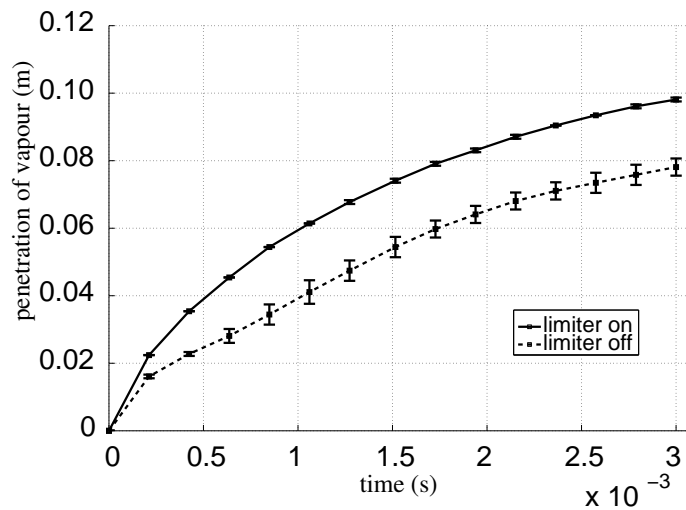Figure 4.15: Vapour penetration vs. time, obtained using three different Courant numbers and the standard k-ε model

Figure 4.16: Vapour penetration vs. time, obtained using three different Courant numbers, and the Launder-Sharma k-ε model

4.3.3   Comparison to Experimental Data

To compare simulations using the turbulence length scale limiter to experiments, an extensive range of injection and bomb pressures were used. The results of that study was presented in Paper 1, and only one case will be presented here for reference.
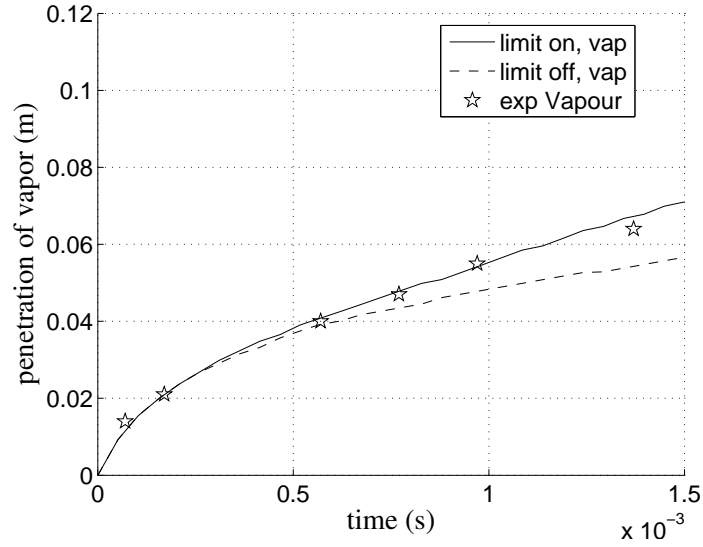

Figure 4.17: Vapour penetration vs. time for a 3D case comparing experimental to simulated data. Injection pressure, 70 MPa; bomb pressure, 4.4 MPa.

4.4   Influence of Numerical Scheme

In numerical simulations of diesel sprays, using a grid with more, smaller cells does not necessarily increase the accuracy of the simulations. Instead, the best grid for a specific case is found on an empirical basis. As shown in Paper 4, the same is true for the numerical scheme, and to some degree, the initial conditions for the turbulence. The numerical scheme referred to here is the scheme for the advection term (for a more detailed description of how the scheme is used when solving the momentum equations, see Appendix A.2). The numerical schemes examined in Paper 4 were members of the total variation diminishing (TVD) family of schemes, which were initially developed to handle large gradients, originally in compressible high Mach number flows. However, they can also be applied with success to other cases, such as diesel sprays where there are high gradients between the spray and the surrounding quiescent air.
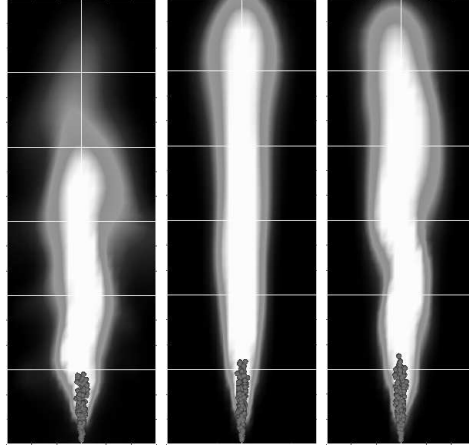

Figure 4.18: Fuel vapour distributions of three sprays, obtained using linear interpolation (left), upwind interpolation (centre) and MC interpolation (right). Grey scale altered (compared to the one in figure 4.19) to ensure that the fuel distribution is visible for all cases. The Launder-Sharma k-ε model was used for modelling turbulence. Time, 1 ms after SOI. Initial $\mu_T = 10^{-5}$ m^2/s.

As can be seen, the differences in vapour distribution obtained using different numerical schemes are quite large. Since MC interpolation uses both upwind and linear interpolation, it mixes the properties of the two solutions using the simpler schemes. MC yields as long penetration as upwind, while retaining some irregularities like linear interpolation. The difference between the schemes was found to be larger when a lower turbulence viscosity was set, indicating that a high viscosity smoothes the solution to such a degree that no instabilities or high gradients are present (see Figure 4.19). This is also, in a sense, an illustration of how the TVD limiter works. When there are no gradients, the TVD limiter will revert to a linear scheme, and the choice of TVD limiter will not have an effect on the solution.
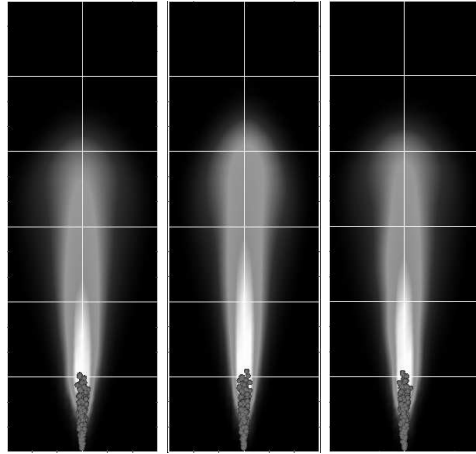
Figure 4.19: Fuel vapour distributions of three sprays, obtained using linear interpolation (left), upwind interpolation (centre) and MC interpolation (right). The Launder-Sharma k-ε model was used for modelling turbulence. Time, 1 ms after SOI. Initial $\mu_T = 3.6 \cdot 10^{-4}$ m^2/s.

4.5   Fuel Sprays with Chemistry

In Paper 3, simulations of events in the Sandia [73] constant-volume-vessel were presented. The focus was on differences between KIVA-3V and OpenFOAM predictions of ignition delay time and flame lift-off length, and how well the codes could calculate these parameters compared to experimental data. The simulations were performed on a cubic mesh with 108 mm sides for the following conditions: ambient gas oxygen concentrations, 8-21 %; ambient gas temperatures, 750-1300 K; and ambient gas density, 14.8 kg/m^3. The injector orifice diameter was 100 μm, and the injection pressure difference was set to 1500 bar.

As can be seen from figures 4.20 through 4.23, OpenFOAM can predict the ignition delay time and its dependence on ambient temperature and ambient oxygen concentration fairly well. This indicates of that the initial evaporation and chemical kinetics are "correct". Unfortunately, the flame lift-off length predictions are not as good. OpenFOAM seems to overpredict the changes in lift-off length caused by variations oxygen concentrations and ambient temperature. KIVA-3V calculations use a set atomization length, as can be seen from figure 4.20, where the lift-off length is stable above 1100 K. OpenFOAM's lift-off length is also stable for these temperatures, but this is because the flame cannot be any closer to the wall (due to the constant temperature condition set along the walls).

The time sequence in figure 4.24 displays how the ignition starts and flame propagates in OpenFOAM, KIVA-3V and experiments. The flame in OpenFOAM and KIVA-3V differs in two main respects. In OpenFOAM (and the experiments) the flame ignites and then propagates upstream towards the injector, whereas in KIVA-3V the flame ignites closer to the injector and then the flame lift-off length propagates downstream. The second main difference is that OpenFOAM's flame is very long and thin compared to KIVA-3V's wider, shorter flame. The long flame generated by OpenFOAM penetrates much too far, according to the experimental data. In the simulations Paper 4 is based upon, this was found to be due to the numerical scheme and turbulence model chosen. RNG k-ε is the k-ε turbulence model in OpenFOAM that produces the longest flames, and the limited linear scheme in OpenFOAM was found to promote long, thin flames and fuel distributions. These results, and the quantitative results in figures 4.20-4.23 are extracted from Paper 3.

The computational time was much higher in OpenFOAM compared to KIVA-3V. The case with 21% oxygen took up to 70 hours on 4 processors using OpenFOAM, about 4 times the computational time for KIVA-3V. The main reason for the high computational time is solving the chemical reaction rate equations. In OpenFOAM they are solved fully coupled using the SIBS ODE solver as described in section 3.1.4. If the ODE solver for the chemistry can be optimized to reduce the computational time without losing accuracy is an object for future work.

In addition to the two codes differing in computational time, there are numerous other differences in the solver in two codes. OpenFOAM uses a

collocated grid arrangement, whereas KIVA-3V uses a segregated grid
arrangement. OpenFOAM uses spray submodels which are the same by name,
but the way they are implemented in KIVA-3V is different. The spray
momentum coupling, chemical solver, and turbulence model are also different.
These differences do not make the comparisons presented here and in Paper 3
irrelevant, since it was made to compare the two codes in terms of
performance and ability to match experimental data. A full comparison of the
two codes should be made starting with simulation of a simple model flow,
where complexity such as compressibility, spray, spray submodels, chemistry
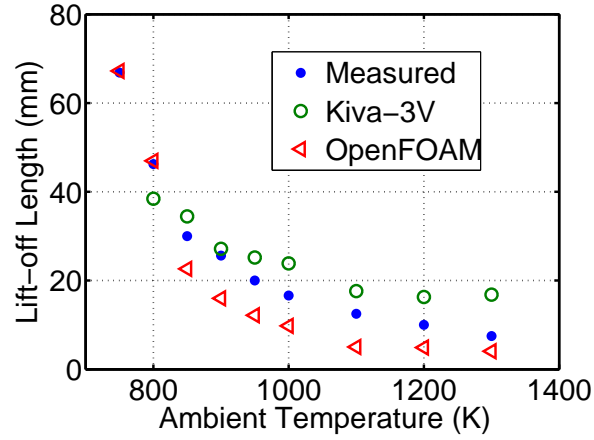etc. is added step-by-step to see the effects of each model.

Figure 4.20: Comparison of OpenFOAM and KIVA-3V-predicted and measured
lift-off lengths for different ambient gas temperatures, at ambient gas oxygen
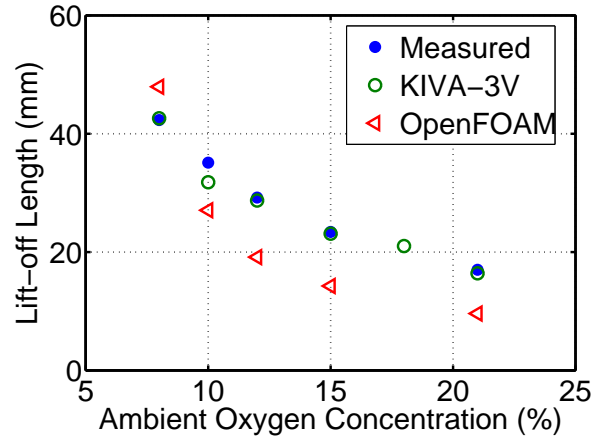concentration and density of 21% and 14.8 kg/m^3, respectively.

Figure 4.21: Comparison of OpenFOAM and KIVA-3V-predicted and measured
lift-off lengths for different ambient gas oxygen concentrations at an ambient
gas temperature and density of 1000 K and 14.8 kg/m^3, respectively.

Figure 4.22: Comparison of OpenFOAM-predicted and measured ignition delay times for different ambient gas oxygen concentrations at an ambient gas temperature and density of 1000 K and 14.8 kg/m^3, respectively.
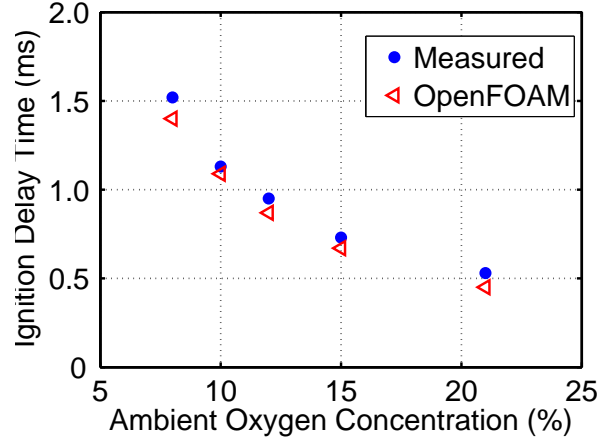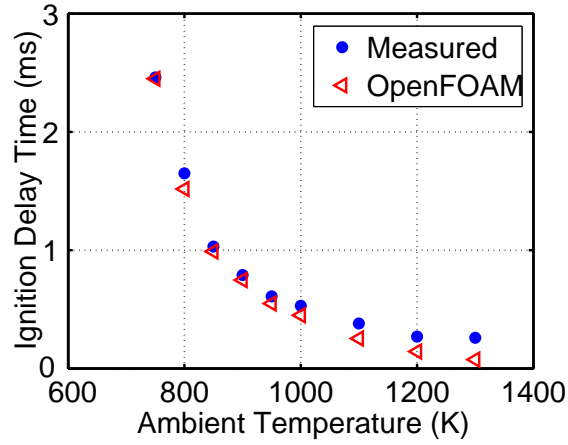

Figure 4.23: Comparison of OpenFOAM-predicted and measured ignition delay times for different ambient gas temperatures at an ambient gas oxygen concentration and density of 21% and 14.8 kg/m^3, respectively.

Temperature (K)

750   1210   1675   2140   2600

PSfrag replacements
Temperature

PSfrag replacements   PSfrag replacements
Temperature   Temperature

PSfrag replacements   PSfrag replacements
Temperature   Temperature

PSfrag replacements 0.5 ASI   PSfrag replacements 0.8 ASI
Temperature   [160]   Temperature   [1.0]

              t = 0.5 ms   t = 0.8 ms

PSfrag replacements   PSfrag replacements
Temperature   Temperature

PSfrag replacements   PSfrag replacements
Temperature   Temperature

PSfrag replacements 1.1 ASI   PSfrag replacements 1.3 ASI
Temperature   [1.0]   Temperature   [0.7]

              t = 1.1 ms   t = 1.3 ms

PSfrag replacements
Temperature

PSfrag replacements
Temperature

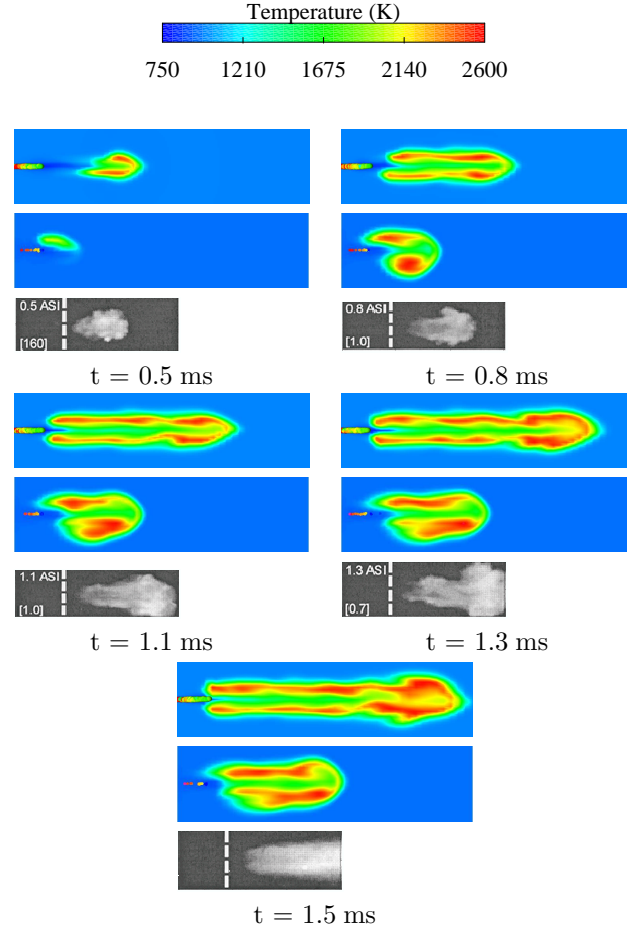PSfrag replacements
Temperature

              t = 1.5 ms

Figure 4.24: Time sequences of simulated temperature distributions obtained
using the OpenFOAM code (top) and KIVA-3V code (middle) showing igni-
tion and flame development of an n-heptane spray in the Sandia high-pressure,
high-temperature vessel: ambient oxygen concentration, 21 %; ambient temper-
ature, 1000 K; and ambient density 14.8 kg/m^3. Corresponding, experimentally
acquired OH chemiluminescence images are shown in the bottom part of each
subfigure. The length of each image from simulations corresponds to 108 mm,
the experimental images are of the same scale, but extending 60 mm.

4.5.1 Combustion Predictions Using Other Schemes

In Paper 3, the limited linear scheme was used for the advection term, and the RNG k-ε model for turbulence. As mentioned in the previous section, these two choices were quite unfavourable for obtaining similar (short) flames to those observed in experiments. They did, however, provide reasonably close flame lift-off lengths (which was the reason for the choices). The "best"[1] choices for advection scheme and turbulence (of those tested in the studies presented in Paper 4) were found to be Superbee and Launder-Sharma k-ε, respectively. It was also found that the initial turbulent viscosity should be slightly higher. These numerical conditions were used to examine whether good comparisons with data in the Sandia database of experiments could be maintained when combustion was considered in the simulation.
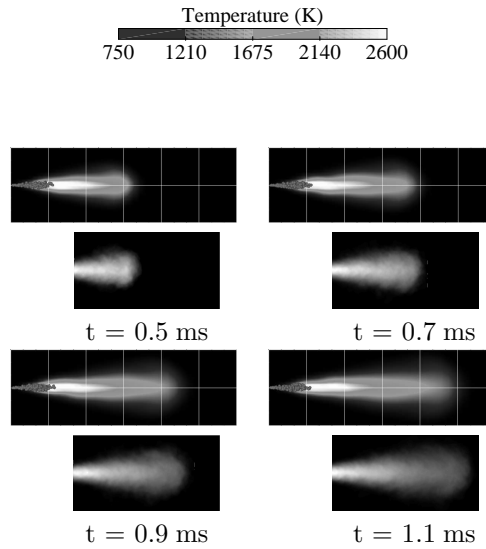

Figure 4.25: Comparison of fuel distributions obtained from experiments and simulations tuned to match the experimentally determined fuel vapour distribution for the non-combusting case. Ambient gas temperature, 1000 K; oxygen content, 0%; density, 14.8 kg/m^3.

Comparing Figure 4.25 and 4.26, showing images obtained from simulations excluding combustion and including combustion, respectively, it can be clearly seen that while OpenFOAM predicts the vapour distribution in the displayed part of the vessel accurately, it does not predict the combustion and (more specifically) the flame lift-off length so well. Aside from the well-predicted vapour distribution, the chemical mechanism used has been validated against shock tube data. These two validations reduce the number of possible reasons for the discrepancy in the flame lift-off length. Unfortunately, however, the

---

[1]In terms of matching experimental fuel vapour distribution of a non-combusting spray.
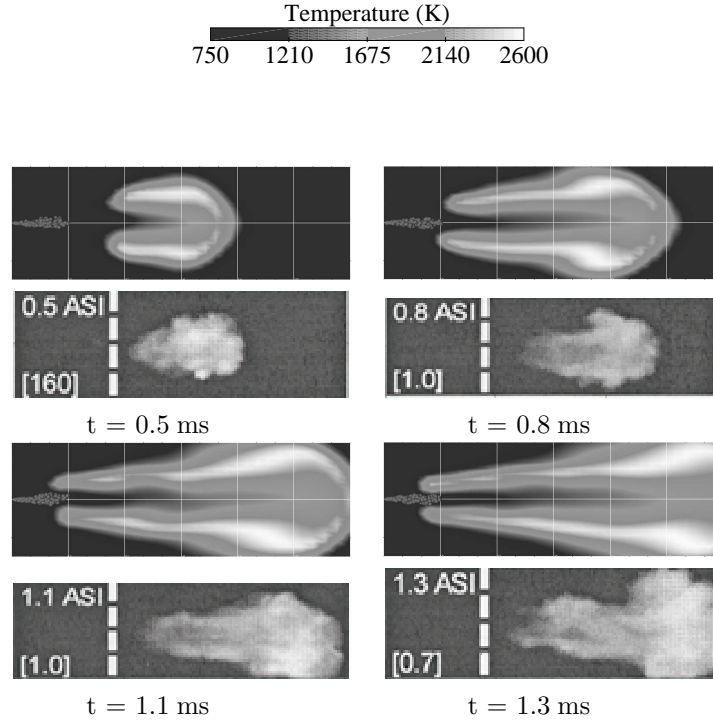
Figure 4.26: Comparison of OH chemiluminescence images obtained from experiments and temperature distributions from simulations tuned to match experimental fuel vapour distribution for a non-combusting case. Ambient gas temperature, 1000 K; oxygen content, 21%; density, 14.8 kg/m^3.

experimental data for the non-combusting case only covers the area 17 mm downstream of the nozzle and beyond. Hence, the data for the ignition site and early atomization zone cannot be validated. There are several possible remaining reasons for the difference between the experimental and simulated data; one is that the effects of air entrainment and air-fuel mixing might not be correct, i.e. the PaSR model might need improvement or the parameters used in it might be incorrect (most likely the turbulence mixing time). If our chemistry-turbulence model predicts perfect mixing in a position where it does not occur, the flame lift-off length could be underpredicted. This should also result in underprediction of ignition delay times, which is consistent with observations. OpenFOAM, like most other codes, assumes a Lewis number of unity for species diffusion, and this according to Hilbert *et al* [74] (page 94, figure 17 in [75]), can lead to substantially larger errors than use of more detailed approximations. Another set of unknowns that have already been mentioned in part are the liquid atomization parameters, including the liquid droplet distribution parameters, the penetration of the droplets before they evaporate, and the initial shape/particle distribution of the fuel cloud. A good

parameter to use for comparison would be the fuel lift-off length for a non-combusting case. The liquid penetration for the non-combusting case is reasonably well predicted by the simulations, but there is no way to verify how well it is predicted for the combusting case with currently available experimental data.

Finally, it is possible that the temperature dependence may be incorrect in some of the models. Unfortunately, data for only one non-combusting case were available at the time of these simulations, so it was not possible to verify that the vapour distribution or liquid length is correct at other temperatures and densities.

4.6 Comment on the PaSR Model

During the course of the work reported in Paper 3, it was observed that the PaSR model only had minor effects on the solution. The model was described in detail in section 3.1.4, but some of its properties will be repeated here for the reader's convenience. The parameter that will be highlighted in the figure below is κ, which determines the combusting and quiescent proportions of a cell, which depend in turn on local chemical and turbulent timescales. The chemical timescale is determined by the timescales of each reaction and does not contain any "tuning" constants. The timescale of the turbulence is different, and the way it should be calculated is an open question. In [54] the mixing timescale was calculated as:

$$\tau_{\text{mix}} = \left(\frac{1}{\text{Re}_T}\right)^{1/4} \frac{k}{\varepsilon} = 0.178 \frac{k}{\varepsilon} \qquad (4.1)$$

Other versions are from [59], in which the kolmogorov timescale is used, and [52] in which a modelling constant C_{mix} is used:

$$\tau_{\text{mix}} = C_{\text{mix}} \frac{k}{\varepsilon} \qquad (4.2)$$

This is the expression used in this work. In [52] the value of C_{mix} was reported to be 0.005, while the one I used for combustion calculations was 0.03. It was found that the simulations are almost independent of the value of C_{mix}, as long as it remains lower than 1 (in fact, major differences have not been observed until the value reaches 1000). For the n-heptane mechanism used in this work, the chemical timescale is thus always several times larger than the turbulent timescale. Naturally, the values of k and ε also affect the result, but for spray simulations ε has an average of the order of 10^6 m^2/s^3, while k is of the order of 100 m^2/s^3. An image of the values of κ in a combusting spray is shown in figure 4.27. The elevation is by temperature, to visualize the extent of the spray. The scale should be noted, since it ranges between 0.97 and 1.0. Obviously, the partially stirred reactor becomes a perfectly stirred reactor in

this case. However, whether or not this is due to unrealistic chemical timescales of the reactions involved, is not known at this time.
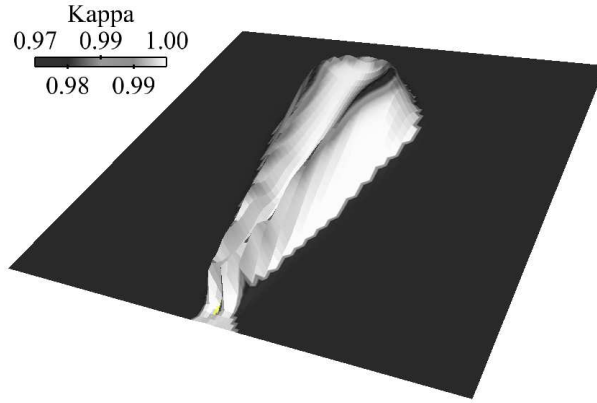

Figure 4.27: Display of a spray simulation (corresponding to the one shown in figure 4.26), coloured according to κ and elevated according to temperature. κ is the mass fraction of the cell that is involved in the chemical reactions. The area outside of the elevated temperature area has a κ value of zero.

Chapter 5

Conclusions

A code describing how a fluid cavitates when it is subjected to low pressures due to geometric contraction was successfully used to simulate data acquired from model nozzle experiments performed at AVL. The thesis shows that there are many pitfalls on the way to simulations that provide good comparisons to experimental events, as well as presenting some final results from the study. Examples of the degree of influence the injection model can have over the Euler-Lagrangian spray simulations are also presented, together with an example of results obtained using the three-phase code (mainly for illustrative purposes since this code has not been validated). These simulations were, as stated in the outline of the thesis (section 1.4), intended to be used for the development of an injection/atomization model for Euler-Lagrangian diesel spray simulations. Unfortunately, due to the high complexity of the problem, no such model could be developed. For a more detailed description of the encountered problems when simulating cavitating diesel injections, see section 4.1.

Regarding spray grid and time-step independence, the results from Paper 1 and section 4.3 clearly show that dependence diminishes when a limiter on the length scale of the turbulence is applied. The importance of this result cannot be over-emphasised, since shorter computational time means more investigations can be made, or results can be obtained in a shorter time. In short, it improves the efficiency of the CFD modelling.

The results also show how flame lift-off length and ignition delay time can be predicted by OpenFOAM, and the effects of varying the ambient oxygen concentrations and temperatures on these parameters. OpenFOAM was found to perform well when predicting the propagation of the flame compared to the ignition site, and in ignition delay time. However, it was found to underpredict the flame lift-off length and its dependency on temperature and ambient oxygen concentration. For a non-combusting case in the same geometry, OpenFOAM could predict the vapour distribution very well, in addition to the liquid and vapour penetration lengths.

To further analyze the reason for the short flame lift-off lengths yielded by OpenFOAM, the calculations and results of Siebers *et al* [76] were used. The cited report describes a way to estimate the percentage of stoichiometric air entrained (ξ) upstream of the lift-off length. According to this estimate, the percentage of entrained air is 29% of the air required for stoichiometric combustion, which is consistent with the article's relationship between injection velocity and ξ. Furthermore, according to the report, the liquid droplets and flame should be separated in distance much more from the injector than they are in figure 4.26. If the turbulence/chemistry interaction model used required more air to be entrained before combustion, the flame lift-off length might be increased without increasing the length of the flame. As indicated in section 4.6, the PaSR model does not suffice for this task.

The choice of scheme can have a large influence on the fuel vapour distribution, and thus on the resulting flame and combustion. This was demonstrated in paper 4, and also in sections 4.4 and 4.5.1. These effects are important to be aware of, in addition to the effects of numerical grid and turbulence model. In the work this thesis was based upon, the SuperBee TVD limiter was found to give the best results compared to experiments, but this finding could be (like the choice of grid) problem-dependent.

Chapter 6

Future Work

As shown in this thesis, diesel spray simulations using the Euler-Lagrangian approach are helpful, but they are not yet predictive. Therefore, much work needs to be done to improve them. Briefly, two possible approaches could be adopted in attempts to improve diesel spray simulations: Euler-Euler type simulations, which have only been used for primary breakup studies to date; or more sophisticated Euler-Lagrangian descriptions. Following the second approach, implies use of LES to model gas phase turbulence and better sub-models for the liquid-gas interactions. Another option is the VSB2 spray model developed by Karlsson [77], in which the Lagrangian parcels/blobs do not interact with the grid directly, but through bubbles of varying size. Furthermore, the Lagrangian parcels contain a distribution of blobs instead of equally sized droplets. Details of this setup are not known at this time, but might be published in the future.

In the nearer future, possible areas of future work are to continue efforts started in the studies published in Papers 3 and 4. As shown in the Results section, while the models presented in Paper 4 delivered fuel vapour distributions that approximated well to experimentally observed distributions, the resulting flames were not well predicted when chemistry was considered. Since we can now assume that the spray and vapour distributions are well tuned, the parts of the code that are largely responsible for the errors must be the turbulence/chemistry interaction (PaSR model), temperature dependency of the liquid penetration, primary breakup and initial vapour cloud formation, or the chemical mechanism itself. However, the chemical mechanism has been verified against shock-tube experiments, and seems to produce good comparisons for those cases. A way to rule out temperature dependency would be to run simulations and compare them to the results of corresponding experiments, without oxygen using different ambient temperatures. The validation presented in Paper 3 is only against one case, due to a lack of data from non-combusting experiments with well-defined boundary conditions to compare to the simulations.

When the results presented in Paper 3 are to be improved (beyond the improvement presented in this thesis), a large number of simulations where the chemical reactions are considered will have to be run. It would then be desirable to have optimized the solver for the chemical mechanism, as the computational time occupied by the solver in OpenFOAM is currently very high (as mentioned in section 4.5).

It would also be interesting to venture further down the path taken in Paper 2, investigating in detail how the initial droplet parameters influence the spray and combustion. The most important of these parameters, based on the short preliminary study, seems to be the initial droplet size distribution. It is likely that a good atomization and injection model would improve the flame lift-off length predictions presented in Paper 3, since the liquid penetration length has a strong influence on the ignition point and its propagation. These two approaches are linked in the sense that they both are concerned with the primary events of spray development. Simulating cavitating diesel flow requires a more robust model than the one used in Paper 2, and perhaps it is not even essential to the development of a new injection model. There are studies ([78, 79]) which links injection pressure, nozzle diameter, to spray angle, discharge coefficient etc. If these studies were used like the cavitation simulations were intended to be used, a diesel injection model could be developed based on experimental studies instead of numerical simulations.

Other aspects not covered in the thesis could be of interest for future work. One such aspect is the obvious extension from constant volume vessel simulations to engine simulations. OpenFOAM has the functionality to handle moving meshes with valves and other topological changes [80], so using the work described in Papers 3 and 4 as a basis for engine simulations to explore the effects of key variables in engines could be of high value to both the engine community and the numerical community.

Aside from using k-ε models and LES it could also be useful to assess the possible utility of other turbulence models such as k-ω type models, unsteady RANS models or other hybrid type turbulence models. It is possible that the turbulence plays a major role in obtaining correct air entrainment for modelling the early spray development and flame lift-off lengths.

6.1   Outlook

As mentioned above, it would be helpful to have access to an experimental database covering a larger array of non-combusting cases than the single case from Sandia. It would also be beneficial for research in numerical methods to have more data on the initial breakup of sprays for both combusting and non-combusting cases. A good example of a study that presented relevant data, in this respect, is one by Ochoterena *et al* [81], in which both liquid and vapour penetration lengths are presented along with flame lift-off lengths, cone angles and flame temperatures. Unfortunately, from a modeller's perspective, the fuels used are not as easy to model as, for instance, n-heptane, and the experiments were only run in combusting conditions. However, it should be

noted that supplying modellers with input for simulations was not one of the stated objectives of the cited study ([81]).

In light of the increasing need for more experimental data specifically tailored for validating numerical simulations, the author belives and strongly recommends that more experiments tailored for numerical simulations should be performed. Close, long-term co-operation between a modeller and an empirical investigator with access to both spray chamber and engine equipment would have every chance of making major advances in spray modelling. Furthermore, the need for good spray modelling will probably increase as engine concepts become more advanced and new fuels are introduced, to help ensure that demands from customers and legislation are met.

Finally, we return to the starting point of the thesis; horses in early 20th century America. During this period, commuters were facing rising prices for hay and oats, as well as increased public fears about pollution and traffic jams [1]. This situation is uncomfortably similar to current circumstances. Hopefully, the solution we devise this time will not lead to the same problems 100 years from now.

Chapter 7

Summary of Papers

The thesis is based on the work published in the following papers

Paper I - Numerical Investigation of Mesh/Turbulence/Spray Interaction for Diesel Applications

This paper originated from attempts to solve the problem of grid dependence described in section 1.4. The solution was based on a suggestion in the book "Modeling Engine Spray and Combustion Processes" by Gunnar Stiesch [12], p.183, that the turbulence length scale should be limited to the jet diameter within the jet region. The rationale for this is that the jet is the driving force for the turbulence in spray simulations. This was implemented in the OpenFOAM code, and tested on different sized grids in 2D and 3D, as well as using different time-steps. It was shown in the article that the length scale limiter was very beneficial in terms of reducing grid and time-step dependency. The results were also compared to data acquired in experiments performed at Chalmers on fuel injection into a high-pressure, high-temperature constant volume vessel. The multi-component model diesel fuel IDEA was used as the fuel. The simulations using the turbulence length scale limiter proved to provide better matches to the experimental data than when it was turned off. The most important finding was that the grid and time step dependency could be reduced by introducing the length scale limiter.

The simulations and paper were planned together with Dr Niklas Nordin, who also implemented the limiter in the code. I was responsible for the preliminary studies that were not included in the paper, to determine limiter size, grid optimization etc. I was also responsible for running and post-processing all but one of the simulations included in the paper, the remaining one was performed by Dr Niklas Nordin. The experimental data used were acquired by Alf-Hugo Magnusson at Chalmers University of Technology. The paper was written by

me, together with Dr Niklas Nordin, and I presented it at the SAE Fuel and
Lubricants Conference, 2005, in Rio de Janeiro, Brazil.

Paper II - Modelling Injector Flow Including Cavitation Effects for Diesel Applications

This paper was preceded by several attempts to model diesel injector flow.
The initial intention was to develop and present a new injection model,
together with validation of the code for the injector flow, in the same article.
However, simulating injector flow proved to be much more complex than
anticipated, so a decision was taken to focus solely on the validation in this
paper, while the injector model would be the topic of a possible later paper.
The code used in this paper was written by OpenCFD Ltd., as a by-product of
a code to simulate diesel injector flow with the ambient air as well as
cavitating diesel liquid.

I setup, ran and post-processed the simulations, with numerical help from
Henry Weller, who developed the code used. However, as these simulations
required extensive testing, I ran months of simulations, with various numerical
setups to ensure a stable solution, before the article was written. The
empirical data used for comparison were acquired from experiments performed
at AVL. I wrote the paper with inputs from Dr Niklas Nordin and Henry
Weller. In addition, I presented it at the 5th Joint ASME/JSME Fluids
Engineering Conference, 2007, San Diego, USA.

Paper III - Three Dimensional Simulation of Diesel Spray Ignition and Flame Lift-Off Using OpenFOAM and KIVA-3V CFD Codes

The paper originated from a comparison of OpenFOAM results I generated to
KIVA-3V results generated by Dr Feng Tao. Thanks to the large ECN
database, it was also possible to compare the results to experimental data. We
compared the effects of varying amounts of oxygen/EGR and ambient
temperatures using the two codes. There was also a limited comparison of the
effects of using different grids and injection positions (published in the
Appendix of the article). It was found that OpenFOAM produces much longer
flames than KIVA-3V, as well as short flame lift-off lengths. It is possible that
KIVA-3V yields longer flame lift-off lengths since the atomization length is
prescribed in the code. The OpenFOAM simulations did not use an
atomization model, and thus yielded much shorter liquid penetrations.
Unfortunate use of the RNG k-ε turbulence model together with the limited
Linear scheme is believed to be an underlying reason for the long penetration
of the flame. With the knowledge gained from the studies published in Paper
IV, I believe the results would have been better if SuperBee interpolation had
been used for the advection scheme.

I setup, ran and post-processed the OpenFOAM simulations, while the KIVA-3V simulations were setup, ran and post-processed by Dr Feng Tao. The paper was written by me and Dr Feng Tao. I presented it at the SAE World Congress, 2008, Detroit, USA.

Paper IV - Influence of Advection Schemes In The Prediction of Diesel Spray and Fuel Vapour Distributions

As mentioned regarding the previous paper, the authors were not satisfied by OpenFOAM's overprediction of flame lengths. Simulations indicated that the scheme might have a strong influence on the fuel vapour distribution. Therefore, a more extensive study of the influence of the scheme (and effects of the initial parameters on spray development) was undertaken. It was found that while the scheme does have a large influence, the initial turbulence parameters can reduce or enhance its influence. If the initial viscosity of the turbulence is low, the SuperBee scheme was shown to be the best choice for interpolation of the advection scheme.

I setup, ran and post-procssed the simulations, and wrote the paper together with Dr Feng Tao. It was presented at ILASS, 2008, Como Lake, Italy.

Appendix A

Implementation in OpenFOAM

A.1   Rhie-Chow Interpolation in OpenFOAM

OpenFOAM is relatively new, open source code that is not fully documented. Therefore the intention of the author here is to extend the documentation, and at the same time share some additional knowledge that has been gained during the course of this work. One very important aspect of CFD is Rhie-Chow correction, which will therefore be described here. Rhie-Chow correction is absolutely necessary for flow simulations using a collocated grid, since it removes oscillations in the solution, which occur if the pressure gradient does not depend on the pressure in adjacent cells, thus allowing a "jigsaw" pattern to develop.

Some basic information about the notation in OpenFOAM is needed to describe how it works. Partial Differential Equations in OpenFOAM are solved by setting up the appropriate matrix system:

$$\texttt{fvm::operation(coefficient,U)} \tag{A.1}$$

This means that the solver is to solve for `U`, and `coefficient` is a coefficient which can vary in space and/or time, or be a constant. Operations like this will be described many times throughout this section, and it is important to understand the nomenclature. Further, this section contains two velocities: $\mathbf{U}$, which is used for the flux and held constant when the momentum equations are solved; and $U_{\mathrm{x,y,z}}$, which is the velocity we solve for. All equations containing $U_{\mathrm{x,y,z}}$ are actually three equations, referring to relationships in the x-, y-, and z-direction respectively.

Rhie and Chow is usually regarded as a correction proportional to the difference between the pressure gradient at the face and the interpolated

pressure gradient at the face. For example (from Ferziger & Peric [82]), for a cell face, the velocity is corrected by:

$$u_j = \overline{u_j} - \Delta \overline{\left(\frac{1}{A_p^{u_j}}\right)} \left(\frac{\partial p}{\partial x_j} - \overline{\left(\frac{\partial p}{\partial x_j}\right)}\right) \tag{A.2}$$

where the overbar indicates interpolation, and Δ is related to the mesh size. OpenFOAM does not have such an explicit term in the equations, which makes it difficult to see how the Rhie-Chow correction is applied. Indeed, OpenFOAM applies a correction that some would call 'in the spirit of Rhie and Chow'. For this description, the `icoFoam` code from OpenFOAM will be used to illustrate how this correction is implemented. `icoFoam` is a solver for transient incompressible laminar flow of Newtonian fluids. For this type of flow, the momentum equation in vector form would be:

$$\frac{\partial U_{\mathrm{x,y,z}}}{\partial t} + (\mathbf{U} \cdot \nabla)U_{\mathrm{x,y,z}} - \nabla \cdot (\nu \nabla U_{\mathrm{x,y,z}}) = -\frac{1}{\rho} \nabla p \tag{A.3}$$

Where the above equation is solved for $U_{x,y,z}$ in each of the three directions. If we consider the `UEqn.H` in `icoFoam`, the convection term is slightly different.

```
fvVectorMatrix UEqn                    (A.4)
(
    fvm::ddt(U)
+   fvm::div(phi, U)
−   fvm::laplacian(nu, U)
);
```

Equation A.4 has no right hand side, and there is a field named `phi` (ϕ) instead of the **U**-term. ϕ is (for incompressible flows) the volume velocity flux defined at the faces of each cell. It is used because OpenFOAM utilizes the Gauss theorem, which is frequently used in applied mathematics, and defines the transform of a volume integral into a surface integral. For an incompressible case, equation A.3 is integrated over a volume V with face S, and the second term can be rewritten as:

$$\int_V \nabla \cdot (\mathbf{U}U_{\mathrm{x,y,z}})\, dV \;=\; \int_S (\mathbf{U}U_{\mathrm{x,y,z}})_f \cdot \hat{\mathbf{n}}\, dS =$$
$$= \sum_i U_{\mathrm{x,y,z}}^{f,i}(\mathbf{U}^{f,i} \cdot \mathbf{S}_{\mathbf{f}i}) \;=\; \sum_i \phi^i U_{\mathrm{x,y,z}}^{f,i} \tag{A.5}$$

where

$$\phi = \mathbf{U}^{f,i} \cdot \mathbf{S_f} \tag{A.6}$$

$\mathbf{U}^{f,i}$ is the velocity that will be held constant when the equation for pressure is solved, while $\mathbf{U}$ is the vector velocity that will be solved for. It is important to note the difference in the subscript when the surface integral is introduced; subscript f indicates that the term should be evaluated on the face. ϕ is defined as the scalar product of the cell face velocity and the cell face normal (eq. A.6). The magnitude of the cell face normal is the cell face area.

We can now connect OpenFOAM's equation to its analytical counterpart:

$$\int_V \nabla \cdot (\mathbf{U} U_{\mathrm{x,y,z}}) \, dV \Longrightarrow \texttt{fvm::div(phi,U)} \tag{A.7}$$

In the above equation, $\mathbf{U}$ is turned into $\texttt{phi}$ (by equation A.6). $U_{\mathrm{x,y,z}}$ is the velocity we solve for, which is turned into $\texttt{U}$ in OpenFOAM. There is also a difference in that $\texttt{phi}$ and $U_{\mathrm{x,y,z}}^{\mathrm{f}}$ are evaluated on the surfaces of the cell, while $\texttt{U}$ is defined in the cell centre. The way in which the face and cell values are obtained from each other is discussed in section A.2.

We are now ready to return to equation A.4, which does not include the pressure gradient (thus contributing to the separation of pressure and velocity). The code adds the influence of p to U in another way, which is described below.

Recalling from [82], the discretized momentum equation would be this matrix system:

$$\mathcal{A}[U_{\mathrm{x,y,z}}] = \mathcal{H} - \nabla[p] \tag{A.8}$$

$\mathcal{A}$ is the numerical equivalent of the operators in equation A.3 operating on $U_{\mathrm{x,y,z}}$, and $\mathcal{H}$ the one containing terms without $U_{\mathrm{x,y,z}}$. They are created by issuing the commands $\texttt{UEqn.A()}$ and $\texttt{UEqn.H()}$, respectively. [.] denotes the numerical approximation of the corresponding variable. This system is solved by dividing by $\mathcal{A}$, which results in:

$$[\mathbf{U}] = \frac{\mathcal{H}}{\mathcal{A}} - \frac{1}{\mathcal{A}}\nabla[p] \tag{A.9}$$

Equation A.9 cannot be solved at this stage, since we have not updated the pressure yet. If the problem of interest includes transport of a scalar property, such as enthalpy or the mass fraction of a chemical compound, we need a predictor for $\mathbf{U}$, which is calculated using the pressure from the previous iteration:

$$\texttt{solve(UEqn == - fvc::grad(p));} \tag{A.10}$$

This is called a momentum predictor of $\mathbf{U}$. So far only the momentum equation has been used, but we also have the continuity equation, which is used to create an equation for pressure. The first term on the right hand side of equation A.10 is needed for the pressure equation, and given a special notation:

$$\texttt{U* = UEqn.H()/UEqn.A();} \tag{A.11}$$

The velocity from A.11 does not satisfy continuity, and lacks influence of pressure. To create the equation for pressure, we take the divergence of equation A.9:

$$\nabla \cdot [\mathbf{U}] = \nabla \cdot ([\mathbf{U}^*]) - \nabla \cdot \left(\frac{1}{\mathcal{A}} \nabla [p] \right) \tag{A.12}$$

The left hand side is zero for incompressible flows, since it represents the correct velocity. Equation A.12 is then:

$$\nabla \cdot ([\mathbf{U}^*]) = \nabla \cdot \left(\frac{1}{\mathcal{A}} \nabla [p] \right) \tag{A.13}$$

The left hand side will be treated explicitly, since we now need to find the pressure, and thus keep the velocity constant. In OpenFOAM, this is done by utilizing $\texttt{fvc}$ instead of $\texttt{fvm}$. The velocity $\mathbf{U}^*$ is replaced by the velocity flux ϕ, since the face velocities will be used to evaluate the term. The resulting equation is then:

$$\begin{aligned} &\texttt{surfaceScalarField phi =} \\ &\qquad\qquad \texttt{fvc::interpolate(U) \& mesh.Sf()} \quad \text{(A.14)} \\ &\texttt{volScalarField rUA = 1.0/UEqn.A();} \quad\qquad \text{(A.15)} \\ &\texttt{fvScalarMatrix pEqn} \qquad\qquad\qquad\qquad\qquad \text{(A.16)} \\ &\texttt{(} \\ &\quad \texttt{fvm::laplacian(rUA, p) == fvc::div(phi)} \\ &\texttt{);} \end{aligned}$$

A feature that cannot be seen in this formulation is that OpenFOAM again uses the Gauss theorem. Thus, it is not necessary to calculate a second derivative of p, but only a first derivative. This derivative is needed on the cell faces, and it is evaluated by using the cell centre values of the pressure.

When the PISO loop is finished, the velocity is corrected with the correct pressure gradient.[1]

---

[1]Actually this is computed at the end of each PISO loop, before the boundary conditions are corrected. The code used as an example here is $\texttt{icoFoam}$, but the method is the same in most of the other codes available in OpenFOAM.

$$\texttt{U -= rUA*fvc::grad(p);} \tag{A.17}$$

The gradient in equation A.17 is again evaluated using the Gauss theorem, and therefore no gradient calculation is necessary. Instead, only the pressure on the cell face is needed.

To summarize, there are four important points regarding the Rhie-Chow correction in OpenFOAM.

1. `phi` does not include any effect of pressure when solving the continuity equation
2. `rUA` does not include any effect of pressure when solving for continuity and the final velocity corrector
3. The Laplacian-term of p uses the value of the gradient of p on the cell face. The gradient is calculated using neighbouring cells, not neighbouring faces
4. The gradient term of p is calculated from the cell face values of p.

This method gives an oscillation-free velocity "with the spirit of Rhie-Chow", even though there is no explicit Rhie-Chow correction.

A.2 Formulating the Momentum Equation Matrix in OpenFOAM

In Paper 4 there is a concise description of the way in which different schemes for different terms can be used in OpenFOAM. This will be explained in more detail here, from equation to matrix. We start off by simplifying equation A.3, by assuming stationary incompressible non-viscous flow:

$$\mathbf{U} \cdot \nabla U_{\mathrm{x}} = \nabla \cdot (\mathbf{U} U_{\mathrm{x}}) = -\frac{1}{\rho}\frac{\partial p}{\partial x} \tag{A.18}$$

$$\mathbf{U} \cdot \nabla U_{\mathrm{y}} = \nabla \cdot (\mathbf{U} U_{\mathrm{y}}) = -\frac{1}{\rho}\frac{\partial p}{\partial y} \tag{A.19}$$

$$\mathbf{U} \cdot \nabla U_{\mathrm{z}} = \nabla \cdot (\mathbf{U} U_{\mathrm{z}}) = -\frac{1}{\rho}\frac{\partial p}{\partial z} \tag{A.20}$$

$$\tag{A.21}$$

where the equations are re-written using the continuity equation. In OpenFOAM they would be written (according to the Rhie-Chow method explained in the previous section) as:

$$\tag{A.22}$$
```
fvVectorMatrix UEqn
(
  fvm::div(phi, U)
);
```

Rho is not included in the above equation because OpenFOAM uses $\overline{p} = \frac{p}{\rho}$ for many incompressible codes instead of actual p, although this is only visible in the dimension on initial p. For simplicity, we will only consider flow in the y-direction. This saves space, as we now only have one equation:

$$\nabla \cdot (\mathbf{U} U_{\mathrm{y}}) = -\frac{1}{\rho}\frac{\partial p}{\partial y} \tag{A.23}$$

This term is integrated over the cell volumes used for the finite volume method, yielding:

$$\int_{V} \nabla \cdot (\mathbf{U} U_{\mathrm{y}})\, dV = \int_{S} (U_{\mathrm{y}})_{\mathrm{f,scheme}}\, (\mathbf{U})_{\mathrm{f,linear}} \cdot \hat{\mathbf{n}}\, dS$$

$$= \sum_{i} (\mathbf{U})_{\mathrm{f,linear}}^{i} \cdot \mathbf{S}_{\mathrm{f}}^{i} (U_{\mathrm{y}})_{\mathrm{f,scheme}}^{i} = -\int_{V} \frac{\partial p}{\partial y}\, dV \tag{A.24}$$

Where all the variables are evaluated on face i, belonging to the cell in question with volume V and surface S. Two interpolations are then required to calculate the term on the left-hand side: one for $(U_y)^i_{f,scheme}$, which is the velocity to be solved for; and one for $(\mathbf{U})^i_{f,linear}$, the velocity that is kept constant as the linear equation system is solved. As indicated by the subscript, the second velocity is usually interpolated by linear interpolation. The faceflux, (`phi` in OpenFOAM) is either mass-flux in compressible code, or volume-flux in incompressible code. Using anything other than linear for this term could cause problems later when the divergence term is evaluated. For instance, the faceflux on certain faces could be zero due to use of upwind/downwind interpolation, and thus the TVD scheme for the divergence term would not perform as well.
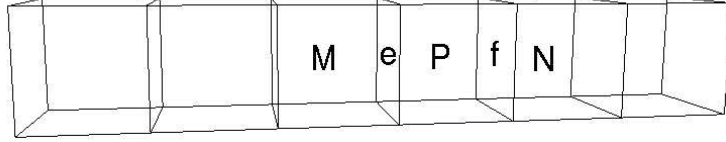

Figure A.1: Line mesh consisting of six cells.

Following the nomenclature in figure A.1, we can write equation A.24 for cell P:

$$\underbrace{(\mathbf{U})^e_{linear} \cdot \mathbf{S}_e}_{\phi_e} (U_y)^e_{scheme} + \underbrace{(\mathbf{U})^f_{linear} \cdot \mathbf{S}_f}_{\phi_f} (U_y)^f_{scheme} = |\mathbf{S}_e|p_e - |\mathbf{S}_f|p_f \quad \text{(A.25)}$$

If OpenFOAM used a staggered grid setup, the above equation could be solved for the face values *per se*, and the only interpolation needed would be the linear interpolations for the flux term and pressure. Instead, OpenFOAM solves for the cell-centred values directly, requiring more interpolation. The general equation for first/second order interpolation of the cell-centred variable U to the face is given by

$$U_f = \lambda_f(U_P - U_N) + U_N \qquad U_e = \lambda_e(U_M - U_P) + U_P \qquad \text{(A.26)}$$

where λ_f and λ_e vary between 0 and 1 depending on the chosen scheme. If we insert this expression for U_f and U_e into equation A.25, we get the equations used to compile the linear matrix system for solving the equations. For cell P this equation is:

$$\phi_e(\lambda_e(U_M - U_P) + U_P) + \phi_f(\lambda_f(U_P - U_N) + U_N) =$$
$$\phi_e\lambda_e U_M + (\phi_e(1 - \lambda_e) + \phi_f\lambda_f)U_P + \phi_f(1 - \lambda_f)U_N =$$
$$|\mathbf{S}_e|p_e - |\mathbf{S}_f|p_f \qquad (A.27)$$

This equation is valid for all cells, although special treatment is needed for the boundary cells. The resulting matrix formed from this equation is then:

$$\begin{bmatrix} \cdots & \cdots & \cdots & \cdots & \cdots \\ \cdots & \phi_e\lambda_e & \phi_e(1-\lambda_e)+\phi_f\lambda_f & \phi_f(1-\lambda_f) & \cdots \\ \cdots & \cdots & \cdots & \cdots & \cdots \end{bmatrix} \begin{bmatrix} \cdots \\ U_M \\ U_P \\ U_N \\ \cdots \end{bmatrix}$$
$$= \begin{bmatrix} \cdots \\ |\mathbf{S}_e|p_e - |\mathbf{S}_f|p_f \\ \cdots \end{bmatrix} \qquad (A.28)$$

which results in a sparse matrix having elements only on the sub-,super- and main- diagonal. This is the matrix that is calculated when the command `fvVectorMatrix UEqn` is issued in OpenFOAM. It is usually solved by ordinary LU decomposition. Note that this equation is solved for the cell-centered values. As mentioned in the previous section, this equation is not solved directly, but through the procedure described there.

Appendix B

Variable Definitions and Dimensionless Numbers

$$S = \nabla \mathbf{U} \; : \; \mathrm{dev}(\mathrm{sym}(\nabla \mathbf{U})) \tag{B.1}$$

$$f = -0.3\mathrm{e}^{-\left(\min\left[\left(\frac{\rho k^2}{\mu \varepsilon}\right)^2, 50\right]\right)} \tag{B.2}$$

$$R_{\mathrm{RNG}} = \eta \frac{-\frac{\eta}{\eta_0} + 1}{\beta \eta^3 + 1} \tag{B.3}$$

$$\eta = \sqrt{(|S|)} \frac{k}{\varepsilon} \tag{B.4}$$

$$\mathrm{Re}_d = \frac{\rho_d |\mathbf{u}_{\mathrm{rel}}| r}{\mu_{\mathrm{l}}} \tag{B.5}$$

$$\mathrm{We} = \frac{\rho |\mathbf{u}_{\mathrm{rel}}|^2 r}{\sigma} \tag{B.6}$$

$$\mathrm{Oh} = \frac{\sqrt{We_{\mathrm{l}}}}{\mathrm{Re}_{\mathrm{l}}} \tag{B.7}$$

$$\mathrm{Ta} = \mathrm{Oh}\sqrt{\mathrm{We}_{\mathrm{g}}} \tag{B.8}$$

$$\mathrm{Co} = \frac{\mathbf{U} \cdot \mathbf{d}}{|\mathbf{d}|^2 \Delta t} \tag{B.9}$$

$$\mathrm{Sc} = \frac{\nu}{D_{\mathrm{v}}} \tag{B.10}$$

Model parameter	Numerical Value
B_0	0.61
B_1	40.0
C_τ	1.0
C_{RT}	0.1
$m_{\mathrm{s,limit}}$	0.4
We_{limit}	6

Table B.1: KHRT model constants

Bibliography

[1] Tarr, J.A. and McShane, C., 1997. "The centrality of the horse to the nineteenth-century american city". In *The Making of Urban America*. Scholarly Resources Inc., pp. 105–130.

[2] World Health Organization, 2003. "Health aspects of air pollution with particulate matter, ozone and nitrogen dioxide". *EUR/03/5042688*.

[3] Kågeson, Per, www.bilsweden.se. Dieselmotorn på kort och lång sikt.

[4] www.dieselnet.com/standards/eu/ld.html, 2007. Emission standards.

[5] United States Environmental Protection Agency, 2007. Light-Duty Automotive Technology and Fuel Economy Trends: 1975 through 2007.

[6] Lagerquist, M., 2007. Energiläget i siffror 2007, Energy in Sweden 2007 Facts and Figures.

[7] Patterson, M.A., Kong, S.C, Hampson, G.J. and Reitz, Rolf D., 1994. "Modeling the Effects of Fuel Injection Characteristics on Diesel Engine Soot and NOx Emissions". *SAE Paper 940523*.

[8] Patterson, M., and Reitz, R. D., 1998. "Modeling the effects of fuel spray characteristics on diesel engine combustion and emission". *SAE Paper 980131*.

[9] O'Rourke, P.J., and Amsden, A.A., 1987. "The tab method for numerical calculation of spray droplet breakup". *SAE Paper 872089*.

[10] Weller, H., Tabor, G., Jasak, H., and Fureby, C., 1998. "A Tensorial Approach to Computational Continuum Mechanics using Object Orientated Techniques". *Computers in Physics,* **12**(6), pp. 620–631.

[11] Jasak, H., Weller, H. G. and Nordin, N., 2004. "In-Cylinder CFD Simulation Using a C++ Object-Oriented Toolkit". *SAE Paper 2004-01-0110*.

[12] Stiesch, G., 2003. *Modeling Engine Spray and Combustion Processes*. Springer Verlag Berlin Heidelberg New York.

[13] Faeth, G. M., Hsiang, L-P and Wu, P-K, 1995. "Structure and Breakup Properties of Sprays". *International Journal of Multiphase Flow,* **21**, pp. 99–127.

[14] Badock, C., Wirth, R., Fath, A., and Leipertz, A., 1999. "Investigation of cavitation in real size diesel injection nozzles". *International Journal of Heat and Fluid Flow,* **20**(5).

[15] Winklhofer, E., Kull, E., Kelz, E., and Morozov, A., 2001. "Comprehensive Hydraulic and Flow Field Documentation in Model Throttle Experiments Under Cavitation Conditions". In Proceedings of the ILASS-Europe Annual Meeting, Zurich, Switzerland, pp. 574–579.

[16] Arcoumanis, C., Gavaises, M., Flora, H., Roth, H., 2001. "Visualisation of cavitation in diesel engine injectors". *Mecanique & Industries,* **2**(5).

[17] Blessing, M., König, G., Krüger, C., Michels, U., and Schwarz, V., 2003. "Analysis of Flow and Cavitation Phenomena in Diesel Injection Nozzles and its Effects on Spray and Mixture Formation". *SAE Paper 2003-01-1358.*

[18] Schmidt, D., Rutland, C., and Corradini, M., 1997. "A numerical study of cavitating flow through various nozzle shapes". *SAE Paper 971597.*

[19] Yuan, W., and Schnerr, G., 2003. "Numerical Simulation of Two-Phase Flow in Injection Nozzles: Interaction of Cavitation and External Jet Formation". *Journal of Fluids Engineering,* **125**, pp. 963–969.

[20] Mulemane, A., Subramaniyam, S., Lu, P., Han, J., Lai, M., and Poola, R., 2004. "Comparing Cavitation in Diesel Injectors Based on Different Modeling Approaches". *SAE Paper 2004-01-0027.*

[21] Martynov, S., Mason, D., Heikal, M. R., Sazhin, S. S., and Gorokhovski, M., 2006. "Modelling of Cavitation Flow in a Nozzle and its Effect on Spray Development". In International Heat Transfer Conference.

[22] Yuan, W., Sauer, J., and G.H., S., 2001. "Modeling and Computation of Unsteady Cavitation Flows in Injection Nozzles". *Mechanique & Industries,* **2**, pp. 383–394.

[23] Masuda, R., Fuyuto, T., Nagaoka, M., Berg, E., and Tatschl, R., 2005. "Validation of diesel fuel spray and mixture formation from nozzle internal flow calculation". *SAE Paper 2005-01-2098.*

[24] Ning, W., 2007. "Development of a next-generation spray and atomization model using an eulerian-lagrangian methodology". PhD thesis, University of Wisconsin - Madison.

[25] Roth, H., Giannadakis, E., Gavaises, M., Arcoumanis, C., Omae, K., Sakata, I., Nakamura, M., and Yanagihara, H., 2005. "Effect of multi-injection strategy on cavitation development in diesel injector nozzle holes". *SAE Paper 2005-01-1237.*

[26] Nouri, J., Mitroglou, N., Yan, Y., and Arcoumanis, C., 2007. "Internal flow and cavitation in a multi-hole injector for gasoline direct-injection engines". *SAE Paper 2007-01-1405.*

[27] Payri, R., Margot, X., and Salvador, F., 2002. "A Numerical Study of the Influence of Diesel Nozzle Geometry on the Inner Cavitating Flow". *SAE Paper 2002-01-0215.*

[28] Schmidt, D.P., Rutland, C.J. and Corradini, M.L., 1999. "A Fully Compressible Two-Dimensional Model of High Speed Cavitating Nozzles". *Atomization and Sprays,* **9**.

[29] Vortmann, C., Schnerr, G., and Seelecke, S., 2003. "Thermodynamic Modeling and Simulation of Cavitating Nozzle Flow". *International Journal of Heat and Fluid Flow,* **24**.

[30] Weller, H. G., 2006. A New Approach to VOF-based Interface Capturing Methods for Incompressible, Compressible and Cavitating Flow. Tech. Rep. TR/HGW/07, OpenCFD Ltd., October.

[31] Wallis, G. B., 1969. *One-dimensional Two-phase Flow.* McGraw-Hill, New York.

[32] Chung, M.-S., Park, S.-B., and Lee, H.-K., 2004. "Sound speed criterion for two-phase critical flow". *Journal of Sound and Vibration,* **276**, pp. 13–26.

[33] Ubbink, O., 1997. "Numerical prediction of two fluid systems with sharp interfaces". PhD thesis, Imperial College.

[34] Poinsot, T.J., and Lele, S.K., 1992. "Boundary conditions for direct simulations of compressible viscous reacting flows". *Journal of Computational Physics,* **101**, pp. 103–129.

[35] Huh, K.Y., and Gosman, A.D., 1990. "Atomization Mechanism of Fuel Injection". *ILASS.*

[36] Kralj, C., 1995. "Numerical Simulation of Diesel Spray Processes". PhD thesis, Imperial College of Science Technology and Medicine.

[37] Peng, D.-Y., and Robinson, D. B., 1976. "A new two-constant equation of state". *Industrial & Engineering Chemistry Fundamentals,* **15**, pp. 59–64.

[38] Xie, W. F., Liu, T. G., and Khoo, B. C., 2006. "Application of a one-fluid model for large scale homogeneous unsteady cavitation: The modified Schmidt model". *Computers & Fluids,* **35**, pp. 1177–1192.

[39] de Villiers, E., Gosman, A., and Weller, H., 2004. "Large Eddy Simulation of Primary Diesel Spray Atomization". *SAE Paper 2004-01-0100.*

[40] Befrui, B., Corbinelli, G., Robart, D., and Reckers, W., 2008. "LES Simulation of the Internal Flow and Near-Field Spray Structure of an Outward-Opening GDi Injector and Comparison with Imaging Data". *SAE Paper 2008-01-0137.*

[41] Ménard, T., and Berlemont, A., 2007. "Interface tracking with a coupled level set/vof/ghost fluid method: Application to jet atomization". *Proceedings of FEDSM2007,* **FEDSM2007-37377**.

[42] Vuorinen, V., Larmi, M., and Fuchs, L., 2008. "Large-Eddy Simulation on the Effect of Droplet Size Distribution on Mixing of Passive Scalar in a Spray". *SAE Paper 2008-01-0933*.

[43] Blokkeel, G., Barbeau, B., and Borghi, R., 2003. "A 3D Eulerian Model to Improve the Primary Breakup of Atomizing Jet". *SAE Paper 2003-01-0005*.

[44] Lebas, R., Blokkeel, G., Beau, P.-A., and Demoulin, F.-X., 2005. "Coupling Vaporization Model With the Eulerian-Lagrangian Spray Atomization (ELSA) Model in Diesel Engine Conditions". *SAE 2005-01-0213*.

[45] Iyer, V. and Abraham, J., 2003. "An Evaluation of a Two-Fluid Eulerian-Liquid Eulerian-Gas Model for Diesel Sprays". *Journal of Fluids Engineering,* **125**, pp. 660–669.

[46] Jones, W. and Launder, B., 1972. "The prediction of laminarization with a two-equation model of turbulence". *Int. J. Heat Mass Transfer,* **15**, pp. 301–314.

[47] Yakhot, V. and Orzag, S.A., 1986. "Renormalization Group Analysis of Turbulence". *I. Basic Theory J. Sci. Comput.*

[48] Launder, B. and Sharma, B., 1975. "Application of the energy dissipation model of turbulence to the calculation of flow near a spinning disc". *Lett. Heat and Mass Transfer,* **1**, pp. 131–138.

[49] Amsden, A.A., O'Rourke, P.J. and Butler, T.D., 1989. "Kiva-ii: A computer program for chemically reactive flows with sprays". *LA-11560-MS, May.*

[50] Gore, R., and Crowe, C. T., 1989. "Effect of particle size on modulating turbulent intensity". *International Journal of Multiphase Flow,* **15**(2), pp. 279–285.

[51] Crowe, C., Sommerfeld, M., and Tsuji, Y., 1998. *Multiphase Flows with Droplets and Particles.* CRC Press LLC.

[52] Nordin, N., 2001. "Complex chemistry modeling of diesel spray combustion". PhD thesis, Dept. of Thermo and Fluid Dynamics, Chalmers University of Technology, Göteborg.

[53] Press, W.H., Teukolsky, S.A., Vetterling, W.T. and Flannery, B.P., 2002. *Numerical Recipes in C++: The Art of Scientific Computing*, 2:nd ed. Cambridge University Press.

[54] Karlsson, J. A. J., 1995. "Modeling Auto-Ignition, Flame Propagation and Combustion in Non-stationary Turbulent Sprays". PhD thesis, Chalmers University of Technology, Göteborg.

[55] Venugopal, R., and Abraham, J., 2007. "A numerical investigation of flame lift-off in diesel jets". *Combustion Science and Technology,* **179**, pp. 2599–2618.

[56] P.K. Senecal, E. P., and Richards, K., 2003. "Multidimensional Modeling of Direct-Injection Diesel Spray Liquid Length and Flame Lift-off Length using CFD and Parallel Detailed Chemistry". *SAE 2003-01-1043*.

[57] Tap, F., and Veynante, D., 2005. "Simulation of Flame Lift-off on a Diesel Jet Using a Generalized Flame Surface Density Approach". *Proceedings of Combustion Inst.*(30), pp. 919–926.

[58] Chomiak, J. and Karlsson, J.A.J., 1996. "Flame Liftoff in Diesel Sprays". *Twenty-Sixth Symposium (International) on Combustion/The Combustion Institute*, pp. 2557–2564.

[59] Tao, F., 2003. "Numerical Modeling of Soot and NOx Formation in Non-Stationary Diesel Flames with Complex Chemistry". PhD thesis, Chalmers University of Technology, Göteborg.

[60] Macpherson, G. B., Nordin, N., and Weller, H. G., 2008. "Particle tracking in unstructured, arbitrary polyhedral meshes for use in cfd and molecular dynamics". *Communications in Numerical Methods in Engineering*.

[61] Schmalzing, C.-O, Stapf, P., Maly, R.R., Renner, G., Stetter, H., and Dwyer, H.A., 1999. "A holistic hydraulic and spray model - liquid and vapor phase penetration of fuel sprays in di diesel engines". *SAE Paper 1999-01-3549*.

[62] Kimura, S., Kosaka, H., Matsui, Y.,and Himeno, R., 2004. "A numerical simulation of turbulent mixing in transient spray by les". *SAE Paper 2004-01-2014*.

[63] Reitz, R.D., 1987. "Modeling Atomization Processes in High-Pressure Vaporizing Sprays". *Atomization and Spray Technology,* **3**, pp. 309–337.

[64] Park, S. W., Kim, H. J., and Lee, C. S., 2003. "Investigation of atomization characteristics and prediction accuracy of hybrid models for high-speed diesel fuel sprays". *SAE Paper 2003-01-1045*.

[65] Rotondi, R., Bella, G., Grimaldi, C., and Postrioti, L., 2001. "Atomization of High-Pressure Diesel Spray: Experimental Validation of a New Breakup Model". *SAE paper 2001-01-1070*.

[66] Bianchi, G.M., and Pelloni, P., 1999. "Modeling the diesel fuel spray breakup by using a hybrid model". *SAE Paper 1999-01-0226*.

[67] Lee, J-H and Goto, S., 2000. "Comparison of spray characteristics in butane and diesel fuels by numerical analysis". *SAE Paper 2000-01-2941*.

[68] O'Rourke, P., 1981. "Collective Drop Effects on Vaporizing Liquid Sprays". PhD thesis, Department of Mechanical and Aerospace Engineering, Princeton University.

[69] Schmidt, D., and Rutland, C., 2000. "A New Droplet Collision Algorithm". *Journal of Computational Physics,* **164**, pp. 62–80.

[70] Gustavsson, J., and Golovitchev, V., 2004. "3D Simulation of Multiple Injections in DI Diesel Engine". In The Sixth International Symposium on Diagnostics and Modeling of Combustion in Internal Combustion Engines, COMODIA.

[71] Peng Kärrholm, F., 2006. *Numerical Modelling of Diesel Spray Injection and Turbulence Interaction*. Licentiate Thesis, Department of Applied Mechanics, Chalmers University of Technology.

[72] van Leer, B., 1977. "Towards the ultimate conservative difference scheme iii. upstream-centered finite-difference schemes for ideal compressible flow". *J. Comp. Phys.,* **23**, pp. 263–75.

[73] Sandia National Laboratories, 2007. Engine combustion network (public.ca.sandia.gov/ecn).

[74] Hilbert, R., and Thévenin, D., 2002. "Autoignition of turbulent nonpremixed flames investigated using direct numerical simulations". *Combustion and Flame,* **128**, pp. 22–37.

[75] Hilbert, R., Tap, F., El-Rabii, H., and Thévenin, D., 2004. "Impact of detailed chemistry and transport models on turbulent combustion simulations". *Progress in Energy and Combustion Science,* **30**, pp. 61–117.

[76] Siebers, D. L., and Higgins, B. S., 2000. Effects of Injector Conditions on the Flame Lift-Off Length of DI Diesel Sprays. Tech. Rep. 2000-8249, Sandia National Laboratories.

[77] Husberg, T., Denbratt, I., and Karlsson, A., 2008. "Analysis of advanced multiple injection strategies in a heavy-duty diesel engine using optical measurements and cfd simulations". *SAE Paper 2008-01-1328.*

[78] Payri, F., Bermúdez, V., Payri, R., and Salvador, F., 2004. "The influence of cavitation on the internal flow and the spray characteristics in diesel injection nozzles". *Fuel,* **83**, pp. 419–431.

[79] Gavaises, M., Arcoumanis, C., Roth, H., Choi, Y., and Theodorakakos, A., 2002. "Nozzle flow and spray characteristics from vco diesel injector nozzles". *SAE Paper 2002-30-0002.*

[80] Lucchini, T., D'Errico, G., Jasak, H., and Tukovic, Z., 2007. "Automatic mesh motion with topological changes for engine simulation". *SAE Paper 2007-01-0170.*

[81] Ochoterena, R., Larsson, M., Andersson, S., and Denbratt, I., 2008. "Optical studies of spray development and combustion characterization of oxygenated and fischer-tropsch fuels". *SAE Paper 2008-01-1393.*

[82] Ferziger, J.H. and Peric, M., 1999. *Computational Methods for Fluid Dynamics*. Springer.

Paper II

FEDSM2007-37518

MODELLING INJECTOR FLOW INCLUDING CAVITATION EFFECTS FOR DIESEL APPLICATIONS

F. Peng Kärrholm[*]
Department of Applied Mechanics
Chalmers University of Technology
Sweden
Email: fabian.peng-karrholm@chalmers.se

Henry Weller
OpenCFD Ltd.
Caversham, Reading
UK

Niklas Nordin
Scania CV AB
Södertälje
Sweden

ABSTRACT

In this paper, cavitation and pressure parameters measured in a model diesel injector are compared to data acquired by numerical simulations using a new code developed for the Open-FOAM platform, which uses a barotropic equation of state together with the homogeneous equilibrium assumption. It is a viscid code, allowing both compressible liquid and vapour to be modelled. The mass flow and cavitation probabilities obtained from the simulations are compared to data obtained in experiments performed at AVL's laboratories, in which the flow through an almost two-dimensional nozzle was examined. The experimental data used include pressure profiles and cavitation images. The model proved to be able to predict cavitation probabilities, mass flows, and the occurrence of super-cavitation in the channel. In addition, it proved to be stable in its dependency on physical parameters, and grid independent.

NOMENCLATURE

A   flow area of the nozzle
A_i area of a face in the nozzle in flow direction
Cd   discharge coefficient
p   pressure
Δp pressure difference
U   velocity
$\dot{m}$ mass flow
γ vapour fraction

μ_g vapour viscosity
μ_l liquid viscosity
μ_f fluid viscosity
ρ fluid density
ρ_v vapour density
ρ_l liquid density
$\rho_{v,sat}$ vapour density at saturation
$\rho_{l,sat}$ liquid density at saturation
ψ_v vapour compressibility
ψ_l liquid compressibility

INTRODUCTION

In Diesel engines and direct injection spark ignition engines, fuel is injected into the combustion chamber by high pressure. Ideally, the fuel should atomise, form small droplets, and eventually evaporate completely in order to obtain a mixture that can be easily combusted without formation of soot or NO_x. Important features of the atomisation, including the size of the initial droplets and the fragmentation processes, are mainly governed by the flow in the nozzle [1] which ejects the spray. It is therefore important to study the flow inside the nozzle, to find out how it is linked to the flow in the combustion cylinder.

When a high velocity fluid passes through a contraction like a nozzle, a pocket of low pressure is formed in the wake of its edge. In this wake the pressure can decrease below the saturation pressure, and thus cause the liquid to cavitate. The size of the cavitation bubbles thereby formed depends on several factors, including (*inter alia*) the injection pressure, geometry, and

---

[*]Address all correspondence to this author.

1

smoothness of the interior of the nozzle, and the properties of the fluid. For example, if the fluid is pushed through the nozzle sufficiently slow, there will be no cavitation and ordinary pipe flow will occur.

Cavitation introduces vapour bubbles into the flow. It also increases the maximum velocity, for two reasons. If there is vapour along the walls, the liquid will not have a no-slip boundary condition, since the vapour by the wall will not be stationary. This allows a higher velocity of the liquid, which is required when the pressure over the nozzle is high. The velocity is also increased since the liquid can not fill the entire channel. When the vapour bubbles formed in the nozzle reach the combustion chamber, both the bubbles and the liquid surrounding them will be heated by the gas in the chamber. The liquid will evaporate faster if it has already been partially evaporated by cavitation, and thus the entire atomisation process will be accelerated.

The point where the fluid is no longer cavitating is called the re-attachment point, if there is no such point the fluid will be super-cavitating and the cavitation region will extend throughout the entire nozzle. Super-cavitation changes the atomisation behaviour significantly, since the spray's cone angle is severely reduced when it exits the injector, resulting in a steady flow with fairly large scale disturbances on the surface [2]. Therefore, super-cavitation should be avoided, since it severely reduces the atomisation. There are also other negative aspects of cavitation aside from super-cavitation. Notably it can erode the injector, thus reducing its lifetime. Further, if the injection pressure is increased, for a cavitating injector the flow rate is still constant. This removes the option of increasing spray penetration by using higher pressures, and thus higher atomisation. Ultimately it will impair performance of the engine.

PREVIOUS STUDIES ON CAVITATION IN NOZZLES

Numerical studies on Diesel sprays are usually based on Euler-Lagrangian modelling according to the Discrete Droplet Model (DDM). Few attempts have been made to model the entire spray using only an Eulerian framework, and those that have been made have usually been done in 2D [3] or have been limited to a restricted part of the spray [4]. There are also hybrids, like the model described in [5], in which Lagrangian parcels are added to the spray when the liquid phase is sufficiently disperse. However, the most common way of modelling sprays is still to use a combination of Eulerian gas and Lagrangian liquid descriptions. Associated with the DDM model are several sub-models describing injection, atomisation, break-up, evaporation, combustion etc.

The injection model will be described further, as it is of particular interest when studying cavitation. One of the most common approaches when modelling injection is to assume the droplets follow a distribution with some estimated parameters, and then sample the droplet size from that distribution. This type

of model was used in [6–8]. More ambitious injection models, which attempt to couple the nozzle flow to the injected droplets, have been presented [9–11]. However, their rationale has not been based on CFD or experimental data, but on theoretical considerations and assumptions. This paper focuses on verifying a code for a cavitating injector, thereby providing a sound foundation for the subsequent development of a new injection model.

Previous works related to cavitation in nozzles under diesel conditions have focused on various aspects of the associated phenomena. One option, adopted by Sarre *et al* [12], is to use CFD to investigate the nozzle flow and couple it to the spray. Sarre *et al* focused on the spray calculations, and the effect the flow in the nozzle has on the spray, rather than studying the actual nozzle flow. In other studies only the nozzle flow has been simulated, e.g. the study by Mulemane *et al* [13], in which two of the possible modelling approaches to cavitation was explored. The cited authors present pressure plots similar to those in this article, but do not compare their numerical results with experimental data.

There is also a study by Yuan *et al* [2], in which the cavitating flow inside the nozzle as well as the atomising spray close to the nozzle is modelled. This approach is not common, due to the complexities associated with the presence of three phases: liquid, vapour formed from the cavitated liquid, and gas which the liquid is being injected into. Diesel injection into air without cavitation has also been simulated in [4].

Cavitation can be modelled in several ways. There are interface tracking methods, which have two explicit phases, and continuum methods which have just one explicit phase. Continuum methods include the Rayleigh-Plesset bubble method [14, 15], barotropic equation of state method [13, 16], and a third rarely used method based on Gibbs free energy [17].

The method chosen for cavitation modelling for this work is the barotropic equation of state approach, mainly because it is most appropriate for the cavitation that occurs in diesel injectors, which originates from flow separation at the nozzle inlet. The Rayleigh-Plesset (RP) approach is therefore unsuitable, since it is based on the specified bubble density, and assumes gas diffusion and bubble coalescence to be important factors [13]. However, since the velocity in diesel injectors is high, diffusion and bubble coalescence can be assumed to have negligible effects. Further, the code we used is a simplified Volume of Fluid (VOF) code that allows both diesel vapour and air to be modelled. Since the Barotropic equation of state is more consistent with the VOF framework, it was deemed to the most suitable method for this work.

The barotropic equation of state method described in [13] differs from the one used here in the sense that it assumed the two fluid phases to be incompressible. In this paper both phases are compressible, which increases the physical validity. It also differs from the one presented by Schmidt [16], in which an equation of state is analytically integrated, and thus the pressure is found as a function of density.

Experimental data in the field are very scarce, and many models have only been validated (if at all) by comparing simulated and empirical discharge coefficients, cavitation numbers and average velocities. This is due to the difficulties involved in experimentally investigating the nozzle flow. Often the cavitation along the sides of the nozzle makes it very difficult to evaluate the flow inside, since the cavitation hinders optical analysis. However, in experiments presented in [18] a nozzle was set up in such a way that cavitation was limited to two of the four sides of the nozzle, thus allowing the pressure and velocities of the flow to be measured. The data acquired in these experiments are used to validate the model presented in this article.

The main objective of this paper is to introduce the new model, by first describing the theory underlying the equation of state (EOS) used, and then the momentum equations and how they are solved. The experimental case study used to compare to the simulations is briefly described, and the numerical setup. Finally, results are presented, including both pressure profile comparisons and cavitation probability images.

THEORY

To model the flow in the nozzle, we need to model the cavitation, and either resolve the turbulent scales or model them. Turbulence is not modelled, due to the relatively weak influence it is believed to have on the nozzle flow, compared to the cavitation [14]. The only way turbulence is addressed is in stabilising numerics (in contrast to DNS computations) which are not sufficiently accurate to include all scales of the turbulence. As mentioned above, the barotropic equation of state was the method chosen for modelling cavitation. We also assumed homogenous equilibrium, i.e. the liquid and vapour are assumed to always be perfectly mixed in each cell. The parameter γ describes the amount of cavitated vapour in each cell.

For the method chosen to model the cavitation, an equation of state is needed. The temperature is assumed to be constant, which is not a major limitation [18]. A common barotropic equation of state is the non-equilibrium differential equation:

$$\frac{D\rho}{Dt} = \psi \frac{Dp}{Dt} \qquad (1)$$

ψ refers to the compressibility, which is the inverse square root of the speed of sound in the cavitating mixture. This equation can either be used directly in the continuity equation to formulate a pressure equation, or integrated to obtain the pressure as a function of the density. The latter approach was adopted by Schmidt *et al* [16], as mentioned earlier. The former approach is problematic because equation 1 is not an equilibrium equation of state, so the pressure and density obtained are not consistent with the liquid and vapour equations of state unless equilibrium

has been reached. Before equilibrium is attained errors will arise, and the code will not yield corrects result when it has been attained.

The equation of state should therefore be consistent with the liquid and vapour equations of state both at the limits when there is pure liquid or pure vapour, and at intermediate states when there is some form of mixture. The two states can be described by the linear equation of state:

$$\rho_v = \psi_v p \qquad (2)$$
$$\rho_l = \rho_l^0 + \psi_l p \qquad (3)$$

The parameter that describes how much of the liquid is in each phase is γ:

$$\gamma = \frac{\rho - \rho_{l,sat}}{\rho_{v,sat} - \rho_{l,sat}} \qquad (4)$$

$\gamma = 1$ corresponds to a fully cavitated flow, and $\gamma = 0$ a flow with no cavitation. $\rho_{v,sat}$ is calculated from

$$\rho_{v,sat} = \psi_v p_{sat} \qquad (5)$$

ψ_v is the compressibility of the vapour. These properties together form the mixture's equilibrium equation of state:

$$\rho = (1 - \gamma)\rho_l^0 + (\gamma \psi_v + (1 - \gamma)\psi_l) p^{sat} + \psi(\gamma)(p - p^{sat}) \qquad (6)$$

The compressibility ψ was first mentioned in equation 1, but nothing was said of how it is chosen. It can be modelled in several ways, one very common way is the Wallis model [19]. The model chosen here is a simple linear one:

$$\psi = \gamma \psi_v + (1 - \gamma)\psi_l \qquad (7)$$

A linear model was selected partly because the code we used is based on a VOF code, for which linear combinations of γ are highly suitable for describing the mixtures properties, and partly because it gives greater stability than the Wallis model. The γ value is also used to calculate the mixture's viscosity, in the same manner as the compressibility:

3

$$\mu_f = \gamma\mu_v + (1-\gamma)\mu_l \qquad (8)$$

When a linear model is used for the compressibility, the equation of state (6) can be simplified into:

$$\rho = (1-\gamma)\rho_l^0 + \psi p \qquad (9)$$

The first term governs the liquid's density when γ is low. If the fluid is cavitated, the second term becomes more dominant. The first term contains the property ρ_l^0 which is:

$$\rho_l^0 = \rho_{l,sat} - p_{sat}\psi_l \qquad (10)$$

$\rho_{l,sat}$ is the liquid density at standard conditions. The saturation density of the vapour, previously used to calculate γ, is important for the liquid's tendency to cavitate. A higher $\rho_{v,sat}$ will not require as low ρ to get a higher γ.

Unlike the model used by Schmidt *et al* [16], the code does not solve the Euler equations for inviscid flow to obtain the velocity and density. Viscous terms are included, and the momentum equations are solved for U, not ρ U which is common for friction-free compressible flows. A brief description of the methodology of the code is given for clarity. The iteration process starts by solving the continuity equation (eq. 11) for ρ, which is where rho is convected.

$$\frac{\partial\rho}{\partial t} + \nabla\cdot(\rho U) = 0 \qquad (11)$$

The ρ in the divergence term $\nabla\cdot(\rho U)$ is interpolated by use of a total variation diminishing (TVD) scheme named MUSCL. The MUSCL scheme is second order in space, and appropriate when there are large gradients present, like the one between liquid and vapor density. Several other options are easily available in the code. ρ is also used to obtain preliminary values for γ (eq. 4) and ψ (eq. 7), and when defining the momentum equations.

$$\frac{\partial\rho U}{\partial t} + \nabla\cdot(\rho UU) = -\nabla p + \nabla(\mu_f \nabla U) \qquad (12)$$

The momentum equations are used in an ordinary fashion to get the matrices used to calculate the pressure-free velocity. The same TVD scheme with MUSCL limiter is used for the velocity divergence term. It was found to be very important to choose a proper scheme for the velocity, if a too stable scheme is used the cavitation region will be flat. Following this is an ordinary PISO loop, to solve for p and correct the velocity to achieve continuity. For a description on how OpenFOAM achieves continuity and solves for p, see [20]. The equation solved in the PISO loop is again the continuity equation, but this time transformed into a pressure equation by use of equation 6.

$$\frac{\partial\psi p}{\partial t} - \left(\rho_l^0 + (\psi_l - \psi_v)p_{sat}\right)\frac{\partial\gamma}{\partial t}$$
$$-p_{sat}\frac{\partial\psi}{\partial t} + \nabla\cdot(\rho U) = 0 \qquad (13)$$

When continuity has been reached, the remaining properties γ, ρ and ψ are updated. ρ is now updated according to the EOS, eq. 6. The time step is limited by both the Courant number, and the acoustic Courant number, respectively defined as:

$$\mathrm{Co} = \max\left(\frac{|U|}{\Delta x}\right)\Delta t \qquad (14)$$

and

$$\mathrm{Co}_{acoustic} = \max\left(\frac{1}{\sqrt{\psi}\Delta x}\right)\Delta t \qquad (15)$$

The Courant number was chosen to be limited to 0.125, and the acoustic Courant number was limited to 12.5 in all of the simulations. However, the non-acoustic Courant number is the real limiter of the time-step, and the acoustic Courant number is usually around 2-3.

The model described is implemented for the OpenFOAM platform, under the name cavitatingFoam (in OpenFOAM 1.4). OpenFOAM is an open source toolbox for CFD, written in C++, available at www.openfoam.com.

STUDY

The results produced by the code are compared to data acquired in experiments performed at AVL's laboratories, in which diesel fuel was pumped through a nozzle-like structure. The setup is described in [18], and the model nozzle is shown in figure 1. The experiments generated data on density/pressure as well as images of the cavitation region, and due to the simplicity of the geometry they are suitable for comparison to numerical
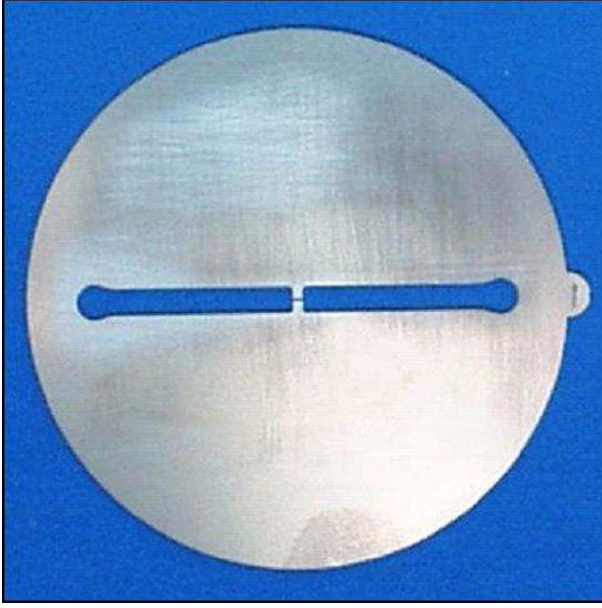
4

Figure 1.   VIEW OF THE EXPERIMENTAL NOZZLE, 1 cm CHANNEL BEFORE AND AFTER THE NOZZLE
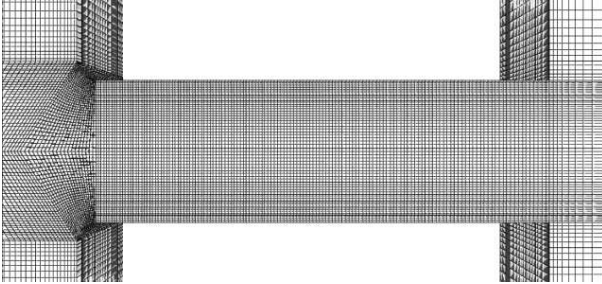

Figure 2.   CLOSE-UP OF THE MEASURED REGION, 299 μm WIDE, 1 mm LONG

data. An image of a typical mesh can be seen in figure 2. In the experiments the injection pressure was 10 MPa, and the outlet pressures were varied.

Table 1.   DATA ON DIESEL FUEL

property	liquid	vapour
density (kg/m^3)	832	0.1361
viscosity (kg/ms)	0.0065	$5.953 \cdot 10^{-6}$
compressibility (s^2/m^2)	$5 \cdot 10^{-7}$	$2.5 \cdot 10^{-6}$
vaporation pressure (Pa)		$5.4 \cdot 10^3$

Some of the values in table 1 have large margins of error. For example, the compressibility of diesel vapour at room temperature is an estimation based on the ideal gas law. The compressibility of the liquid is taken from measurements of the speed of sound in diesel fuel [21], which is around 1400 m/s. The evaporation pressure chosen was that of heptane, since it is commonly used as a model fuel for diesel. The liquid density was measured in the experiments, while the vapour density was from the equation

$$\rho_{v,sat} = \psi_v p_{sat} \qquad (16)$$

The gas viscosity was obtained from the Lucas viscosity model described in [22] (again based on n-heptane's properties), and the liquid viscosity from Petrocard's data on their diesel fuel products. As will be shown in the results section, the model is not sensitive to many of these physical properties (apart from the liquid viscosity), as long as they are of the right order.

The walls on the sides of the nozzle, have an ordinary no-slip condition for the velocity. The upper and lower walls, on the other hand, have a slip condition for the velocity, similar to that used in supersonic compressible flow. Perpendicular to the wall the flow (or flux) is zero, but the flow in the tangential direction of the wall is not. A no-slip boundary condition would lead to overestimates of the thickness of the boundary layer, resulting in strong vortices in the centre of the channel, and incorrect modelling of the flow's cavitation. Figure 3 shows these vortices and the resulting cavitation. As mentioned earlier, viscosity is sometimes disregarded entirely, here we have chosen to disregard the viscosity from two walls due to the assumed thinness of the boundary layer on those two walls.

RESULTS

In all of the experimental cases the injection pressure was 10 MPa, and the outlet pressure was varied. The two outlet pressures used here for detailed comparison are 5.1 MPa, 3 MPa and 1.5 MPa. In the experiments cavitation was measured by a line of sight method, i.e. all cavitation observed from the top of the nozzle was recorded, and then averaged as shown in figure 4. The numerical simulations are evaluated by a similar line of sight method, in which the domain is searched for cavitated cells. Both the experimental and numerical values are averaged over 20 time-steps, resulting in images such as the one shown in figure 5. The average value at time t^n is calculated from

$$\overline{U^n} = \frac{\overline{U^{n-1}}\left(t^n - t^0\right) + U^n \Delta t^n}{t^n + \Delta t^n - t^0} \qquad (17)$$
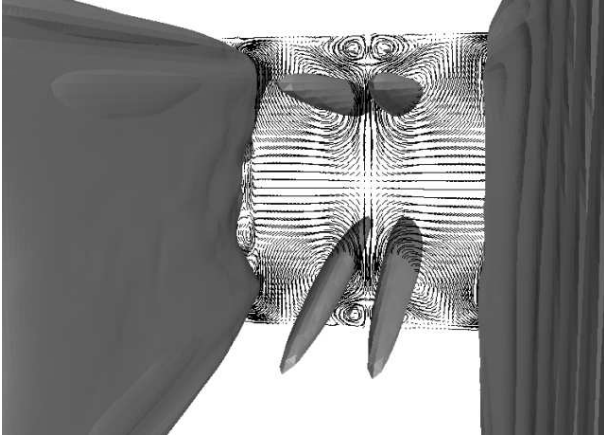
5

Figure 3. MEAN ISOSURFACE FOR VAPOR FRACTION OF 0.1, VELOCITY FIELD IN A PLANE PERPENDICULAR TO THE FLOW DIRECTION SHOWN TO VISUALIZE THE VORTICES, NO-SLIP CONDITION USED ON BOTH UPPER AND LOWER WALL

t^0 is the start time for the average, and Δt^n is the timestep at time n.

When comparing the different cases, the discharge coefficient is used to measure how much losses there are in the injector. This has been defined as:

$$Cd = \frac{\dot{m}_{calculated}}{\dot{m}_{Bernoulli}} = \frac{\sum_i^N \rho_i U_i A_i}{\sqrt{2\Delta p \rho_0}A} \qquad (18)$$

The simulations (figures 5 & 7) predict the experiments (figures 4 & 6) quite well, even though the simulations yield slightly more cavitation than observed in the experiments. The model manages to predict when the flow is super-cavitating, i.e. when the cavitation region extends throughout the entire nozzle. This occurs when the outlet pressure is 1.5 MPa, but not when it is 3 MPa.

The experimental data also include pressure measurements along the channel centreline and a line 40 μm from the channel wall. Figures 8 and 9 illustrate these results, and as can be seen the calculations do not predict the experimental results well. It is important to point out that the measured pressure is much higher than the saturation pressure for the liquid, but the cavitation probability is still shown to be 100 % close to the wall (4). This will be discussed later in the Conclusions section. The pressures in the experiments are derived from density measurements, and an equation of state. In the pressure profile plots, the channel starts at 0 and ends at 1 mm.

The mass flow is calculated for several time-steps, and averaged in time over the last 100 μs. The mass flow behaviour is
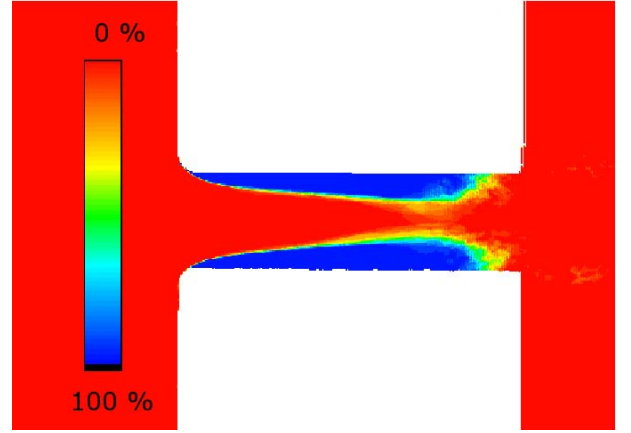

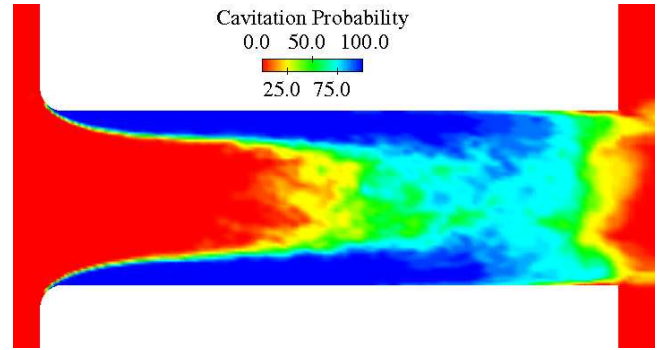Figure 4. IMAGE OF THE EXPERIMENTAL CAVITATION PROBABILITY, INJECTION PRESSURE 7 MPa

Figure 5. IMAGE OF THE COMPUTED CAVITATION PROBABILITY, INJECTION PRESSURE 7 MPa

Table 2. COMPARISON OF MODELLED AND EXPERIMENTAL DATA

p_{out}	$\dot{m}_{experiment}$	$\dot{m}_{model}$	Std. Deviation	Cd_{model}
5.1 MPa	$6.98 \cdot 10^{-3}$	$7.53 \cdot 10^{-3}$	$2.31 \cdot 10^{-5}$	0.93
3 MPa	$8.46 \cdot 10^{-3}$	$8.54 \cdot 10^{-3}$	$1.49 \cdot 10^{-4}$	0.88
1.5 MPa	$8.46 \cdot 10^{-3}$	$8.53 \cdot 10^{-3}$	$2.25 \cdot 10^{-4}$	0.80

predicted within 1% for the cavitating cases, and 10 % for the non cavitating case ($\Delta p = 5.1$ MPa). The model can also predict the choking of the channel which occurs when it starts to cavitate. The discharge coefficient is also listed, which shows how much more losses there are in the strongly cavitating case. With the mass flow constant for increased pressure difference, the discharge coefficient will decrease with increasing pressure difference.

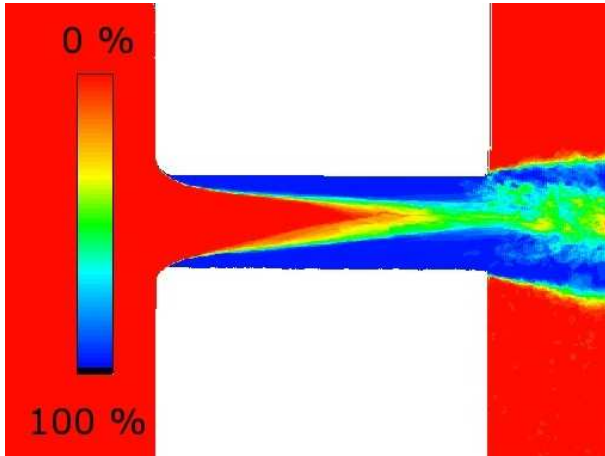The reason why the mass flows differ, could be underesti-

6

Figure 6. IMAGE OF THE EXPERIMENTAL CAVITATION PROBABIL-
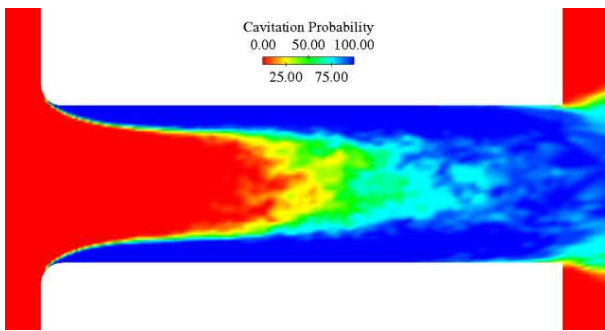ITY, INJECTION PRESSURE 8.5 MPa

Figure 7. IMAGE OF THE COMPUTED CAVITATION PROBABILITY, IN-
JECTION PRESSURE 8.5 MPa

Figure 8. AVERAGE PRESSURE ALONG THE CENTRELINE OF THE
NOZZLE
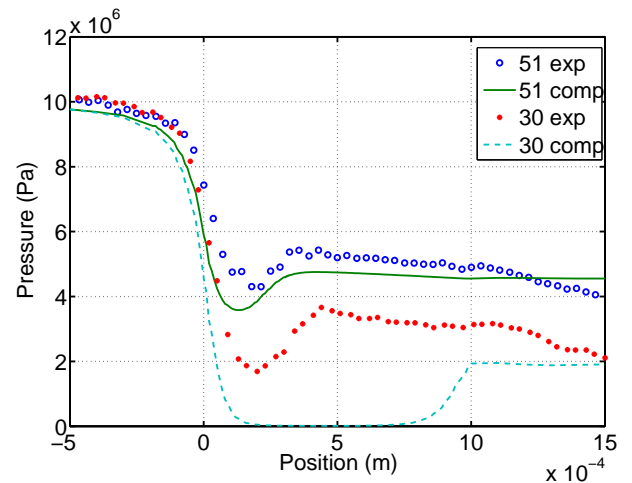
Figure 9. AVERAGE PRESSURE ALONG THE WALL OF THE NOZZLE

mation of the liquid viscosity. As mentioned when the physical properties were shown, there are high uncertainties in the data. Another factor could be the lack of friction in the simulations on the two walls with slip boundary condition, which reduces the friction more than the lack of rough walls. This simplifications was forced due to the presence of a strong cavitating vortex as mentioned earlier.

To save computational time, a quarter of the mesh, in this case 90 degrees of the full mesh, is often used. However, if such a restriction is imposed turbulence will not be correctly modelled, and it will not be possible to capture large eddies. It is however, still an attractive option due to the reduction in computational time. The case with an outlet pressure of 3 MPa was examined with both the full 3D mesh, consisting of 1.7 million cells, and the quarter mesh consisting of only 508 000 cells, to examine possible differences in the outcome. The results (Figure 10), show that the quarter mesh provides a possible approximation to the three dimensional flow. However, differences in mass
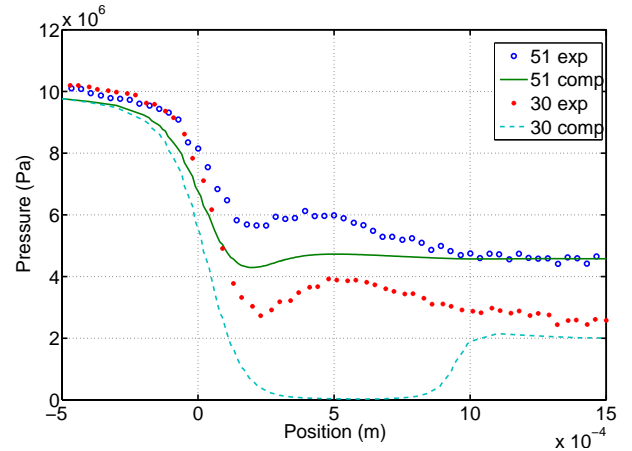
flow can be seen by comparing tables 4 and 2, for the case of 500k cells and an outlet pressure of 3 MPa.

The effects of inlet rounding are often considered since it affects cavitation; a well rounded inlet can reduce cavitation, while a sharp inlet gives more cavitation. Since the rounding does not affect the total pressure drop over the nozzle, it can be seen as a way of examining the flow as if there were no cavitation at all. The data shown in Figure 11 and table 3 were produced using a quarter of the channel, to reduce computational time.

Rounding was not varied in the experiments reported in [18], so the exact values can not be verified. However, the results show that the model can predict the reduced cavitation and increased flow rate as the inlet becomes more round. The discharge coefficient also increases, since there is less cavitation causing losses.
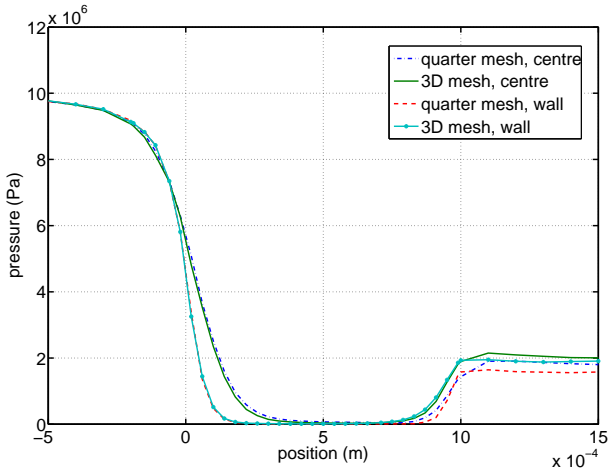
7

Figure 10. AVERAGE PRESSURE ALONG THE CENTRELINE AND WALL OF THE NOZZLE, QUARTER AND FULL GEOMETRY RESULTS SHOWN, PRESSURE DIFFERENCE 7 MPa
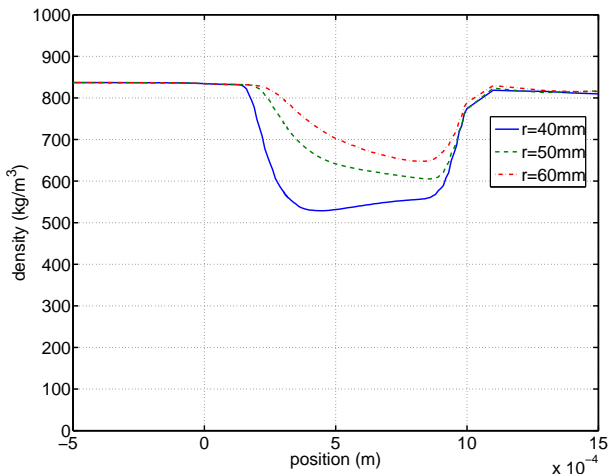

Figure 11. DENSITY ALONG THE WALL OF THE NOZZLE, THREE DIFFERENT INLET RADII., PRESSURE DIFFERENCE 7.0 MPa

Table 3. DISCHARGE COEFFICIENTS AND MASS FLOWS FOR DIFFERENT VALUES OF THE INLET ROUNDING RADIUS

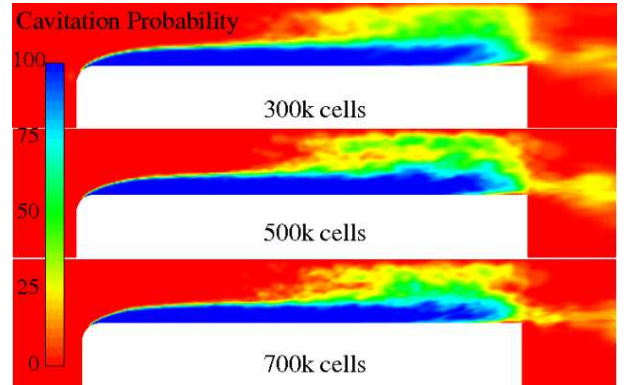| r_{inlet}	$\dot{m}$	C_d
40 mm	$8.60 \cdot 10^{-3}$	0.889
50 mm	$8.83 \cdot 10^{-3}$	0.912
60 mm	$9.00 \cdot 10^{-3}$	0.930

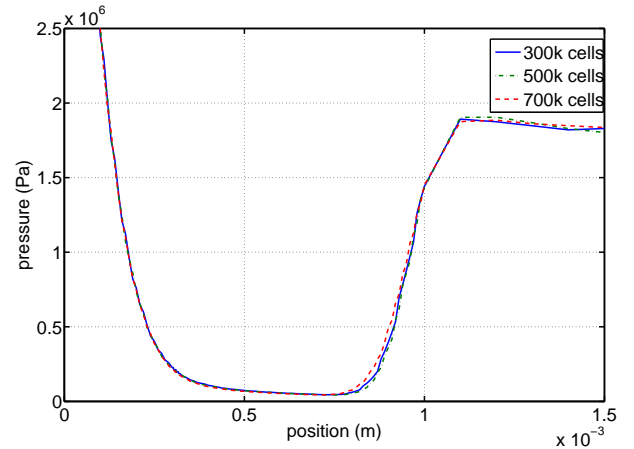Figure 12. CAVITATION PROBABILITY, FOUR DIFFERENT GRIDS USED, INJECTION PRESSURE 7 MPa

Figure 13. PRESSURE ALONG THE CENTRELINE OF THE NOZZLE, WITH FOUR DIFFERENT GRIDS, INJECTION PRESSURE 7 MPa

We have chosen to display density instead of pressure, since it provides a clearer indication of how much the flow has cavitated.

An important factor to examine when trying to model a flow is the grid-size. The standard grid chosen for this study has 508 000 cells, with ca. 5 μm cells in the channel. The grid is graded to be finer close to the wall in the cavitating region, and close to the rounded inlet.

The calculations are not sensitive to grid-size, as can be seen in figures 12-13 and table 4. The figure is zoomed in on the cavitation region, to make it easier to see the small differences. If a grid coarser than the one with 140 000 cells is chosen, the cavitation region will consist of very few cells, and the assumption of homogenous equilibrium becomes invalid. The numerical value for the mass flow in table 4 is different from the flows listed in table 2, since the first are from the quarter mesh, and the latter from the full 3D grid.

As mentioned in the Study section, some of the parameters

8

Table 4. MASS FLOWS AND DISCHARGE COEFFICIENTS CALCULATED FROM THREE DIFFERENT GRIDS, QUARTER OF DOMAIN USED

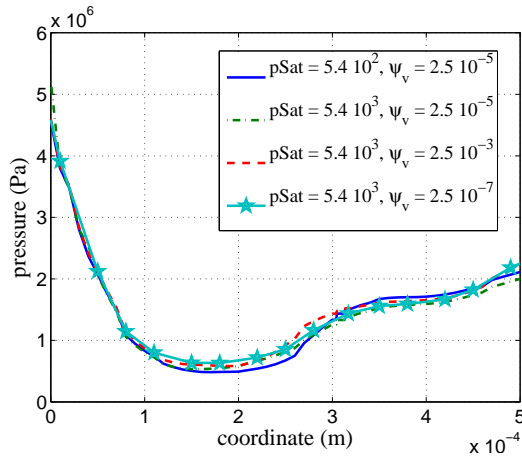| r_{inlet}	$\dot{m}$	C_d
300k cells	$8.59 \cdot 10^{-3}$	0.89
500k cells	$8.60 \cdot 10^{-3}$	0.88
700k cells	$8.57 \cdot 10^{-3}$	0.89

Figure 14. CLOSE-UP OF THE PRESSURE ALONG THE WALL, PRESSURE DIFFERENCE 7.0 MPa, WITH FOUR DIFFERENT COMBINATIONS OF ψ_v AND p_{sat}

are difficult to measure experimentally, and few data are available. To test the model's sensitivity to the ψ_v three different values of this parameter were tested for the $p_{diff} = 7$ MPa case. The results are shown in figure 14.

CONCLUSIONS AND FUTURE WORK

A new model for calculating the flow in a cavitating nozzle has been developed. The model has been validated against data obtained in experiments with a simple contraction type nozzle. It has been shown that the model can predict the cavitation probability in the nozzle, and the effects of variations in the pressure differences over the nozzle. There is a slight over prediction for the cavitation probability, which could be due to underestimation of the liquid's viscosity. The model is also capable of predicting choking of the flow in the channel, since the mass flow does not increase above the value it has when the flow starts to cavitate.

The pressure profile from the simulations are not similar in shape or value to the experimentally derived profiles. They are slightly better for the non-cavitating case. However, the experimental data show a minimum pressure close to the wall (figure 9) at around 2 MPa, although the cavitation probability is said to be 100 % in this region (figure 4). If the average pressure really would be of the magnitude suggested by the pressure profile plots, the flow would not cavitate at all. The authors have therefore chosen not to try to match the simulated pressure curve to the experimental ones. The experimental data were acquired by a line of sight method, so variations in the width of the cavitation region at different heights in the nozzle would not have been seen. If the cavitation region is only large close to the walls, and smaller at greater distances from them, this could explain why the average pressure is said to be much higher than the evaporation pressure of the liquid. The simulations indicate that the cavitation region is spread out and is not interrupted by any large non-cavitating areas.

The influence of the walls should also be considered, since the walls have different boundary conditions. When normal non-slip conditions were applied, the flow started to cavitate in the central part of the channel, due to strong vortices. These cavitated regions were separated from the wall cavitation, and thus did not result from the pressure drop following the contraction. It was found that the vortices originated from the top and bottom walls, and if the boundary condition on those walls were changed to a slip condition, a more physical behaviour of the flow was observed. However, if the same slip condition was applied to all walls, the cavitation region would grow larger (preliminary calculations suggest this). It would also increase the mass flow, since the friction is reduced when the walls are made inviscid (and, notably, many previously used cavitation codes have assumed completely inviscid flow).

The real walls in the experiments are not perfectly smooth, unlike the walls in the simulations. Smooth walls might inhibit cavitation, since they provide fewer cavitation sites. However, introduction of rough walls would require a new form of modelling, since the barotropic equation of state is not dependent on the presence of cavitation sites.

To further validate the model, more simulations would be needed, preferably with comparison to other sets of experimental data. Since the goal is to simulate diesel sprays, higher injection pressures should be tested as diesel injection pressures often exceed 100 MPa.

9

REFERENCES

[1] Faeth, G. M. and Hsiang, L-P and Wu, P-K, 1995. "Structure and Breakup Properties of Sprays". *International Journal of Multiphase Flow,* **21**, pp. 99–127.

[2] Yuan, W., and Schnerr, G., 2003. "Numerical Simulation of Two-Phase Flow in Injection Nozzles: Interaction of Cavitation and External Jet Formation". *Journal of Fluids Engineering,* **125**, pp. 963–969.

[3] Iyer, V. and Abraham, J., 2003. "An Evaluation of a Two-Fluid Eulerian-Liquid Eulerian-Gas Model for Diesel Sprays". *Journal of Fluids Engineering,* **125**, pp. 660–669.

[4] de Villiers, E., Gosman, A., and Weller, H., 2004. "Large Eddy Simulation of Primary Diesel Spray Atomization". *SAE Paper 2004-01-0100.*

[5] Blokkeel, G., Barbeau, B., and Borghi, R., 2003. "A 3D Eulerian Model to Improve the Primary Breakup of Atomizing Jet". *SAE Paper 2003-01-0005.*

[6] Peng Kärrholm, F., and Nordin, N., 2005. "Numerical Investigation of Mesh/Turbulence/Spray Interaction for Diesel applications". *SAE Paper 2005-01-2115.*

[7] Lippert, A., Chang, S., Are, S., and Schmidt, D., 2005. "Mesh Independence and Adaptive Mesh Refinement For Advanced Engine Spray Simulations". *SAE Paper 2005-01-0207.*

[8] Kim, H., and Sung, N., 2004. "Combustion and Emission Modeling for a Direct Injection Diesel Engine". *SAE Paper 2004-01-0104.*

[9] Rotondi, R., Bella, G., Grimaldi, C., and Postrioti, L., 2001. "Atomization of High-Pressure Diesel Spray: Experimental Validation of a New Breakup Model". *SAE paper 2001-01-1070.*

[10] Baumgarten, C., Stegemann, J., and Merker, G., 2002. "A New Model For Cavitation Induced Primary Break-up of Diesel Sprays". *ILASS-Europe Zaragoza.*

[11] Huh, K.Y., and Gosman, A.D., 1990. "Atomization Mechanism of Fuel Injection". *ILASS.*

[12] von Kuensberg Sarre, C., Kong, S., and Reitz, R., 1999. "Modeling the Effects of Injector Nozzle Geometry on Diesel Sprays". *SAE Paper 1999-01-0912.*

[13] Mulemane, A., Subramaniyam, S., Lu, P., Han, J., Lai, M., and Poola, R., 2004. "Comparing Cavitation in Diesel Injectors Based on Different Modeling Approaches". *SAE Paper 2004-01-0027.*

[14] Payri, R., Margot, X., and Salvador, F., 2002. "A Numerical Study of the Influence of Diesel Nozzle Geometry on the Inner Cavitating Flow". *SAE Paper 2002-01-0215.*

[15] Yuan, W., Sauer, J., and G.H., S., 2001. "Modeling and Computation of Unsteady Cavitation Flows in Injection Nozzles". *Mechanique & Industries,* **2**, pp. 383–394.

[16] Schmidt, D.P., Rutland, C.J. and Corradini, M.L., 1999. "A Fully Compressible Two-Dimensional Model of High Speed Cavitating Nozzles". *Atomization and Sprays,* **9**.

[17] Vortmann, C., Schnerr, G., and Seelecke, S., 2003. "Thermodynamic Modeling and Simulation of Cavitating Nozzle Flow". *International Journal of Heat and Fluid Flow,* **24**.

[18] Winklhofer, E., Kull, E., Kelz, E., and Morozov, A., Zurich, Switzerland, 2001. "Comprehensive Hydraulic and Flow Field Documentation in Model Throttle Experiments Under Cavitation Conditions". *ILASS-Europe Annual Meeting,* pp. 574–579.

[19] Wallis, G. B., 1969. *One-dimensional Two-phase Flow.* McGraw-Hill, New York.

[20] Peng Kärrholm, F., 2006. *Numerical Modelling of Diesel Spray Injection and Turbulence Interaction.* Department of Applied Mechanics, Chalmers University of Technology.

[21] Mustafa, E. T., and Van Gerpen, J. H., 2003. "Effect of Temperature and Isentropic Bulk Modulus of Mixtures of Biodiesel and Diesel Fuel". *Journal of the American Oil Chemists' Society,* **80**(11), pp. 1127–1130.

[22] Poling, B., Prausnitz, J., and O'Connell, J., 2001. *The Properties of Gases and Liquids*, 5th ed. McGraw-Hill.